Studies of energy dissipation pathways in the water formation reaction using metal-oxide-semiconductor nanostructures

Dissertation
zur Erlangung des Doktorgrades
der Naturwissenschaften
- Dr. rer. nat. -

vorgelegt von

Ievgen I. Nedrygailov

geboren am 07. Dezember 1980 in der Ukraine

Fakultät für Chemie
Universität Duisburg-Essen

März 2014

Die vorliegende Arbeit wurde im Zeitraum von März 2010 bis März 2014 im Arbeitskreis von Prof. Dr. Eckart Hasselbrink am Institut für Physikalische Chemie der Universität Duisburg-Essen durchgeführt.

Gutachter:	Prof. Dr. Eckart Hasselbrink
	Prof. Dr. Christian Mayer
Vorsitzender:	Prof. Dr. Thomas Schrader
Tag der Disputation:	19 März 2014

Contents

Abstract

Catalytic chemical reactions are complex processes, which include a variety of steps such as molecular adsorption and dissociation on a surface, interactions between intermediates, and desorption of products from the surface to the gas phase. Considerable effort has been made to achieve a detailed microscopic understanding of the dynamics of these processes using different experimental and theoretical methods, nevertheless still little is known about the routes of energy transfer accompanying gas-surface interactions [1, 2, 3]. In particular, the role of electronic excitations for the energy dissipation in surface chemical reactions is a subject of debate [2, 4]. Resolving this issue is of particular interest for the understanding of the surface chemical reactions.

Recently, an easy to implement approach to study energy transfer processes accompanying exothermic gas-surface interactions with the use of metal-semiconductor (MS) [2, 5, 6, 7, 8, 9], metal-oxide-semiconductor (MOS) [10], and metal-insulator-metal (MIM) [11, 12] nanostructures has been demonstrated. These devices allow direct detection of electronic excitation induced by the the non-adiabatic dissipation of chemical energy as a macroscopic electric current, called chemicurrent. To date, the most significant progress has been made in the study of chemicurrents induced in the course of reactions between atomic species on metals. Main results of these studies are reviewed elsewhere [2, 12]. At the same time, interactions of molecular gases with metal surfaces are less studied. For instance, the number of publications reported observation of an electric current induced by oxidation of hydrogen or carbon monoxide on the surface of platinum catalysts [6, 7, 8, 13, 14, 15, 16]. However, it is not clear yet which reaction steps are responsible for the generation of this current. The contribution of thermal effects in the generation of the chemicurrent is also not fully understood [16, 17].

The goal of this work is to study processes of an electric charge generation and transfer, induced by adsorption of oxygen and hydrogen molecules, and reactions between them on a polycrystalline surface of platinum with the use of the Pt/SiO_2-n-Si MOS nanostructures. In particular, it aims to find answers to the following questions: (1) Is there any electronic excitation, accompanying steps of the water formation on platinum, which can be detected using MOS nanostructures? (2) What is the mechanism of this chemicurrent creation? (3) How big is the impact of thermal effects, due to the surface chemical reaction, on the process of the chemicurrent detection using MOS nanostructures.

Chapter 1

Introduction

When gas particles, atoms or molecules, are approaching a surface of a solid, new chemical bonds can be formed. Some of these processes, called exothermic, lead to liberation of significant amounts of energy, which can reach several electron volts per reaction event [18]. Dissipation of this energy may lead to a variety of elementary excitations on the surface, such as collective lattice vibrations (phonons), electron-hole pairs, exo-electrons, exo-ions and chemiluminescence (emission of photons). This chapter aims to overview briefly all these effects. However, the main focus will be on the phenomena associated with the excitation and detection of electron-hole pairs.

1.1 Overview of processes induced on the surface by an exothermic chemical reaction

1.1.1 Transfer of energy in gas-surface interactions

When exothermic chemical reactions take place on a solid surface, chemical energy can be transferred from the reacting particles to the degrees of freedom of the solid [1, 2, 3, 6, 7, 8, 12, 13, 14]. Applying classical mechanicals, the average energy exchange between an incoming gas particle of mass m and a surface atom of mass M can be estimated by the Baule formula [19, 20, 21]:

$$\Delta(E_{\mathrm{i}}, T_{\mathrm{s}}) = \frac{4\mu}{(1+\mu)^2}(E_{\mathrm{i}} - \frac{1}{2}k_{\mathrm{B}}T_{\mathrm{s}}) \tag{1.1}$$

where $\mu = m/M$ is the mass ratio, E_{i} is the kinetic energy of the incoming gas particle, k_{B} is the Boltzmann constant, and T_{s} is the surface temperature. According to this equation, the most efficient energy transfer can be expected for the case, when the mass of the incoming gas particle is equal to the mass of the surface atom, i.e. $\mu = 1$. However, when μ becomes either smaller or larger than unity, the efficiency of the energy exchange

in a gas-surface interaction becomes less effective.

As a rule, catalytic chemical reactions are divided into those which can be described in terms of the Langmuir-Hinshelwood (LH) mechanism [22], and those which can be described within the limits of the Eley-Rideal (ER) mechanism [23]. In the simplest case, for the chemical reaction $A + B \rightarrow AB$, the LH mechanism takes place when both reactants are adsorbed and accommodated on the surface. The ER mechanism take place when the first reactant can react with the second one, which is adsorbed on the surface, directly from the gas phase. As noted in References [3, 24, 25], a prerequisite for the successful chemical event on the surface for both LH and ER mechanisms is that the adsorbing reactants can dissipate their excess kinetic energy. This can be easily achieved when masses of reactants are equal or close to the mass of the surface atoms, as, according to Equation 1.1, the energy transfer in this case is very efficient. However, for chemical reactions of light particles on the solid surface, consisting of heavy atoms (which is a frequent case in catalysis), the energy transfer with the use of nuclear degrees of freedom is inefficient. Therefore, other channels of the energy dissipation, such as the energy dissipation through the electronic excitations, should be taken into consideration [3, 25].

1.1.2 Adiabatic and non-adiabatic processes of chemical energy dissipation

De-excitation of the adsorbate-solid system is driven by the need to minimize the Gibbs free energy, which, however, does not dictate the way of reaching the state of thermal equilibrium [26]. Thus, this can occur with the involvement of either nuclear or electronic degrees of freedom and lead to the following elementary excitations on the surface: collective lattice excitations of a solid (phonons), electron-hole pairs, and collective electronic excitations (plasmons) [2]. Taking into account the enormous number of degrees of freedom, existing in solids, the easiest way of evaluation of the route by which the solid reaches an equilibrium state is the use of **adiabatic** or Born-Oppenheimer approximation [27]. This approximation implies, that the electronic system of a solid is always in the state of thermodynamic equilibrium with the nuclear coordinates.

Indeed, any solid can be seen as a two-component system of particles: light particles (electrons) and heavy particles (nuclei). The whole solid can be described by the Schrödinger equation, given by [28]

$$\hat{H}\Phi = E\Phi \tag{1.2}$$

where $\hat{H}$ is the Hamiltonian, Φ is the wave function, and E is the energy of a solid with N nuclei of mass M_{N} and n electrons of mass m_{e}.

The wave function depends on the coordinates of all electrons (r_{i}) and all nuclei (R_{j}),

i.e.

$$\Phi = \Phi(r_1, r_2, \ldots, r_{\mathrm{n}}, R_1, R_2, \ldots, R_{\mathrm{N}}) \tag{1.3}$$

The Hamiltonian includes:

1. The operator of the kinetic energy of the electrons

$$\sum_i \left(-\frac{\hbar^2}{2m_{\mathrm{e}}} \Delta_i \right) \tag{1.4}$$

where $\hbar$ is the Planck constant, m_{e} is the electron mass, and $\Delta_i = d^2/dx_i^2 + d^2/dy_i^2 + d^2/dz_i^2$ is the Laplace operator.

2. The operator of the kinetic energy of the nuclei

$$\sum_j \left(-\frac{\hbar^2}{2M_{\mathrm{N}}} \Delta_j \right) \tag{1.5}$$

where M_{N} is the mass of the nucleus, and $\Delta_j = d^2/dX_j^2 + d^2/dY_j^2 + d^2/dZ_j^2$.

3. Potential energy of the Coulomb electron-electron

$$\frac{1}{2} \sum_i \sum_k \left(-\frac{e^2}{r_{ik}} \right) \tag{1.6}$$

and nucleus-nucleus interactions

$$V_0 \left(R_1, R_2, \ldots, R_{\mathrm{N}} \right) \tag{1.7}$$

4. Potential energy of electron-nucleus interactions

$$U(r_1, r_2, \ldots, r_{\mathrm{n}}, R_1, R_2, \ldots, R_{\mathrm{N}}) \tag{1.8}$$

Taking into account all the components of the Hamiltonian, Equation 1.2 can be rewritten as

$$\left[\sum_i \left(-\frac{\hbar^2}{2m_{\mathrm{e}}} \Delta_i \right) + \sum_j \left(-\frac{\hbar^2}{2M_{\mathrm{N}}} \Delta_j \right) + \frac{1}{2} \sum_i \sum_k \left(-\frac{e^2}{r_{ik}} \right) + \right.$$
$$\left. + V_0 \left(R_1, R_2, \ldots, R_{\mathrm{N}} \right) + U(r_1, r_2, \ldots, r_{\mathrm{n}}, R_1, R_2, \ldots, R_{\mathrm{N}}) \right] \Phi = E\Phi \,. \tag{1.9}$$

In the state of thermodynamic equilibrium average values of the kinetic energy of these particles are of the same order of magnitude. Taking into account the fact that the mass of a nucleus is much bigger than the mass of an electron, i.e. $M_{\mathrm{N}} >> m_{\mathrm{e}}$, this means

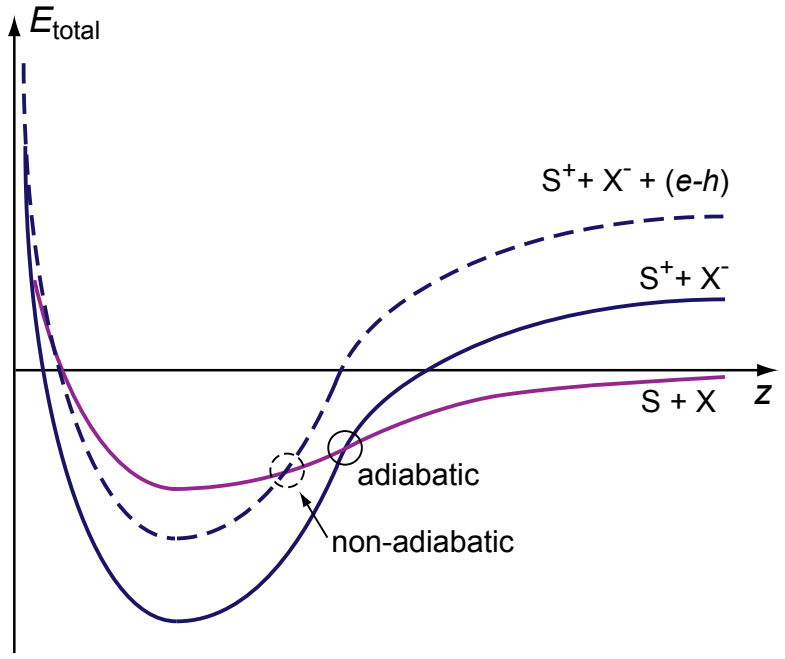

Figure 1.1: Schematic potential energy diagram to demonstrate adiabatic and non-adiabatic surface chemical reaction. Here X denotes a neutral adsorbate approaching a solid surface S. (Redrawn on the basis of Figure 1 [26]).

that velocities of electrons significantly exceed velocities of nuclei in the solid. After each change in the position of the nuclei, the electronic system almost instantly establishes a distribution, which corresponds to a new position of the nuclei. Therefore, it can be assumed that (1) the nuclei are static ($R_1, R_2, \ldots, R_{\mathrm{N}}$ are not variables any more but some parameters $R_{01}, R_{02}, \ldots, R_{0\mathrm{N}}$, kinetic energy of the nuclei becomes equal to zero), (2) the movement of electrons and nuclei occur without energy exchange between electrons and nuclei ($V_0\left(R_1, R_2, \ldots, R_{\mathrm{N}}\right) = 0$). As a result of this approximation, Equation 1.9 can be simplified to

$$\left[\sum_i \left(-\frac{\hbar^2}{2m_{\mathrm{e}}}\Delta_i\right) + \frac{1}{2}\sum_i\sum_k \left(-\frac{e^2}{r_{ik}}\right) + \right.$$
$$\left. + U(r_1, r_2, \ldots, r_{\mathrm{n}}, R_{01}, R_{02}, \ldots, R_{0\mathrm{N}})\right]\Psi_e = E\Psi_e\,. \quad (1.10)$$

Among the consequences of the use of the Born-Oppenheimer approximation for simplification of Equation 1.9 is the complete neglecting of electronic excitations and considering the direct transfer of chemical energy into the lattice excitations (heating) of the solid as the only result of a surface chemical reaction.

If the electron density is low, which is common for gas-solid interfaces, velocities of electron and nuclear motion can be comparable [26]. In this situation the Born-

Oppenheimer approximation breaks down and electronic excitations have to be taken into account [2, 26]. Thus, we have a case of **non-adiabatic** relaxation of a solid, which is characterized by de-excitation of the electronic system in energy steps exceeding thermal fluctuations $k_{\mathrm{B}}T$. The difference between the adiabatic and nonadiabatic relaxation can be demonstrated with the use of potential energy surfaces, Figure 1.1. Here, the curves give the total energy of a system as a function of the reaction coordinate (z) for the case of the interaction between a neutral adsorbate (X) and an atom of a solid (S). If the electronegativities of the reaction species is notably different (such as in the case of a chemical reaction between oxygen and an alkali metal surface) the resulting bond will be ionic. Then, the adiabatic reaction path can be shown by crossing of the potential curves S + X and $\mathrm{S}^{+} + \mathrm{X}^{-}$ [29]. The reaction between the adsorbate and the surface may also happen non-adiabatically and lead to excitation of an $e-h$ pair. In this case relaxation of the system may proceed by phonon coupling or by emission of a particle (exo-emission) or a photon (chemiluminescence) from the surface of a solid, which is schematically shown in Figure 1.2. A detailed description of the progress in studies of the phenomena observed in the course of non-adiabatic chemical reactions on the surface of solids has been done by H. Nienhaus, T. Greber and others [2, 26, 30, 31]. Here, we only briefly characterize some of them, which are of particular interest for this work:

1. **Exo-electron emission** is the emission of electrons by a solid surface (normally a metal surface) in the course of an exothermic chemical reaction. This effect was discovered in 1905 by Thomson who reported the emission of negative particles when a liquid alkali metal was exposed to small amounts of different gases [2, 26]. Later Reboul, Haber and Just studied carefully this effect and identified that these particles, emitted by the alkali metal, were electrons. They also found that the emission of electrons was a result of a surface chemical reaction.

2. Surface **chemiluminescence** is the emission of photons during adsorption of atoms or molecules or their reaction on a solid surface [2, 26, 32, 33]. This effect is weaker than the exo-electron emission. It was studied in the late 1960s after the establishment of the ultra high vacuum techniques in surface science [2]. It is important to note, that the spectrum of the chemiluminescence differs essentially from the spectrum of a black body radiation. The last fact means, that the solid which emits chemiluminescence is not in the state of thermodynamic equilibrium.

3. Generation of **electron-hole pairs** is a process of creation of highly excited electrons and holes in solids as a result of non-adiabatic energy transfer during surface chemical reactions. The direct detection of these excited charge carriers is difficult due to their short life time. For example, in metals they relax within 10^{-14} s by emitting phonons [2, 4]. Therefore, first reports about detection of excited electron-hole pairs appeared in the literature in late 1990s and associated with the beginning

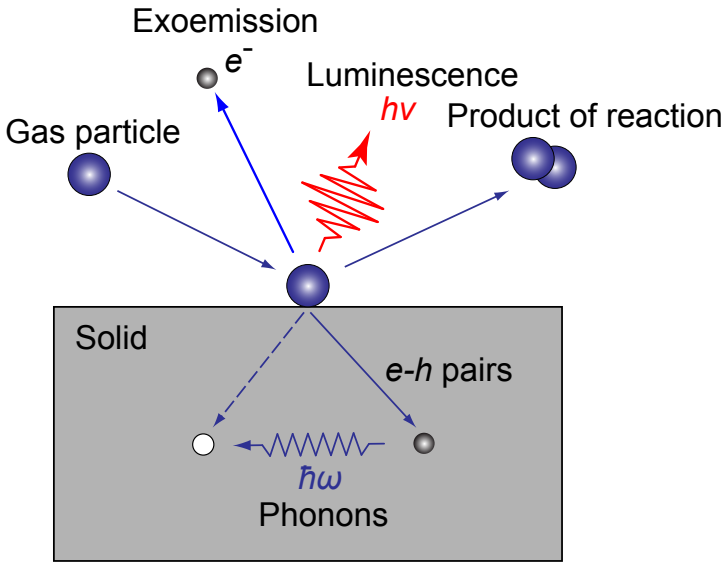

Figure 1.2: Energy dissipation during chemical reaction on a solid surface may happen adiabatically via direct energy transfer to phonons or non-adiabatically leading to emission of electrons, photons or generation of electron-hole pairs [2].

of use of metal-semiconductor nanostructures in surface science. This technique will be discussed in a great detail in Section 1.2.

1.2 Use of nanostructures to study dissipation of chemical energy

1.2.1 The principle of detection of electronic excitations using nanostructures

As discussed in Section 1.1, highly exothermic chemical reactions on metal surfaces can lead to electronic excitations. If the energy of the excited electrons is higher that the work function of a metal, these electrons can be emitted into vacuum (exo-electron emission) and detected there. However, if the energy of the excited electrons is smaller than the work function of a metal, which is normally pretty big for metals used as catalysts (for example, the work function for platinum is in the range of $5.12 - 5.93$ eV), these electrons can not leave the metal surface and can not be detected outside the metal. Therefore, the existence of the electronic excitations during low energy catalytic chemical reactions and their importance were doubtful for a long time.

Recently, methods for the detection of the low energy electronic excitations in the course of surface chemical reactions with the use of composite nanostructures have been proposed in several studies. The earliest report, known to us, on the use of composite structures for the detection of electronic excitations in low energy gas-surface interactions have been done by Amirav, Tully and co-workers, who used p-i-n diodes to detect electron-hole pairs induced at a crystal surface by hyperthermal ($1 - 6$ eV) Xe, Ar, and Kr atoms [34, 35]. Further development of this method has been done in the works of McFarland, Nienhaus, Diesing, Hasselbrink & co-workers, who used nano thin metal-semiconductor Schottky and metal-insulator-metal structures to detect electron-hole pairs induced at metal surfaces during adsorption and surface reaction of hydrogen atoms [2, 5, 10, 11, 12, 36, 37, 38]. Finally, Somorjai, Park, Karpov & co-workers used this method to detect electron-hole pairs induced in the course of catalytic reactions, such as oxidation of carbon monoxide or hydrogen, with the use of nano thin metal-semiconductor structures [6, 7, 8, 13, 14, 39, 40, 41].

In order to understand the essence of the use of composite nanostructures for detection of the electron-hole pairs during catalytic chemical reactions, let us first consider a metal-semiconductor Schottky nanostructure based on an n-type semiconductor, Figure 1.3a. As discussed in Sections 1.3 and 1.4, when gas particles interact with the metal surface significant energy can be released. This energy can be partly dissipated as heat, which leads simply to heating of the metal. In addition, some of the energy can be transferred

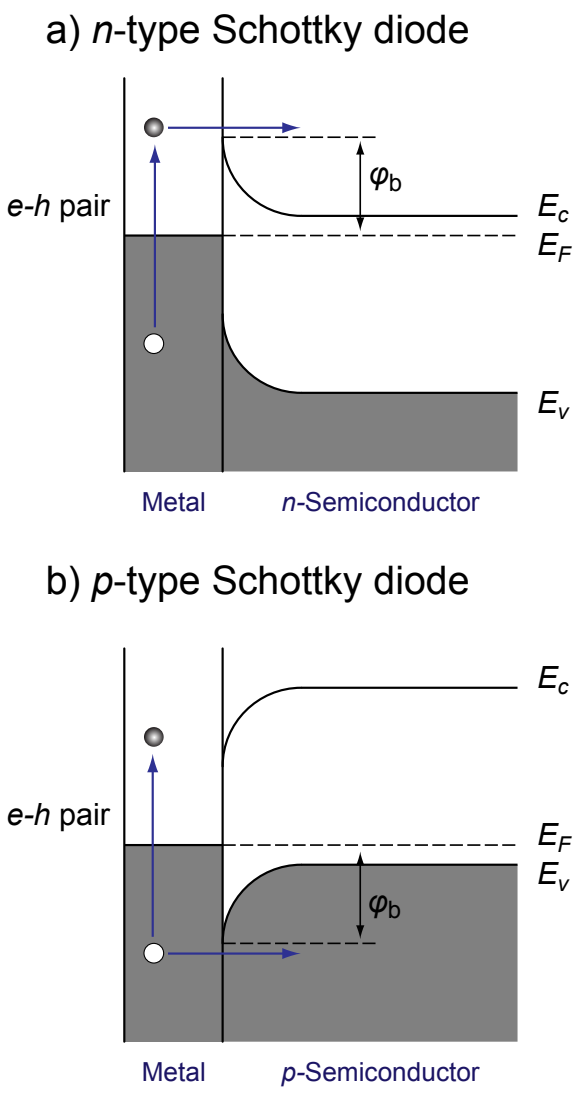

Figure 1.3: Principle of the chemicurrent study of the chemical energy dissipation with the use of a) n-type Schottky structures, and b) p-type Schottky structures.

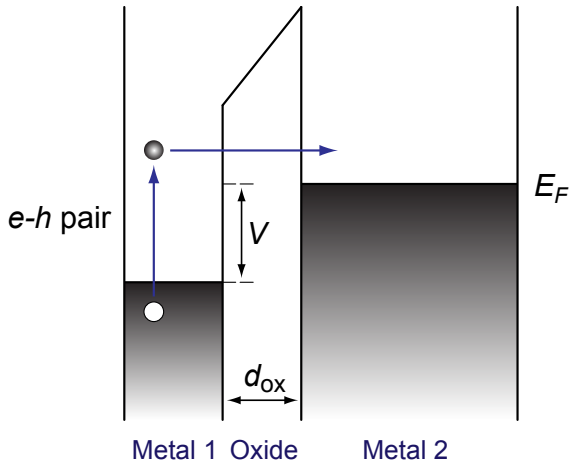

Figure 1.4: Principle of the chemicurrent study of the chemical energy dissipation with the use of metal-insulator-metal nanostructures.

to electrons of the metal, which results in the generation of the energetic electron-hole pairs. These excited charge carriers can travel from the surface of the metal film toward the metal-semiconductor interface without significant attenuation. Further, in the metal-semiconductor nanostructures based on the n-type semiconductors only excited electrons can overcome the potential barrier, denoted as φ_{b} in Figure 1.3, and be detected as an electric current (called **chemicurrent**). The chemicurrent is typically detected in the absence of an applied bias and is analogous to a photocurrent in a photodiode. An important feature of the metal-semiconductor structures is that they have fixed potential barrier heights, which are predominantly determined by the material parameters and which cannot be adjusted by an external electrical potential. Depending on the metal and the interface properties, the potential barrier heights in the metal-semiconductor nanostructures range between 0.2 and 1.0 eV. Metal-semiconductor Schottky nanostructures based on p-type semiconductors work in a similar way, Figure 1.3b. However, they allow for detection of the chemically excited holes.

Metal-semiconductor nanostructures have the highest sensitivity among all the composite nanostructures proposed for detection of the chemicurrent up to date. This is due to the fact that the potential barrier in such structures is relatively small. As a rule, sensitivity of the devices used for detection of the chemicurrent is characterized by a value of quantum yield, which is a number of charge carriers detected per one molecule formed on the surface of the device during a chemical reaction. For metal-semiconductor nanostructures this parameter is in the range of $10^{-5} - 10^{-2}$. However, due to a very high sensitivity of the structures of this type to some secondary effects (such as light and fluctuations of the temperature) the use of them to study catalytic reactions is limited.

In order to overcome the limitations of metal-semiconductor nanostructures, Diesing and Hasselbrink suggested to use metal-insulator-metal (also called metal-oxide-metal) nanostructures. These structures consist of two metal electrodes separated by a thin metal oxide layer, Figure 1.4. Since the thickness of the oxide layer in such structures is only several nanometers chemically excited charge carriers can be transported from the top metal electrode to the bottom metal electrode via quantum mechanical tunneling. Therefore, these structures allow detection of the charge carriers even when their energy is smaller than the potential barrier height at the metal-oxide interface.

When compared with the metal-semiconductor nanostructures, chemicurrent detectors based on the metal-oxide-metal structures have several advantages. First of all, these detectors are less sensitive to light, which can be produced by a source of chemically active particles (such as a source of atomic hydrogen) or generated by a chemical reaction (chemiluminescence). Indeed, the value of the band gap in metal oxides is notably bigger than in semiconductors, being in the range of $4.0 - 8.0$ eV, which dramatically reduces the probability of the band-to-band excitation of electron-hole pairs due the light absorption. In addition, the higher potential barrier in metal-oxide-metal structures ($\varphi_{\mathrm{b}} = 1.0 - 1.5$ eV) limits photocurrents due to the transport of electrons and holes exited in metal electrodes. Secondly, due to an extremely small thickness of the metal-oxide-metal nanostructures and the use of materials with poor thermoelectric properties these structures are less sensitive to the temperature fluctuations, which are unavoidable when exothermic chemical reactions take place on the surface of the nanostructures. In addition, the height of the potential barrier in the metal-oxide-metal nanostructures can be varied by an applied voltage bias, which allows making spectroscopy of the chemically excited charge carriers [38].

Besides the advantages listed above of the metal-oxide-metal nanostructures there are also several significant intrinsic drawbacks associated with these structures, such as relatively small sensitivity (quantum yield is in the range of $10^{-5} - 10^{-4}$) and low stability. The last fact is a result of the small thickness of the oxide layer, which can be easily destroyed by a high temperature or a voltage bias applied to the nanostructure. In addition, conductive properties of the oxide layer can be significantly modified due to the presence of some reactive gases [42].

In order to combine stability and sensitivity of metal-semiconductor nanostructures with the additional options typical for metal-oxide-metal nanostructures, in this work we study the possibility of the use a metal-oxide-semiconductor detector of the chemically excited charge carriers, which is schematically shown in Figure 1.5. This detector is similar to a regular metal-semiconductor structure shown in Figure 1.3 to which a moderately thick oxide layer ($d_{\mathrm{ox}} = 100$ nm) is added. The use of metal-oxide-semiconductor nanostructures for detection of chemicurrents as well as advantages of these structures over regular metal-semiconductor nanostructures have been already discussed in the liter-

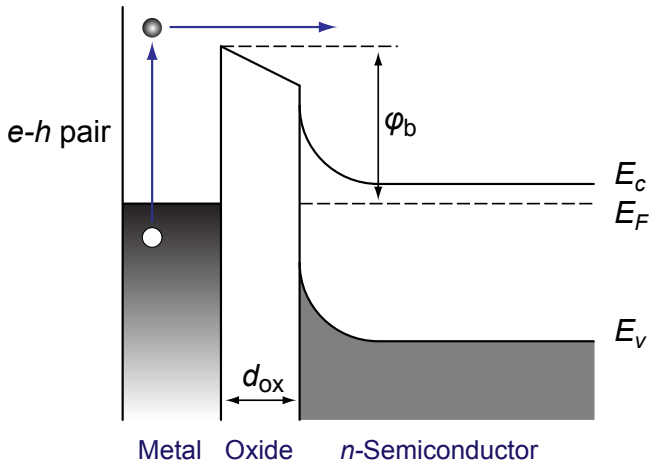

Figure 1.5: Principle of the chemicurrent study of the chemical energy dissipation with the use of metal-oxide-semiconductor nanostructures.

ature [10]. In particular, it has been shown that due to a possibility of varying the height of the potential barrier by a voltage bias, metal-oxide-semiconductor nanostructures allow for detection of chemically excited charge carriers generated in low energy surface events as typical for adsorption of molecular species. However, systematic chemicurrent studies with the use of structures of this type are still missing.

Basic properties of the metal-oxide-semiconductor nanostructures used in this work as well as mechanisms of charge carriers transport in these structures are described in Chapter 2, while details of the fabrication of these structures are given in Chapter 3.

Despite the diversity of the composite nanostructures used for detection of the chemicurrent, the detection principle of the chemically excited charge carriers can be describe by a three-step scheme for all of them: (1) excitation of the electron-hole pair in the course of an exothermic surface chemical event, (2) transport of the charge carriers from the surface to the interface (either metal-semiconductor or metal-oxide), and (3) transmission over or through (tunneling) the barrier, when the excited charge carriers can be detected as an electric current. As shown in Reference [2], the transport of the energetic charge carriers (step 2) through the top metal electrode happens ballistically, which means that these charge carriers experience negligible electrical resistivity caused by scattering while they are moving. However, this process is very short in time, being on the order of tens femtoseconds. The distance which excited charge carriers can overcome during this time (this value is called the **mean free path**) depends on the energy of the charge carriers and the sort of metal. Obviously, the detection of electron-hole pairs (step 3) is possible only under the condition that the mean free path of the excited charge carriers is comparable to the thickness of the top electrode of the composite nanostructures.

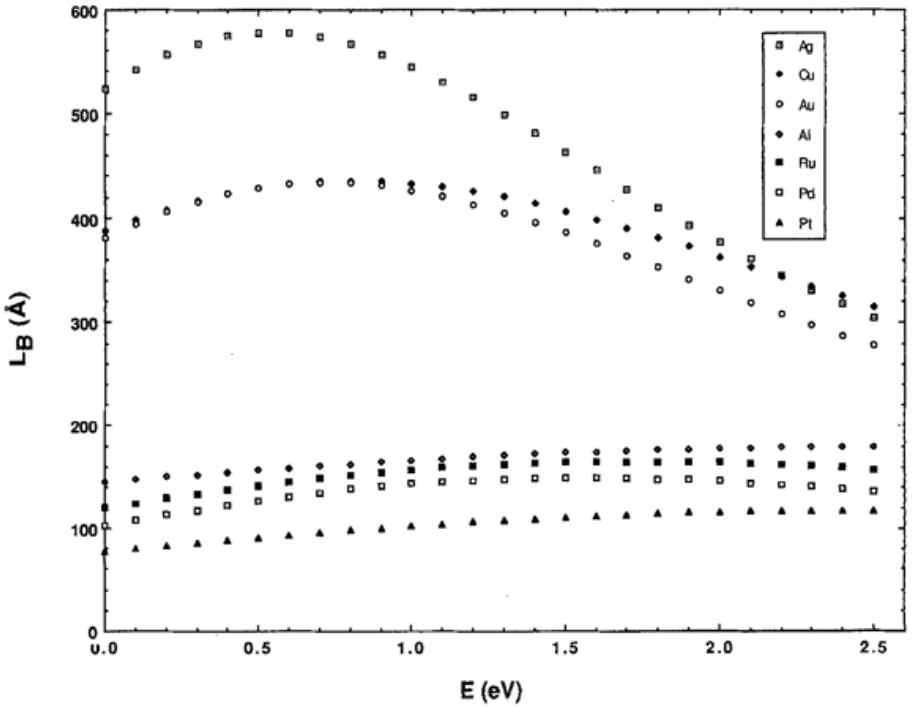

Figure 1.6: Calculated values of the ballistic mean free path as a function of the excess kinetic energy above the Fermi level for various metals. (Taken from Reference [43])

Otherwise, these excited charge carriers will dissipate their energy before they reach the metal-semiconductor or metal-oxide interface. Therefore, let us estimate the value of the mean free path for electrons in metals used for fabrication of the chemicurrent detectors.

According to Frese & co-workers, the mean free path of ballistic electrons (L_{B}) can be calculated as [43]

$$\frac{1}{L_{\mathrm{B}}} = \frac{1}{\lambda_{\mathrm{c}}} + \frac{1}{\lambda_{\mathrm{e-e}}}\,, \tag{1.11}$$

where λ_{c} is the mean free path associated with the crystal lattice and $\lambda_{\mathrm{e-e}}$ is the electron-electron scattering length. Theoretical models suggest, that the first term of Equation 1.11 should increase as E^2, therefore Crowell and Sze proposed [43]

$$\lambda_{\mathrm{c}} = \lambda_{\sigma} \left(\frac{E_{\mathrm{F}} - \Delta E}{E_{\mathrm{F}}} \right)^2 . \tag{1.12}$$

Here E_{F} is the Fermi level and ΔE is the excess kinetic energy above the Fermi level. Scattering of the energetic electrons by electrons can be described by Quinn's theory [44].

Therefore the second term of Equation 1.11 can be written [43]

$$\lambda_{\mathrm{e-e}} = \frac{14.5\,(E_{\mathrm{F}}\beta)^{3/2}E}{(m^*)^{1/2}\left[\tan^{-1}(\beta^{-1/2}) + \dfrac{\beta^{-1/2}}{(1+\beta)}\right]}(E - E_{\mathrm{F}})^{-2}\,, \tag{1.13}$$

where $\beta = (4/9)^{1/3}(r_{\mathrm{s}}/\pi)$, r_{s} is the radius of a sphere which on average contains one electron (Wigner-Seitz cell), and m^* is the electron effective mass.

Calculated values of the ballistic mean free path for different metals are shown in Figure 1.6. This figure is taken from Reference [43]. One can see, that for commonly used catalytic metals (Pt, Pd and Ru) the mean free path does not exceed 200 Å. This value indicates the maximum suitable value for the thickness of the top electrode for the composite nanostructures used as detectors of the chemicurrent.

1.2.2 Thermoelectric effects

In some cases the rate of energy release in the course of a surface chemical reaction can be so large that the temperature of the nanostructure, which is used for detection of the electronic excitations, is significantly higher than the ambient one and a temperature gradient across the nanostructure is practically unavoidable. This temperature gradient can cause an electric current for two reasons: (1) the Seebeck effect in the layers of the nanostructure, (2) the thermionic emission at the interfaces. These currents (hereafter referred to as thermal currents) will be superimposed to the chemicurrent, which is the real object of the studies, hampering the unambiguous interpretation of the experiments. Hence, in this section, we consider basic thermal processes in metal-semiconductor nanostructures, induced by surface exothermic chemical reactions, and estimate the related mechanisms of the thermal currents generation.

Chemicurrent studies in MS nanostructures utilize fairly high-mobility semiconductors, such as Si, GaN, GaP, TiO_2 and SiC, with moderate dopant concentrations. Current-voltage characteristics of such structures are adequately described by Bethe's thermionic emission theory [45, 46].

First, consider a MS nanostructure such as sketched in Figure 1.7 under conditions where no external energy is fed to the top metal electrode. The current density of electrons from the semiconductor to the metal $J_{\mathrm{S}\to\mathrm{M}}$, noted as process 2 in Figure 1.7, for a potential (Schottky) barrier of height φ_b at the MS interface is given by

$$J_{\mathrm{S}\to\mathrm{M}} = A^*\,T_{\mathrm{S}}^2 \exp\left(-\frac{e\varphi_b}{k_{\mathrm{B}}T_{\mathrm{S}}}\right)\exp\left(\frac{qU_{\mathrm{bias}}}{k_B T_{\mathrm{S}}}\right), \tag{1.14}$$

where T_{S} is the temperature of the semiconductor in the region near the MS interface, $A^* = 4\pi e m^* k_{\mathrm{B}}^2/h^3$ the effective Richardson constant, m^* the effective mass of an electron

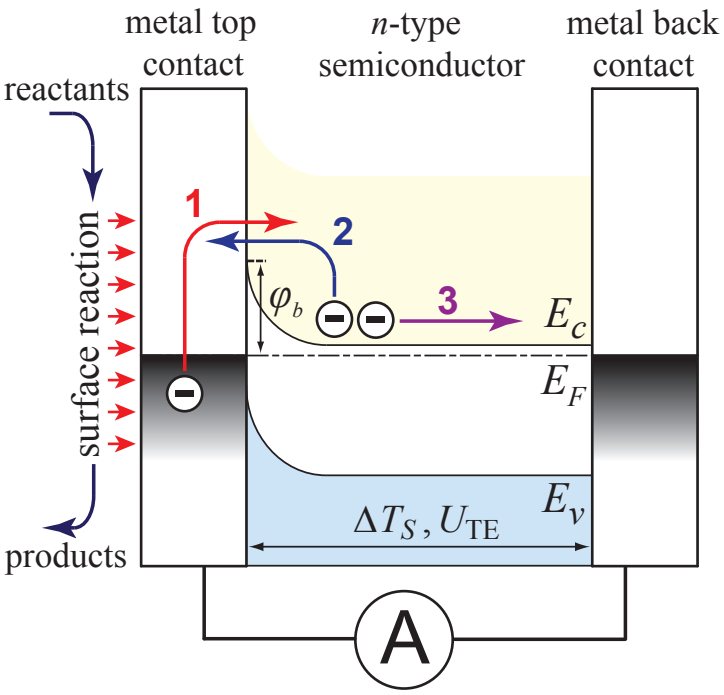

Figure 1.7: Charge carrier transport in a metal-semiconductor nanostructure: 1) and 2) thermionic emission currents of electrons, 3) thermal drift of electrons (Seebeck effect). Here φ_b - Schottky barrier height, E_F - Fermi level of electrons, E_C - conduction-band bottom, E_V - valence-band top, ΔT_{S} - temperature difference in the semiconductor layer, and U_{TE} - thermoelectric power.

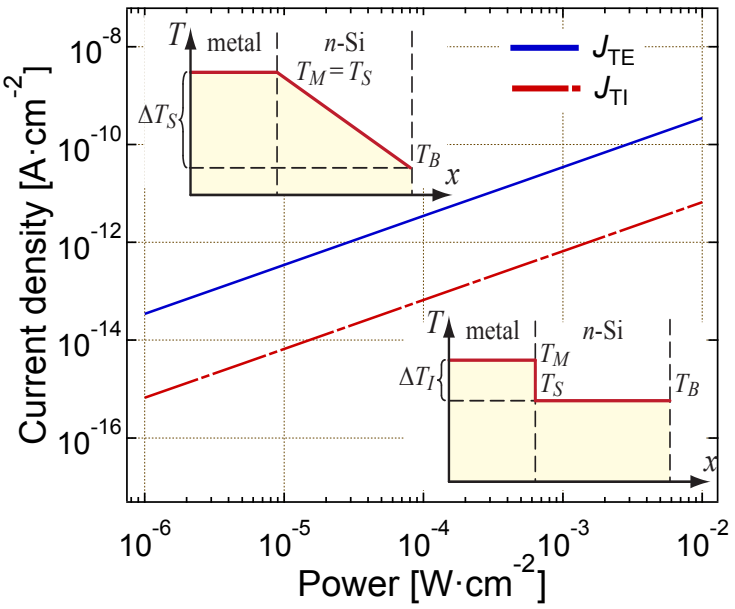

Figure 1.8: Calculated thermoelectric current in a metal/n-Si nanostructure at 300 K as a function of the heating power: J_{TE} – thermoelectric current, J_{TI} – thermionic emission current. Insets show a schematic drawing of the temperature distribution in the metal/n-Si structure in case of (top) thermoelectric current J_{TE} and (bottom) thermionic emission current J_{TI}.

in the semiconductor, q is the elementary charge, and k_{B} the Boltzmann constant. U_{bias} is the voltage bias applied across the MS structure.

For $U_{\mathrm{bias}} = 0$ and equilibrium conditions, this current will be balanced by a reverse current $J_{\mathrm{M}\to\mathrm{S}}$, shown as process 1 in Figure 1.7. Hence, we can write for this current similarly to Equation 1.14 [46]:

$$J_{\mathrm{M}\to\mathrm{S}} = -A^* T_{\mathrm{M}}^2 \exp\left(-\frac{q\varphi_b}{k_{\mathrm{B}} T_{\mathrm{M}}}\right). \tag{1.15}$$

Here T_{M} is the temperature of the top metal electrode. The net current density then is equal to zero, i.e. $J = J_{\mathrm{S}\to\mathrm{M}} - J_{\mathrm{M}\to\mathrm{S}} = 0$.

Now consider the same MS nanostructure when an exothermic chemical reaction with a constant rate (stationary state) takes place on its surface. Generally, dissipation of chemical energy is accompanied by both release of heat and excitation of hot charge carriers in the top electrode [5, 47, 36, 2, 11]. However, for the sake of simplicity we assume that the chemical energy is dissipated only as heat. Thus, we estimate the upper limit for the thermal current induced in the MS nanostructure by the chemical reaction. For this purpose, we assume that (1) the chemical reaction can be regarded as a heat source of constant power attached to the top metal electrode, (2) radiative and convective heat losses from the top metal electrode are not significant, and (3) the temperature of the back

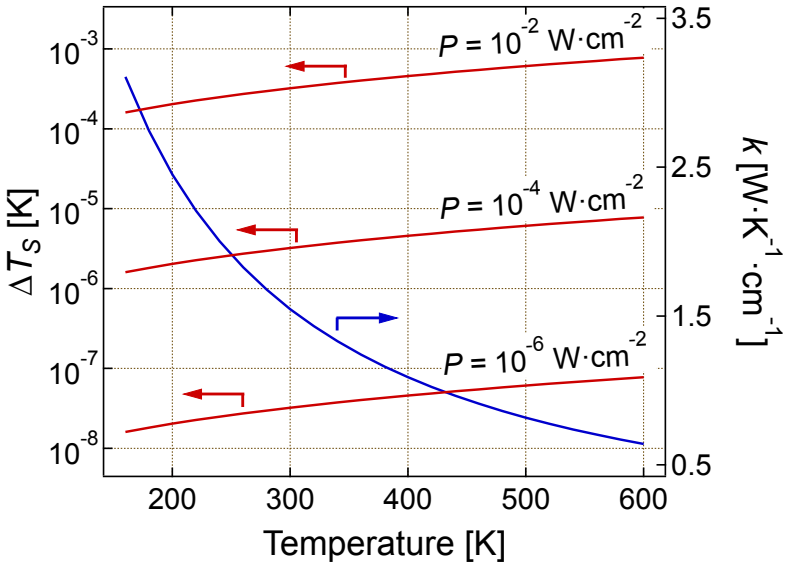

Figure 1.9: Temperature dependence of the calculated thermal conductivity k_{Si} and the temperature difference ΔT_{S} across the silicon layer with $d_{\mathrm{Si}} = 525$ μm thickness for the varied heating power.

contact T_B remains constant, such as it would be connected to an efficient heat sink. The range of heating powers considered, $P = 10^{-6} - 10^{-2}$ W·cm^{-2}, was chosen so as to cover values reported elsewhere [2, 3, 5, 6, 7, 8, 11, 15, 48, 13, 14, 36, 49, 50, 47, 37, 51, 52, 53, 39, 54, 40, 16] in studies of such chemical reactions as the chemisorption of atomic hydrogen (typical beam fluxes are between 2×10^{12} and 2.5×10^{14} atoms cm^{-2}·s^{-1}), carbon monoxide oxidation and water formation (turnover frequency TOF < 100 molecules·site^{-1}·s^{-1}).

The limited heat conductivity results in a temperature difference across the MS structure. In general, this difference is the sum of three components:

$$\Delta T = \Delta T_{\mathrm{M}} + \Delta T_{\mathrm{I}} + \Delta T_{\mathrm{S}}, \tag{1.16}$$

where ΔT_{M} and ΔT_{S} are the temperature differences across the top metal electrode and the semiconductor layer, respectively. Both can be found using the one-dimensional Fourier equation:

$$P = k\,\frac{\Delta T}{d}, \tag{1.17}$$

where P is the heating power per cm^2, k the thermal conductivity, and d the thickness of a material. Finally, $\Delta T_{\mathrm{I}} = T_{\mathrm{M}} - T_{\mathrm{S}} = R_{\mathrm{I}}P$ is the temperature drop across the MS interface which is characterized by the thermal (Kapitza) resistance R_{I}.

Next, we look at the value of each component of ΔT given by Equation 1.16 at a base temperature of 300 K, starting with the temperature difference in the top metal electrode ΔT_{M}. Taking into account the high thermal conductance, typical for metals, and the fact that the top electrode thickness should not exceed the mean free path of hot electrons

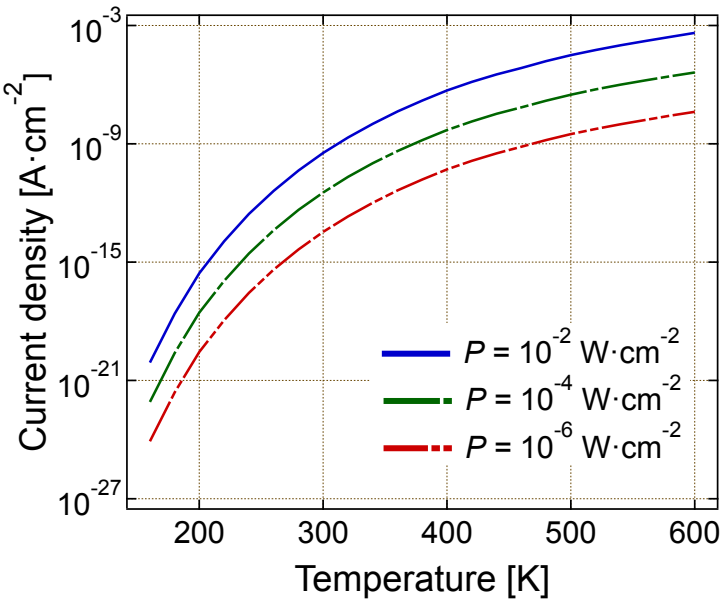

Figure 1.10: Temperature dependence of the calculated thermoelectric current in a metal/n-Si nanostructure for various heating powers.

($<$ 15 nm for most metals) one should expect extremely small values of ΔT_{M}. Indeed, solving Equation 1.17 for e.g. Ag ($k_{\mathrm{Ag}} = 4.29$ W·K^{-1}·cm^{-1}), which often served as the top electrode in chemicurrent studies [5, 47, 36, 2], with a thickness $d_{\mathrm{M}} = 10$ nm, we obtain $\Delta T_M = 10^{-13} - 10^{-9}$ K. In order to estimate the magnitude of ΔT_{I} and ΔT_{S}, we consider a MS nanostructure based on a moderately doped ($N_D \leq 10^{17}$ cm^{-3}) n-type silicon layer with the thickness $d_{\mathrm{Si}} = 525$ μm. Then, using a value of an interfacial thermal resistance $R_{\mathrm{I}} = 10^{-4}$ cm^2·K·W^{-1} [55] for the considered range of heating powers we obtain $\Delta T_{\mathrm{I}} = 10^{-10} - 10^{-6}$ K. At the same time, taking the value of thermal conductivity for silicon $k_{\mathrm{Si}} = 1.56$ W·K^{-1}·cm^{-1} [56] and evaluating Equation 1.17 we obtain $\Delta T_{\mathrm{S}} = 10^{-8} - 10^{-4}$ K. This suggests that we can neglect ΔT_{M} in the following discussion as it is three orders of magnitude smaller than ΔT_{I} and five orders of magnitude smaller than ΔT_{S}.

Both ΔT_{I} and ΔT_{S} may be the reason of a temperature gradient induced current in the MS nanostructure. However, the mechanisms of the current generation are different. Namely, the presence of ΔT_{I} upsets the balance of the currents given by Equations 1.14 and 1.15 at the MS interface and leads to a nonzero total thermionic emission current. In the absence of an applied bias voltage the current density is given by:

$$J_{\mathrm{TI}} = A^* T_{\mathrm{S}}^2 \exp\left(-\frac{q\varphi_b}{k_{\mathrm{B}} T_{\mathrm{S}}}\right) - A^* T_{\mathrm{M}}^2 \exp\left(-\frac{q\varphi_b}{k_{\mathrm{B}} T_{\mathrm{M}}}\right). \tag{1.18}$$

ΔT_{S} also causes a thermal current, but it arises as a result of the electric charge redistribution in the semiconductor layer (for n-type semiconductors electrons drift toward the colder region, process 3 in Figure 1.7) and generation of an electric field (Seebeck

effect). Consequently, the potential barrier for electrons flowing from the semiconductor to the metal changes by the magnitude of the thermoelectric power, $U_{\mathrm{TE}} = S\,\Delta T_{\mathrm{S}} - IR_{\mathrm{ser}}$, where S is the semiconductor's Seebeck coefficient, I the total current through the MS nanostructure, and R_{ser} the series resistance. This effect is equal to adding a voltage source in series with the MS contact [16] and invokes the thermoelectric current:

$$J_{\mathrm{TE}} = A^{*}T_{\mathrm{S}}^{2}\exp\left(-\frac{q\varphi_b}{k_{\mathrm{B}}T_{\mathrm{S}}}\right)\exp\left(\frac{q(S\,\Delta T_{\mathrm{S}} - IR_{\mathrm{ser}})}{k_{\mathrm{B}}T_{\mathrm{S}}}\right) - A^{*}T_{\mathrm{M}}^{2}\exp\left(-\frac{q\varphi_b}{k_{\mathrm{B}}T_{\mathrm{M}}}\right). \quad (1.19)$$

Thermal currents calculated for a metal/n-Si nanostructure using Equations 1.18 and 1.19 with the previously estimated values of ΔT_{I} and ΔT_{S} are shown in Figure 1.8. The calculations are performed using values of the effective Richardson's constant $A^{*} = 120$ A·K^{-2}·cm^{-2} (as for n-type silicon), Seebeck coefficient $S = -1.55 \times 10^{-3}$ V·K^{-1} [57, 58], potential barrier height $\varphi_b = 0.7$ eV and the back contact temperature $T_{\mathrm{B}} = 300$ K. We also assumed that the temperature profile in the metal/n-Si structure corresponds to that shown in the inset of Figure 1.8. Thus, the thermoelectric current density J_{TE} was calculated for the condition that $T_{\mathrm{M}} = T_{\mathrm{S}}$ ($\Delta T_{\mathrm{I}} = 0$) and the temperature difference in the metal/n-Si nanostructure $\Delta T = \Delta T_{\mathrm{S}} = T_{\mathrm{S}} - T_{\mathrm{B}}$. To calculate the thermionic emission current density J_{TI} we assumed that $T_{\mathrm{S}} = T_{\mathrm{B}}$ ($\Delta T_{\mathrm{S}} = 0$) and $\Delta T = \Delta T_{\mathrm{I}} = T_{\mathrm{M}} - T_{\mathrm{S}}$. As can be seen, the thermoelectric current is in the range of $J_{\mathrm{TE}} = 10^{-14} - 10^{-10}$ A·cm^{-2}, which is almost two orders of magnitude larger than the thermionic emission current J_{TI}. Hence, we conclude that the thermoelectric properties of the semiconductor layer is the main factor determining the magnitude of the thermal current generated in a MS nanostructure in case of a stationary chemical reaction. However, one can not rule out a dominant role of the thermionic emission current for transient processes or in case of MIM nanostructures, which are usually based on materials with poor thermoelectric properties.

Here we also note, that the metal/n-Si nanostructures, considered in this article, have stronger thermoelectric properties than some other systems, which are often used in the chemicurrent studies. For instance, the thermoelectric current J_{TE} calculated in a similar way as discuss above for such structures as metal/n-GaN and metal/n-TiO_2 will be smaller. For $\Delta T_{\mathrm{S}} = 10^{-8} - 10^{-4}$ K we obtain J_{TE} in the range of $10^{-15} - 10^{-11}$ A·cm^{-2} for metal/n-GaN, and $10^{-16} - 10^{-12}$ A·cm^{-2} for metal/n-TiO_2 at $T_{\mathrm{B}} = 300$ K.

In order to investigate the effect of temperature on the value of the thermoelectric current J_{TE} we calculated the temperature dependence of ΔT_{S} using Equation 1.17 taking into account the strong temperature dependence of the thermal conductivity of silicon, which can be approximated by $k_{\mathrm{Si}}^{-1} = a + bT + cT^{2}$ [56], with $a = 0.03$ cm·K·W^{-1}, $b = 1.56 \times 10^{-3}$ cm·W^{-1}, and $c = 1.65 \times 10^{-6}$ cm·K^{-1}·W^{-1}. In addition, we used the temperature dependence of the Seebeck coefficient S, adopted from [57, 58]. The height of the Schottky barrier, $\varphi_b = 0.7$ eV, was assumed to be independent of temperature.

Figure 1.9 shows the temperature dependence of the calculated thermal conductivity

(k_{Si}) and the temperature difference in the silicon layer (ΔT_{S}) for three values of the heating power. As can be seen, an increase of the thermal conductivity of silicon leads to smaller values of ΔT_{S} at low temperatures. Corresponding values of the thermoelectric current density (J_{TE}) are shown in Figure 1.10. Below 200 K the thermoelectric current drops to less than 10^{-15} A·cm^{-2}. Such a current is $7-8$ orders of magnitude smaller than the current of hot charge carriers observed during the chemisorption of atomic hydrogen on the surface of Ag/n-Si and Cu/n-Si structures [47, 5, 36, 2] and can be neglected. This finding also agrees well with the conclusion drawn by the authors reporting a chemicurrent for Mg/p-Si diodes [52]. There the authors suggested the inability of thermal effects to induce any measurable current in MS nanostructures at low temperatures. On the other hand, Figure 1.10 predicts that significant thermoelectric currents in the range of $10^{-10} - 10^{-3}$ A·cm^{-2} can be detected at temperatures above 400 K. It should be noted here that the magnitude of the thermoelectric power (U_{TE}) responsible for the current J_{TE} shown in Figure 1.10 is rather small, being in the range of $10^{-11} - 10^{-6}$ V for the temperature interval from 160 to 600 K. When seen together with the fact that chemicurrents reported up to date do not exceed $10^{-7} - 10^{-5}$ A·cm^{-2} [8, 14, 13, 39, 54, 40, 6, 7, 16] these results indicate the need for a particularly thorough control of temperature gradients in MS nanostructures at elevated temperatures to allow the separation of the thermal current and the chemicurrent. Traditional approaches for the temperature measurement (resistance temperature detectors or thermocouple sensors, attached to the surface of the nanostructure) are not sufficient in case of heterostructures of the nanometer thickness due to a large heat capacity of the sensor. Thus, noninvasive techniques of temperature measurement may be needed [59]. In addition, the use of MIM nanostructures, usually based on wider band gap metal oxide nanofilms [11, 48, 3] which strongly suppress thermoelectric currents, seems to be more preferable for the study of chemicurrent at high temperatures.

1.3 Water formation reaction on a platinum surface

Catalytic combustion over the surface of a metal is an important technological process [60, 61, 62, 63]. Water formation is a well known prototype reaction, which is often used to study the surface combustion. Thus, there are many articles which report on the progress in understanding the water formation reaction over the surface of single crystal and polycrystalline platinum. These include ultra high vacuum (UHV) and high pressure studies of both experimental and theoretical character [60, 61, 62, 63, 64, 65, 66, 67, 68].

There are many models, which describe the formation of water on the Pt surface. However, despite the big number of proposed schemes, all of them depict the dominant step of the reaction as a process, which follows the Langmuir-Hinshelwood mechanism [60, 61, 62]. In this work we will follow the model of the water formation reaction, which is

suggested by Schmidt & co-workers [61] and Zhdanov & co-workers [62]. This model includes such steps as

1. Adsorption and desorption of hydrogen, oxygen, and water molecules

$$\mathrm{H_2}(g) \underset{k_{\mathrm{dH}}}{\overset{k_{\mathrm{aH}}}{\rightleftharpoons}} 2\mathrm{H}(a) \tag{1.20}$$

$$\mathrm{O_2}(g) \underset{k_{\mathrm{dO}}}{\overset{k_{\mathrm{aO}}}{\rightleftharpoons}} 2\mathrm{O}(a) \tag{1.21}$$

$$\mathrm{H_2O}(g) \underset{k_{\mathrm{dW}}}{\overset{k_{\mathrm{aW}}}{\rightleftharpoons}} \mathrm{H_2O}(a) \tag{1.22}$$

2. Desorption of OH at high temperatures

$$\mathrm{OH}(a) \xrightarrow{k_{\mathrm{dOH}}} \mathrm{OH}^*(g) \tag{1.23}$$

3. Surface reactions between adsorbed species

$$\mathrm{H} + \mathrm{O} \underset{k_{-1}}{\overset{k_1}{\rightleftharpoons}} \mathrm{OH} \tag{1.24}$$

$$\mathrm{H} + \mathrm{OH} \underset{k_{-2}}{\overset{k_2}{\rightleftharpoons}} \mathrm{H_2O} \tag{1.25}$$

$$2\mathrm{OH} \underset{k_{-3}}{\overset{k_3}{\rightleftharpoons}} \mathrm{H_2O} + \mathrm{O} \tag{1.26}$$

$$\mathrm{H} + \mathrm{H} + \mathrm{O} \underset{k_{-4}}{\overset{k_4}{\rightleftharpoons}} \mathrm{H_2O} \tag{1.27}$$

Here k_{aH}, k_{aO}, k_{aW} are the adsorption rates, and k_{dH}, k_{dO}, k_{dW}, k_{dOH} are the desorption rates for hydrogen, oxygen and OH radicals respectively. Finally, $k_{\pm1}$, $k_{\pm2}$, $k_{\pm3}$, $k_{\pm4}$ are the rates for different steps of the surface reaction of water formation. This mechanism assumes that the water formation reaction on the platinum surface involves only H, O, OH, and H_2O species, while other species, which are also discussed in the literature (for example H_2O_2 [63] and H_3O^+ [69]), are not included. Direct reactions between molecular hydrogen and oxygen, leading to formation of water molecules on platinum, are also not included in this mechanism, since such processes have not been confirmed experimentally yet [61, 62]. As mentioned in Reference [62], step 1.27 can be ignored in most cases. Indeed, at high temperatures the hydrogen coverage is very low, therefore, step 1.27 is not important. It can be also ignored at low temperatures, since three-particle interactions are usually considered to be rare. Thus, in the following discussion we will focus mostly on steps 1.25 and 1.26.

The water formation reaction on the Pt surface is an exothermic reaction, which liberates around 2.5 eV (243 kJ/mol) for the case of $H_2(g)+1/2O_2(g) \rightarrow H_2O(g)$ reaction,

and around 3.6 eV (351 kJ/mol) for the case of $H_2(g)+O_2(g) \rightarrow H_2O(g)+O(a)$ reaction per one water molecule formed on the platinum surface [61]. This energy can give rise to a temperature increase of a catalyst or may lead to some other effects, such as excitation of electron-hole pairs. Search for evidences of the last process is the aim of this work. Therefore, consideration of the energetics of the individual steps of the water formation reaction is of special interest.

An energy diagram for the steps of the water formation reaction on the Pt surface is shown in Figure 1.11. This figure is redrawn on the basis of Figure 9 in Reference [61] and Figure 5 in Reference [62]. As can be seen, adsorption of oxygen and hydrogen particles on the platinum surface are among the most energetic steps of this reaction. For example, adsorption of oxygen releases around 2.25 eV, while adsorption of hydrogen liberates 0.78 eV. A surface reaction of a hydrogen atom with an OH radical, Equation 1.25, and a reaction of two OH radicals, Equation 1.26, leading to formation of a water molecule, are also highly energetic steps, which release around $1.3 - 1.6$ eV. However, these reactions require an activation energy of $0.5 - 0.65$ eV. Since the water formation reaction is known to be quite fast even at low temperatures ($T_{Pt} \geq 120$ K), the activation energy for OH radical formation is assumed to be very small in this mechanism (< 0.11 eV). In our opinion, all these reaction steps can lead to the excitation of electron-hole pairs with the energy high enough to overcome the potential barrier at the metal-oxide interface and be detected using metal-oxide-semiconductor nanostructures. As shown in Section 1.2, the height of this potential barrier in the metal-oxide-semiconductor nanostructures is in the range of $0.5 - 1.0$ eV.

As discussed in Section 1.2.2, thermoelectric effects in the composite nanostructures, induced by the chemical heat release, can cause some difficulties in the detection of the electron-hole pairs created due to the non-adiabatic effects of the energy dissipation. As shown, the value of these effects depends on the power of the chemical heat release. Thus, based on literature data let us estimate the order of magnitude of the power of the heat release during the water formation reaction on platinum, which could be expected in our experiments. In order to estimate the power of heat release during the water formation reaction on the Pt thin foil, Ljungström & co-workers [60] measured the electric power, which is necessary to maintain the constant temperature (1100 K) of the platinum foil, during the reaction and in its absence. The difference in the values of the measured electric power were identified as the power of the chemical heat release. Summarizing the data, obtained in the course of that work, the following conclusions can be done:

1. The maximal power of the chemical heat release is observed for the hydrogen + oxygen gas mixtures when the relative concentration of hydrogen is in the range of $\alpha = 0.15 - 0.25$ (this parameter is defined as $\alpha = P_{H_2}/(P_{H_2} + P_{O_2})$, where P_{H_2} is the partial pressure of hydrogen, and $P_{H_2} + P_{O_2}$ is the total pressure of the hydrogen + oxygen gas mixture).

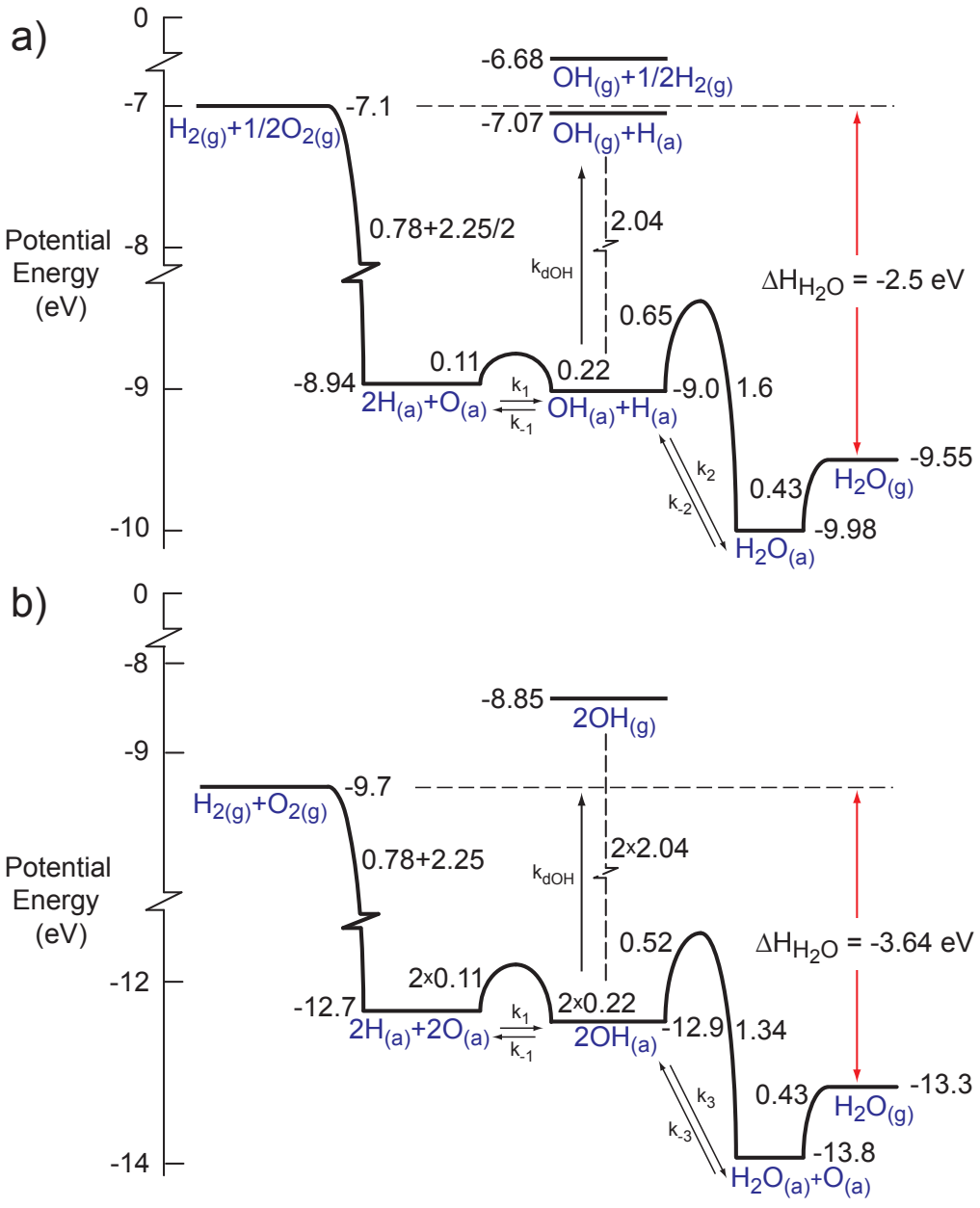

Figure 1.11: Energy diagram for a) reaction $H_2(g)+1/2O_2(g) \rightarrow H_2O(g)$ and b) reaction $H_2(g)+O_2(g) \rightarrow H_2O(g)+O(a)$ on platinum (Redrawn on the basis of Figure 9 in Reference [61] and Figure 5 in Reference [62]).

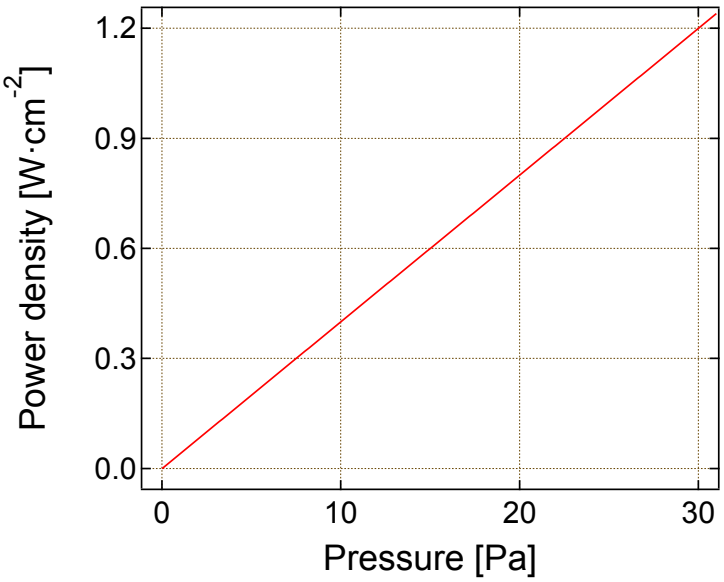

Figure 1.12: Power density of the heat release during the water formation reaction on the Pt thin foil as a function of the pressure of the hydrogen + oxygen gas mixture. (Redrawn on the basis of the data presented in Figure 8 [60]).

2. The power of the chemical heat release is linearly proportional to the total pressure of the hydrogen + oxygen gas mixture.

Based of the data presented by Ljungström & co-workers [60], we have calculated the power density of the heat release during the water formation reaction on the Pt thin foil as a function of the pressure of the hydrogen + oxygen gas mixture, see Figure 1.12. As can be seen, the power of the chemical heat release is of the order of watts per square centimeter.

Despite the fact that the water formation reaction is one of the best studied catalytic reactions, there is still some obscurity about individual steps of this process [61, 62]. Among them Zhdanov & co-workers mentioned (i) uncertainty regarding the determination of the relative importance of the elementary steps leading to formation of a water molecule and (ii) the magnitude of the activation energies for the intermediate reaction steps [62], which differs significantly with changing surface coverage, relative hydrogen concentration in the oxygen+hydrogen mixture, and other parameters. Schmidt & co-workers also indicated, that the water formation reaction on the Pt surface is characterized by very fast rates already at low temperatures, which makes it extremely difficult to determine the rates of intermediate surface reaction steps as well as register intermediate particles [61]. This problem becomes especially relevant when high-pressure gases react on a catalyst at high temperature, which is typical for industrial catalysis.

1.4 Adsorption of O_2 on a platinum surface

The adsorption of oxygen on a platinum surface is a key step of the water formation and many other catalytic reactions. Therefore, in the frame of this PhD work a study of the electric charge transfer induced by oxygen interactions with the polycrystalline Pt surface have been made. Results of this study are given in Section 5.2. In this section we will give a brief overview of the oxygen-platinum system based on the data already reported in the literature.

Using different experimental techniques (namely, low energy electron loss (EELS), ultraviolet photoemission (UPS), and thermal desorption (TDS) spectroscopies as well as low-energy electron diffraction (LEED)) it was found that three different types of oxygen bonding on the platinum surface can be identified. These are an adsorbed layer of molecular oxygen, atomic oxygen, and a layer of platinum oxide [70, 71, 72, 73, 74].

According to Gland & co-workers [70], oxygen adsorbs predominantly in molecular form when the temperature of platinum is below 120 K. According to TDS data, the heat of adsorption in this case is about 0.38 eV. The work function of platinum changes by +0.8 eV during oxygen adsorption, which indicates the electron transfer from platinum into the molecular oxygen layer [70, 75]. Combining these results with the UPS data, one can say, that the primary bond between molecular oxygen and platinum is formed by the electron transfer from the valence band of platinum into π_g^* orbitals of the adsorbed oxygen molecules [70].

When the temperature of platinum is in the range of $170 - 700$ K oxygen adsorbs predominantly in atomic form. As reported by Campbell & co-workers, dissociation of oxygen on the platinum surface may happen in two ways: directly and indirectly [71]. In the first case, an incident oxygen molecule dissociatively adsorbs on the Pt surface without being trapped in the molecular adsorbed state O_2(a). In the second case, O_2 is at first adsorbed as O_2(a), and then dissociates on atoms due to thermal activation. The heat of adsorption depends on the coverage (Θ) [70, 71]. At $\Theta = 0.02\,\Theta_{\max}$ the heat of oxygen adsorption on platinum is about 5.18 eV. However, at $\Theta = 0.2\,\Theta_{\max}$ it is already 2.59 eV. Finally, when $\Theta = 0.8\,\Theta_{\max}$ the heat of adsorption decreases to 1.66 eV.

Finally, when the temperature of platinum is in the range of $800-1000$ K the platinum surface can be oxidized [70, 76]. In contrast to oxygen atoms adsorbed on platinum, the platinum oxide layer is non-reactive if the temperature is below 1100 K.

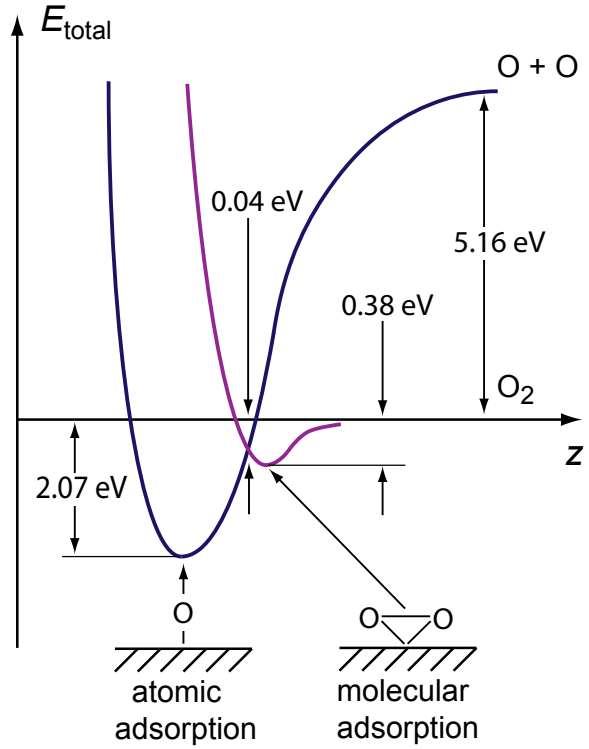

Figure 1.13: Schematics of the potential surface for interaction of oxygen with the platinum surface. (Redrawn on the basis of Figure 14 [70]).

Chapter 2

Physics of MOS structures

As mentioned above, this work aims to study the possibility of using metal-oxide-semiconductor nanostructures as detectors of hot charge carriers, excited during exothermic surface chemical reactions between oxygen and hydrogen species. Thus, it is important to consider basic properties as well as charge transport mechanisms responsible for the electrical conductance of these nanostructures.

Information given in this chapter is not obtained in the course of this PhD work. It is a review based on the data previously published by other authors.

2.1 Ideal MOS structure

The metal-oxide-semiconductor (MOS) structure was proposed back in 1959 by Moll, Pfann and Garrett [77, 78]. However, MOS structures based on Si-SiO_2 remain the most often practically used metal-oxide-semiconductor structure to date [46].

Cross sectional view of an ideal MOS structure, in its simplest form, is shown in Figure 2.1a. It consists of a metal electrode, which is separated from a semiconductor substrate by an oxide film. The thickness of the oxide film is denoted as d_{ox}. For the possibility of creating an electric field inside the MOS structure, an ohmic contact is added to the back side of the semiconductor substrate.

The energy-band diagram for the ideal MOS structure at equilibrium (without any voltage bias) is shown in Figure 2.1b. Here q is the elementary charge, χ and χ_i are the electron affinities for semiconductor and oxide respectively, $q\varphi_m$ is the work function of a metal electrode, E_g is the band gap, E_C is the conduction band edge, E_V is the valence band edge, E_F is the Fermi level of the semiconductor.

According to Reference [46], an ideal MOS structure can be defined as: (1) the structure where electric charges can exist in the semiconductor and on the metal surface adjacent to the oxide film under any biasing conditions, i.e. there are no interface traps nor oxide charges; (2) the structure where the charge transport through the oxide film is not possible under DC biasing conditions. For simplicity, it is also often assumed that

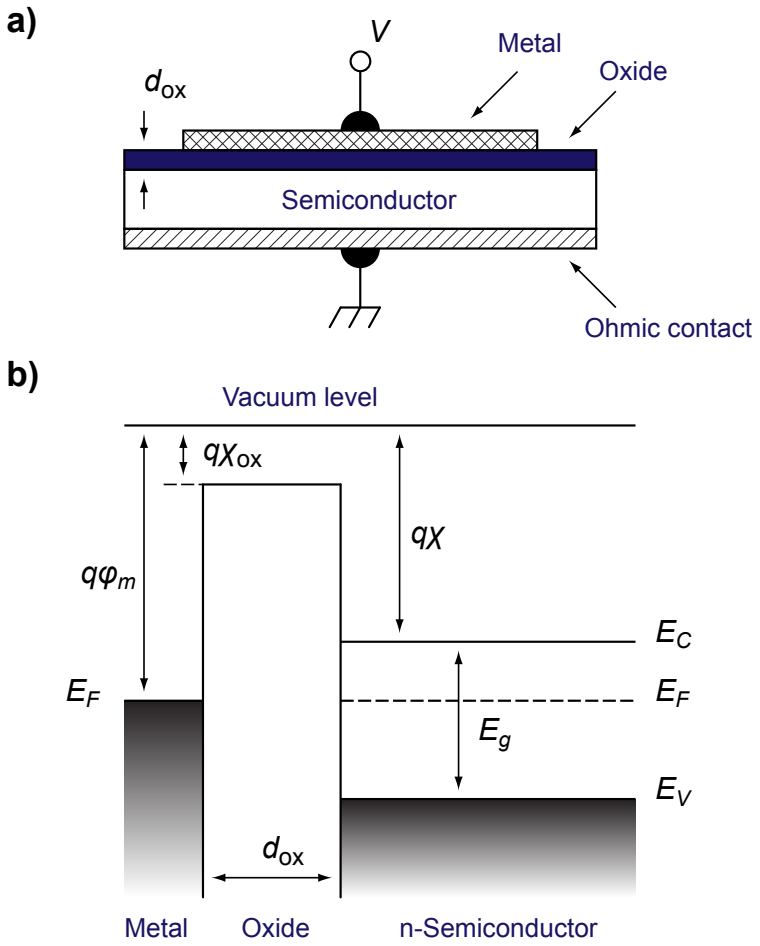

Figure 2.1: a) Cross-sectional view and b) energy-band diagram for an ideal MOS structure based on n-type semiconductor at equilibrium ($V = 0$).

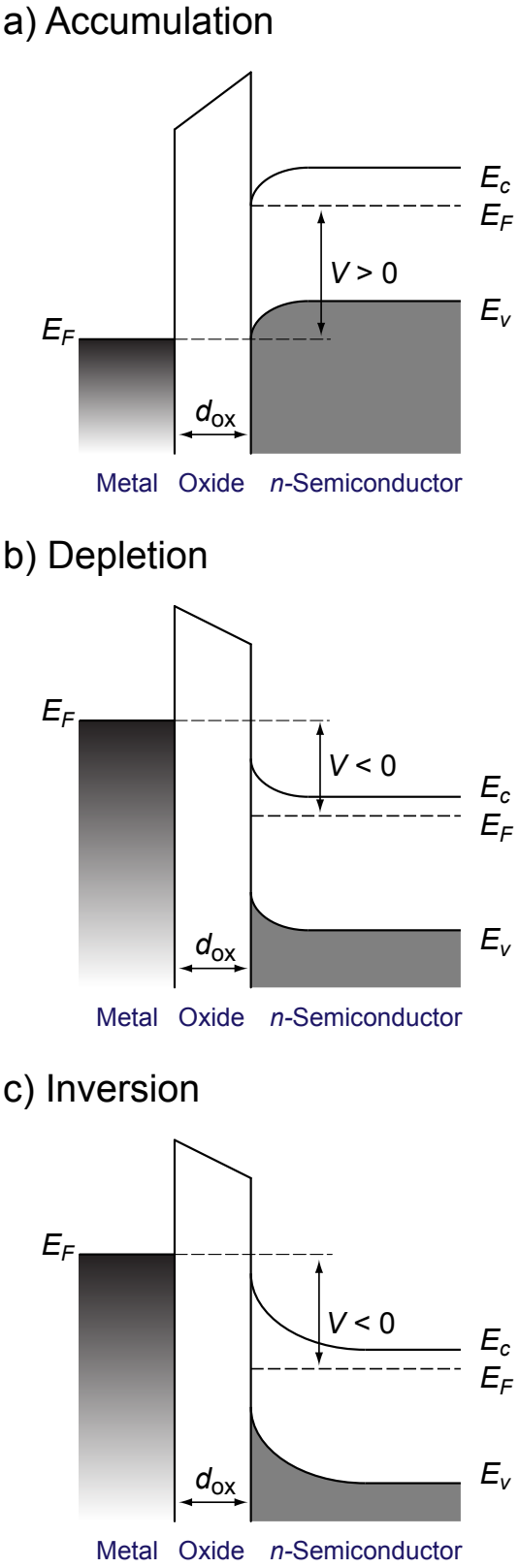

Figure 2.2: Energy-band diagram for an ideal MOS structure based on the n-type semiconductor under different voltage bias.

the metal work function and the semiconductor work function are equal in the ideal MOS structure. Structures satisfying the requirements for the ideal MOS structure do not exist. However, consideration of the ideal MOS structure is useful for the establishing a basis for the understanding of practical devices based of the MOS structures [46].

There are three cases, which can be distinguished when an ideal MOS structure is biased: a) accumulation, b) depletion, and c) inversion [46]. All the cases are shown in Figure 2.2 for the MOS structure based on the n-type semiconductor. The **accumulation** case can be observed in the MOS structure when a positive voltage bias ($V > 0$) is applied. The conduction band edge E_C bends downward in this situation, Figure 2.2a, and is positioned closer to the Fermi level. Since the charge carrier density depends exponentially on the energy difference ($E_C - E_F$) and no current flows through the ideal MOS structure, this leads to accumulation of majority carriers (electrons in this case) near the semiconductor surface. On the other hand, applying a negative voltage bias ($V < 0$) results in the **depletion** case, when the density of the majority carriers in the region near the semiconductor surface decreases, Figure 2.2b. Finally, when the negative voltage bias is so large, that the number of holes (minority carriers) at the semiconductor surface is larger than the number of electrons we have a case of **inversion**, Figure 2.2c.

2.2 Transport of charge carriers

As discussed in the previous section, in a MOS structure metal and semiconductor layers are separated by a thin insulating oxide film. By definition, an ideal insulating layer is not able to conduct any electric current under the influence of an electric field, because its charge carriers are not able to move freely. Thus, an ideal MOS structure should have an electric conductance equal to zero. However, real MOS structures are able to conduct electric current, when the electric field in the oxide film or temperature is high enough. Very often this happens with the involvement of electron traps, which in real oxides can be distributed with a fairly high density.

There are six basic conduction processes in oxide films, which are considered to explain their electric conduction: tunneling, thermionic emission, Pool-Frenkel emission, ohmic conduction, ionic conduction, and space-charge limited conduction. Further, we consider in more detail three of them (namely tunneling, thermionic emission and ohmic conduction) which are important for this work. Detailed descriptions of other conduction processes can be found elsewhere [46].

Tunneling is the most common conduction mechanism in the MOS structures based on very thin oxide films (as a rule, thickness is in the range $1 - 3$ nm). In tunneling transport of charges through the oxide film happens as a result of a quantum mechanical phenomenon, when the charge carriers can be represented by their wave functions. These wave functions can penetrate into and through the potential barrier even in the case,

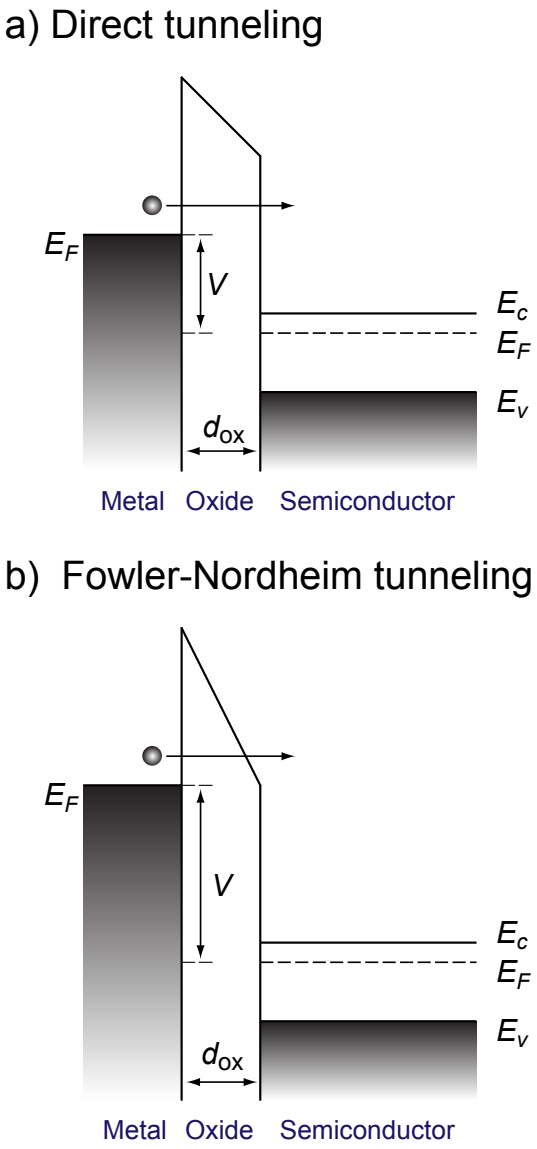

Figure 2.3: Energy-band diagrams showing a) direct tunneling and b) Fowler-Nordheim tunneling in MOS structures.

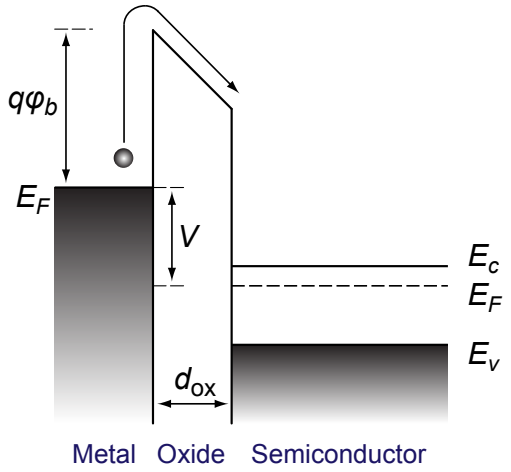

Figure 2.4: Energy-band diagram showing thermionic emission in MOS structures.

when the excess energy of the charge carriers is smaller that the barrier height. In general, tunneling in MOS structures can be divided into **direct** tunneling and **Fowler-Nordheim** tunneling. Both cases are shown in Figure 2.3. One can see, that in the case of direct tunneling charge carriers are transported through the whole width of the potential barrier, while for Fowler-Nordheim mechanism they tunnel through only a part of the width of the barrier [79]. The latter process occurs when an intense electric field is applied across the MOS structure, so that the potential barrier is tilted, see Figure 2.3b.

An essential feature of tunneling is that conductance of the MOS structure in the presence of this mechanism strongly depends on the electric field in the oxide film but is independent of the temperature. Charge carrier transport through the MOS structure for which tunneling is the dominant conduction mechanism can be expressed by [46]

$$I \propto \mathcal{E}_{\mathrm{ox}}^2 \exp\left[-\frac{4\sqrt{2m^*}\,(q\,\varphi_b)^{3/2}}{3\,q\,\hbar\,\mathcal{E}_{\mathrm{ox}}}\right], \tag{2.1}$$

where $\mathcal{E}_{\mathrm{ox}} = V/d_{\mathrm{ox}}$ is the electric field in oxide, V is the applied voltage bias, d_{ox} is the thickness of the oxide film, m^* is the effective mass, q is the elementary charge, φ_b is the potential barrier height, and $\hbar$ is the Planck constant.

Thermionic or Schottky emission in MOS structure is shown in Figure 2.4. In this case MOS conducts an electric current due to emission of electrons over the potential barrier into the semiconductor. In general, in MOS structures this process is similar to the thermionic emission in metal-semiconductor contacts. Therefore, charge carrier transport through the MOS structure can be described using an equation proposed by

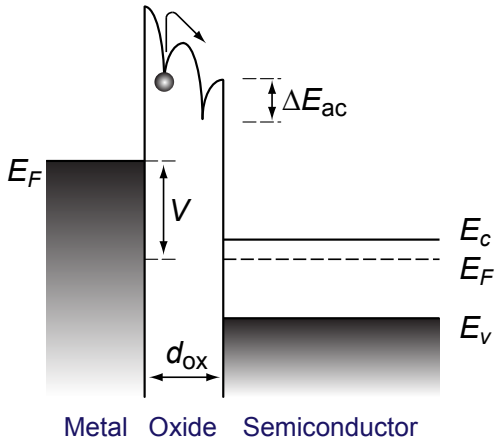

Figure 2.5: Energy-band diagram showing ohmic conduction in MOS structures.

Bethe [46]:

$$I \propto A^* T^2 \exp\left[-\frac{q\,\varphi_b - \sqrt{q\,\mathcal{E}_{\rm ox}/4\,\pi\,\epsilon_{\rm ox}}}{k_{\rm B}T}\right], \tag{2.2}$$

where A^* is the effective Richardson constant, T is the temperature, $\epsilon_{\rm ox}$ is the oxide permittivity, and $k_{\rm B}$ is the Boltzmann constant.

In Equation 2.2, the term subtracted from the potential barrier height (φ_b) is due to image-force lowering, which is observed in the Schottky barriers in the presence of an electric field.

Thermal excitation of electrons from traps into the conduction band can also contribute to the conductance of a MOS structure. At low voltages and high temperatures this mechanism results in the **ohmic** conduction, which can be described by the equation [46]:

$$I \propto \mathcal{E}_{\rm ox} \exp\left[-\frac{\Delta E_{\rm ac}}{k_{\rm B}T}\right], \tag{2.3}$$

where $\Delta E_{\rm ac}$ is the activation energy of electrons.

Chapter 3

Sample fabrication and characterization

This section describes methods of fabrication and characterization of the Pt/SiO_2-n-Si MOS nanostructures, which were used within this PhD work as detectors of electric charge carriers induced by surface chemical reactions. It starts with a step-by-step description of the fabrication sequence and is then followed by a review of the characterization of the MOS nanostructures using current-voltage curves. Finally, some notes related to the thermal stability of the fabricated Pt/SiO_2-n-Si MOS nanostructures are given.

3.1 Fabricaion sequence

A step-by-step sequence of the fabrication of a Pt/SiO_2-n-Si nanostructure is shown in Figure 3.1. At first, a commercial Si (111) substrate (n-type, 7.5 Ω·cm) $20 \times 10 \times 0.5$ mm^3 in size was etched with HF (6%) for 5 min, rinsed in Milli-Q water, and dried in a steam of high purity nitrogen. In the next step, a 100 nm silicon oxide layer was grown on the surface of the Si substrate by thermal oxidation in air at 1200 K for 1 hour. Further, a $d_{\mathrm{Pt}} = 9$ nm thick 0.9999 pure platinum film was deposited onto a top (polished) side of the substrate. The thickness of the Pt film was monitored during the deposition process using a quartz crystal microbalance. At the final step, a wide area low resistance contact was made at the back (unpolished) side of the Si substrate by thermal infusion of pure indium. The thickness of the indium contact (d_{In}) was estimated to be about 0.1 mm.

3.2 Current-voltage characteristics

In order to establish the conduction mechanism of the fabricated Pt/SiO_2-n-Si nanostructures, current-voltage ($I - V$) characteristics of them were studied at different temperatures were. For this purpose, a Pt/SiO_2-n-Si nanostructure placed in the high vacuum

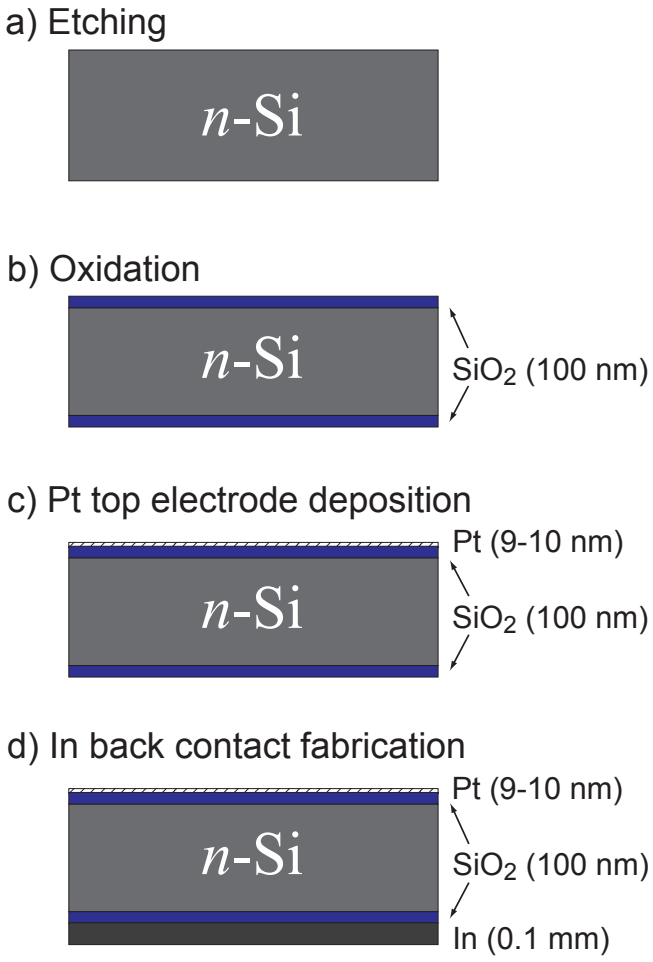

Figure 3.1: A Pt/SiO_2-*n*-Si nanostructure fabrication sequence.

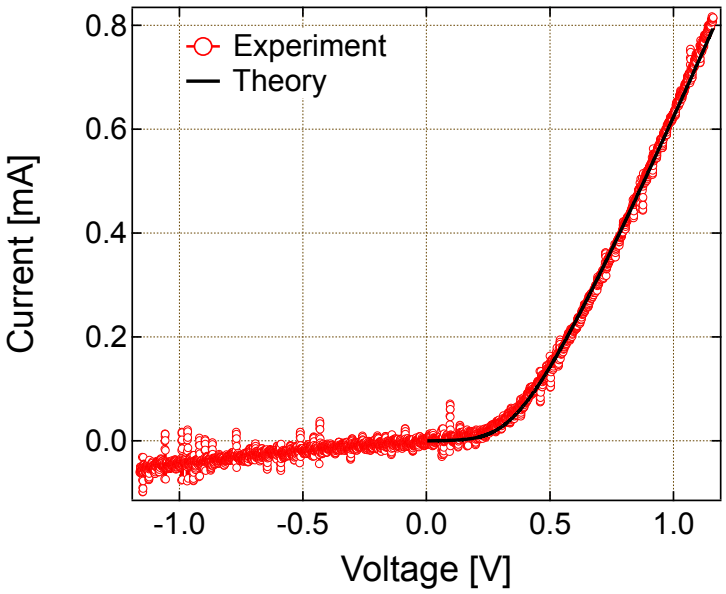

Figure 3.2: Current-voltage characteristics measured from the Pt/SiO_2-n-Si nanostructure at 296 K.

chamber, which will be described in Section 4.1, was connected to the HEKA PG 510 potentiostat, used as a voltage source.

A typical $I-V$ curve recorded from the Pt/SiO_2-n-Si nanostructure at a constant scan rate ($dU/dt = 20$ mV/s) for the voltage bias from -1.1 to $+1.1$ V is shown in Figure 3.2. The temperature was maintained at $T = 296$ K. As can be seen, the $I-V$ curve has a significantly asymmetric diode-like shape. The forward current (positive terminal of the voltage source is on Pt) can be described by the diode equation according to the thermionic emission theory [46]:

$$I = I_S \left[\exp\left(\frac{q(V_{\text{bias}} - IR_{\text{ser}})}{\eta k_{\text{B}} T} \right) - 1 \right], \tag{3.1}$$

where $I_S = AA^*T^2 \exp\left(-q\varphi_b/k_{\text{B}}T\right)$ is the saturation current, $A = 1.62$ cm^2 is the MOS junction area, $A^* = 120$ A·cm^{-2}·K^{-2} is the effective Richardson constant, φ_b is the barrier height, q is the electron charge, k_{B} is the Boltzmann constant, T is the temperature, R_{ser} is the series resistance, η is the ideality factor, and V_{bias} is the voltage bias. Fitting of the experimental $I-V$ curve for the Pt/SiO_2-n-Si structure by Equation 3.1 gives the following parameters: $\varphi_b = 0.86$ eV, $\eta = 2.16$, and $R_{\text{ser}} = 767\ \Omega$.

The use of MOS nanostructures to study surface chemical reactions may require heating of the surface of the nanostrucures to different temperatures. In addition to this, some heat can be generated by the chemical reactions themselves. Since all the key parameters, which are necessary to describe the conductance of MOS nanostructures, are temperature dependent, we have studied $I-V$ curves of our Pt/SiO_2-n-Si nanostructure at different

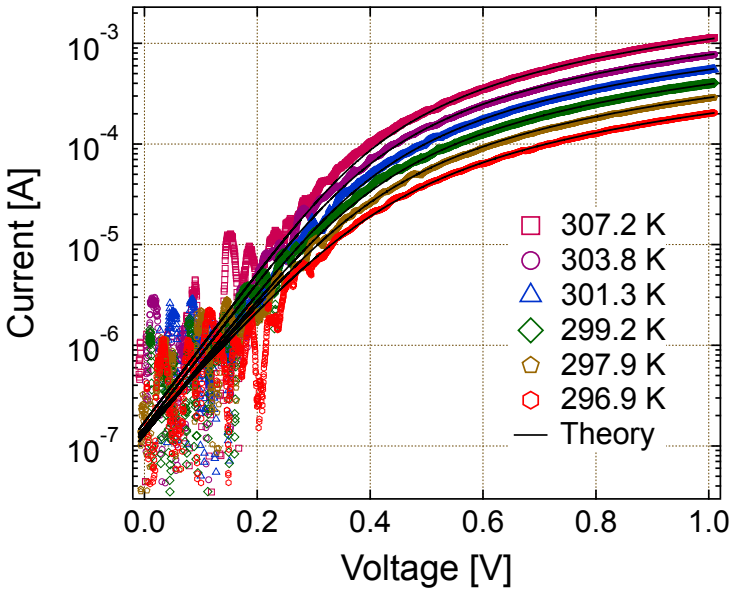

Figure 3.3: Current-voltage characteristics measured from the Pt/SiO_2-n-Si nanostructure at different temperatures in the range of 296 – 307 K.

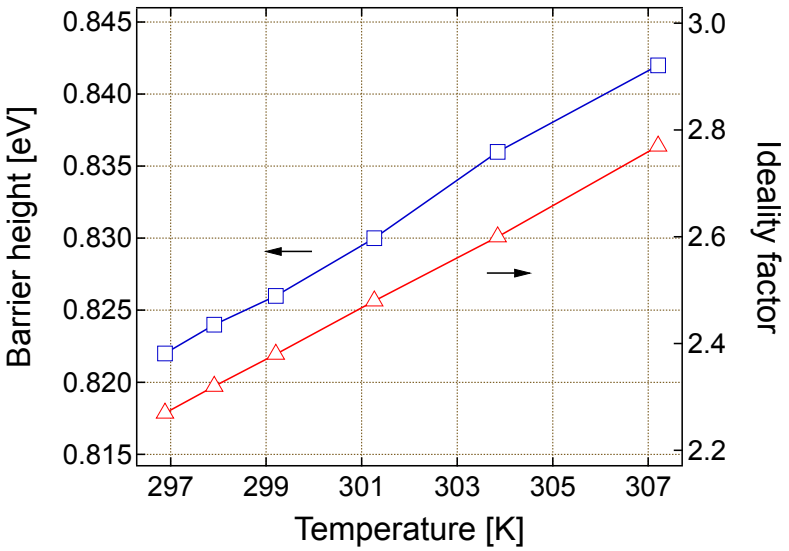

Figure 3.4: Temperature dependence of the barrier height and ideality factor for the Pt/SiO_2-n-Si nanostructure.

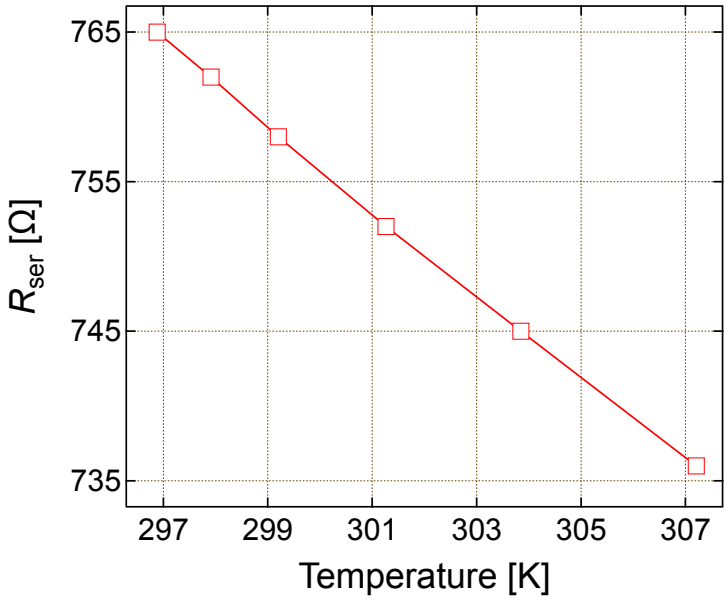

Figure 3.5: Temperature dependence of the series resistance for the Pt/SiO_2-n-Si nanostructure.

Table 3.1: Fitting parameters for the calculation of the current-voltage curves for the Pt/SiO_2-n-Si nanostructure at different temperatures.

Symbol	Physical parameter	a	b
φ_b	Barrier height	1.97×10^{-3} eV·K^{-1}	0.24 eV
η	Ideality factor	4.8×10^{-2} K^{-1}	-12.05
R_{ser}	Series resistance	-2.8 Ω·K^{-1}	1599 Ω

temperatures in the range of $296 - 307$ K. The forward current of these $I - V$ curves is shown in Figure 3.3. As can be seen, the current through the Pt/SiO_2-n-Si nanostructure has a tendency to rise with the increase of temperature. However, for all temperatures in the studied interval this current as a function of voltage bias can be well fitted by Equation 3.1. The temperature dependences of the barrier height and the ideality factor used for the fitting are shown in Figure 3.4. The series resistance as a function of temperature is shown in Figure 3.5. Once can see, that for the considered temperature range all three parameters show a linear dependence on the temperature, which can be represented in the form

$$y = aT + b, \tag{3.2}$$

where T is the temperature in K, a and b are constants listed in Table 3.1.

At first glance, the linear increase of the barrier height with the temperature, shown in Figure 3.4, may seem unusual. It is well known, that heating of a semiconductor leads to an increase of the concentration of electrons in the conduction energy band [46], which in turn should lead to some changes in the depletion layer at the MOS interface. These can

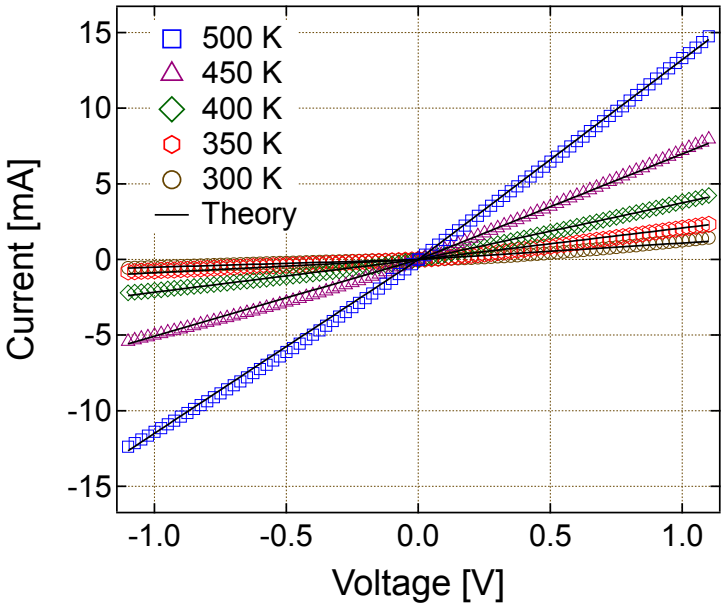

Figure 3.6: Current-voltage curves of the Pt/SiO_2-n-Si nanostructure after a series of experiments in which it was heated to temperatures in the range of $650 - 700$ K. Black solid lines show the fitting of the experimental $I - V$ curves by Equation 2.3.

be reducing the height of the potential barrier or decrease its thickness. According to the theoretical study made by Tersoff [80, 81, 82], the temperature dependence of the barrier height could be also a result of the variations of the band gap of the semiconductor. Thus, one would expect lowering of the potential barrier when the temperature of the MOS nanostructure is increasing. However, as shown in Reference [82], in real Schottky diodes based on silicon both the absolute value of the potential barrier height and its temperature coefficients depend on the interface structure and properties and not on the volumetric properties of the semiconductor. Therefore, one can expect some deviations from the theoretically predicted temperature dependence of the barrier height for the real nanostructures based on Schottky diodes.

3.3 Stability at high temperatures

As mentioned in the previous section, conductive properties of a Pt/SiO_2-n-Si nanostructure are temperature dependent. We have found, that as long as the temperature of the nanostructure does not exceed $T = 600 - 650$ K the change in the conductive properties is reversible. This means, that after experiments at elevated temperatures, cooling of the Pt/SiO_2-n-Si nanostructure to room temperature leads to complete recovery of the initial properties of the nanostructure.

However, heating of the Pt/SiO_2-n-Si nanostructure to temperatures higher than 600 K can cause some irreversible changes. This can be clearly seen in Figure 3.6. This

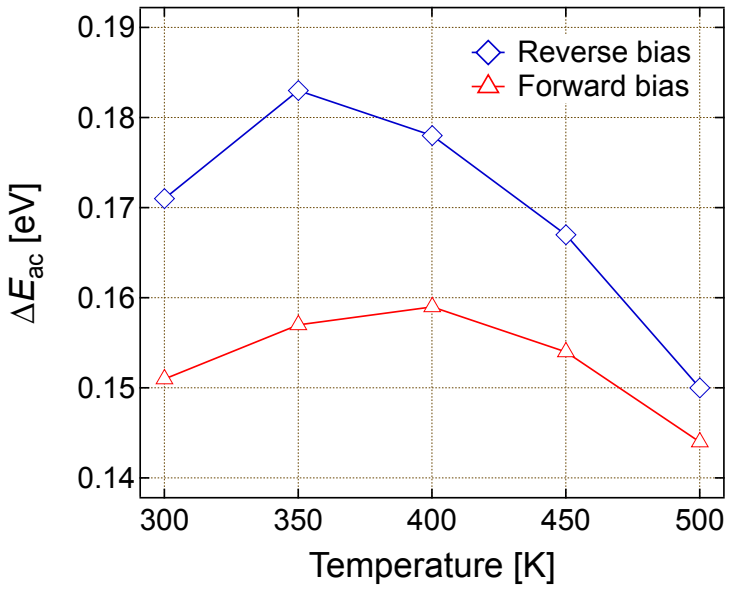

Figure 3.7: Temperature dependence of the activation energy calculated from the $I-V$ curves shown in Figure 3.6 using Equation 2.3.

figure shows $I-V$ curves recorded for different temperatures from the Pt/SiO_2-n-Si nanostructure after a series of experiments in which it was heated to temperatures in the range of $650-700$ K. In contrast to the initial $I-V$ curves (these curves are shown in Figure 3.2 and Figure 3.3) the $I-V$ curves recorded from the Pt/SiO_2-n-Si nanostructure heated to $T > 600$ K show a linear dependence of the current on the applied voltage for both forward and reverse biasing. As seen in Figure 3.6, this dependence can be well described by Equation 2.3 for all temperature values, which points to an ohmic type of conductance. Values of the activation energy, obtained from the fitting of the experimental $I-V$ curves by Equation 2.3 are shown in Figure 3.7. For both forward and reverse voltage bias, E_{ac} as a function of temperature is a curve with a maximum. For the forward voltage bias, the maximum of about 0.159 eV is observed at 400 K. In the case of the reverse biasing the maximum value of the activation energy is bigger, being about 0.183 eV and observed at 350 K.

In the frame of this PhD work we did not make a special study aimed at determining of the exact temperature limit for the Pt/SiO_2-n-Si nanostructure or the mechanisms responsible for the change of the conductance type from diode-like to ohmic. However, one can assume that high temperatures promote diffusion of metal atoms from the top and back electrodes of the nanostructure into the oxide films, which is a well known phenomenon (see for example Reference [83]). The presence of the metal atoms in the oxide film can provide new pathways for the charge transport through the oxide, which in turn may cause degradation of the potential barriers at metal-oxide interfaces. This assumption matches well to the conclusion drawn by Tsui and Chen, who studied dielectric

degradation of $Pt/SiO_2/Si$ structures during thermal annealing [84]. The authors considered three possible degradation mechanisms (namely, (1) chemical reaction between Pt and SiO_2, (2) thermal stress, and (3) Pt dissolution in SiO_2) and came to a conclusion, that only the third mechanism could be the reason of the degradation of the $Pt/SiO_2/Si$ structures during thermal annealing.

It is also interesting to note, that values of the activation energy shown in Figure 3.7 are close to the depth of traps caused by the presence of indium [85] and platinum [86] in silicon.

Chapter 4

Experimental setup

In this chapter an overview of the equipment, experimental methods and conditions used to carry out experimental part of this PhD work is given. At first, the high vacuum system in which most of our measurements have been done is described. Further, some of experimental methods (namely, direct heating and thermometry, and temperature programmed desorption), which were developed in the frame of this work for the use of composite nanostructures in the surface science are presented.

4.1 High vacuum system

All measurements were carried out in a custom high vacuum (HV) system with a base pressure of 2×10^{-4} Pa shown in Figure 4.1 and Figure 4.2. This system consists of a stainless steel chamber (reactor), which can be closed by a glass dome. The overall volume of the chamber with the dome is $V_{\text{reactor}} = 1.2 \times 10^{-1}$ m^3. The chamber is equipped with the capacitive transmitter EDWARDS 600AB (pressure range 10^3 Pa), the vacuum gauge LEYBOLD ITR 090 (pressure range 5×10^{-8} Pa), the system of gas inlet with balloons of three different gases (oxygen, hydrogen, and argon), the volume for gas mixing and the leak valve, and the pumping system, which consists of the turbo molecular pump Varian Turbo-V 250 connected to the pre-vacuum line.

The sample holder with a sample was placed in the middle of the chamber and connected to the measuring circuit using a 9-pin electric connector, Figure 4.3. The outlet of the gas inlet system was located in front of the sample surface at a distance of 20 cm.

Figure 4.4 shows a schematic view of the sample holder with a sample (Pt/SiO_2-Si nanostructure). The sample holder consisted of a copper plate $50 \times 40 \times 1.0$ mm^3 in size, equipped with 8 electric contacts insulated from the plate by ceramic cups. At a distance of 2 cm from the surface of the copper plate, a thin film heater was located. The heater consisted of a $20 \times 10 \times 0.5$ mm^3 in size $SiO_2/Si/SiO_2$ substrate with a thin Au film, deposited on the side opposite to the one where the sample was fixed. This Au film of the heater was connected to the electric contacts on the copper plate using two copper

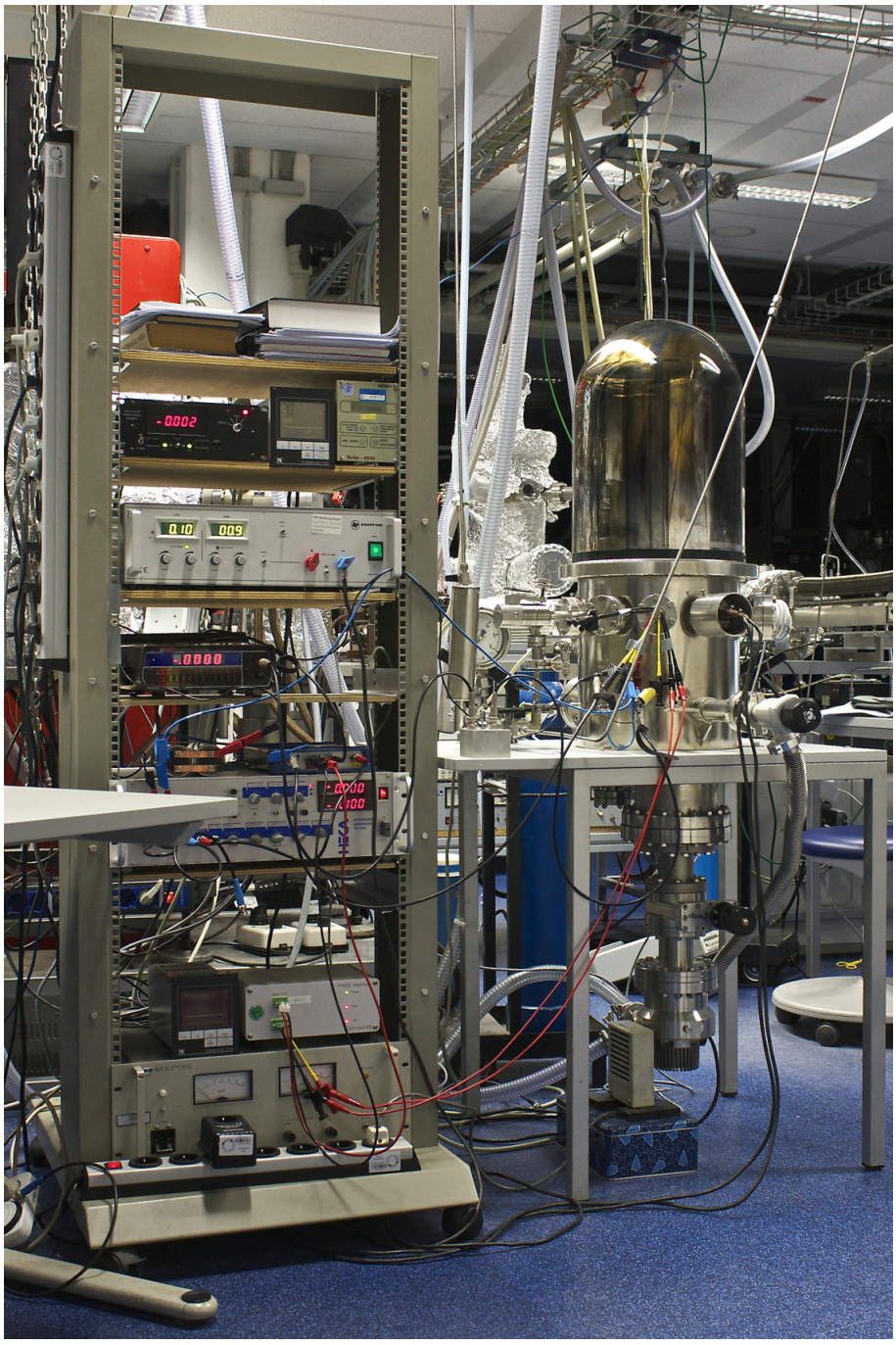

Figure 4.1: High vacuum system for the chemicurrent study of energy dissipation processes.

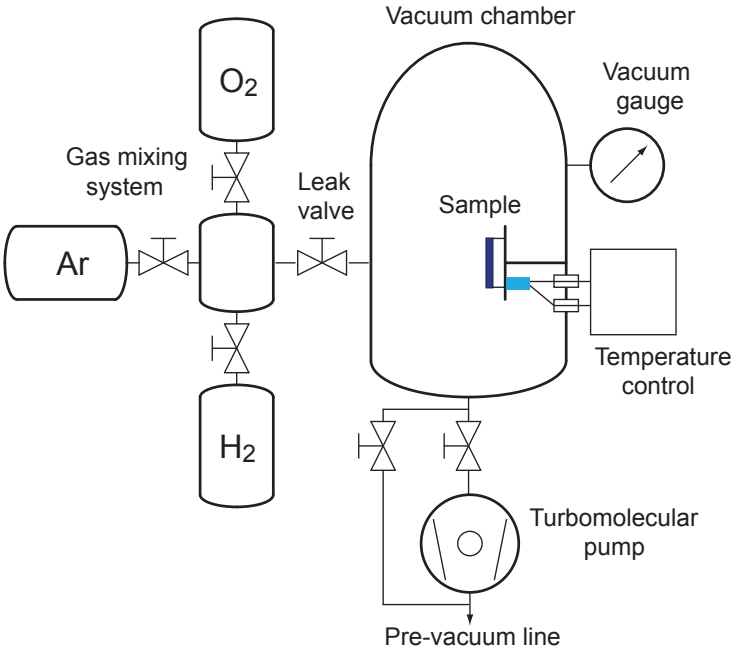

Figure 4.2: Scheme of the chemical reactor system for the chemicurrent study of energy dissipation processes.

strips, which served simultaneously for conducting electricity and supporting the heater with the sample.

A Pt/SiO_2-Si nanostructure (sample) was fixed on the surface of the thin film heater using conductive silver paste. To measure the temperature, a Pt1000 RTD sensor, $2.3 \times 2.1 \times 0.9$ mm^3 in size, was mounted in the middle of the thin film heater, see Figure 4.4. If necessary, one more RTD sensor of the same type was fixed directly on the top electrode of the Pt/SiO_2-Si nanostructure.

4.2 Methods of direct heating and temperature measurement

As already discussed in Section 1.1, chemical reactions on metal surfaces can lead to the excitation of electron-hole pairs. These charge carriers can be detected as a chemicurrent with the use of detectors based on the metal-semiconductor (MS) [2, 5, 6, 7, 8, 9], metal-oxide-semiconductor (MOS) [10] or metal-insulator-metal (MIM) [11, 12] composite nanostructures.

As shown in References [8, 13, 16, 17] a thermocurrent can arise in the detectors mentioned above along with the chemicurrent due to spurious heating of the top metal

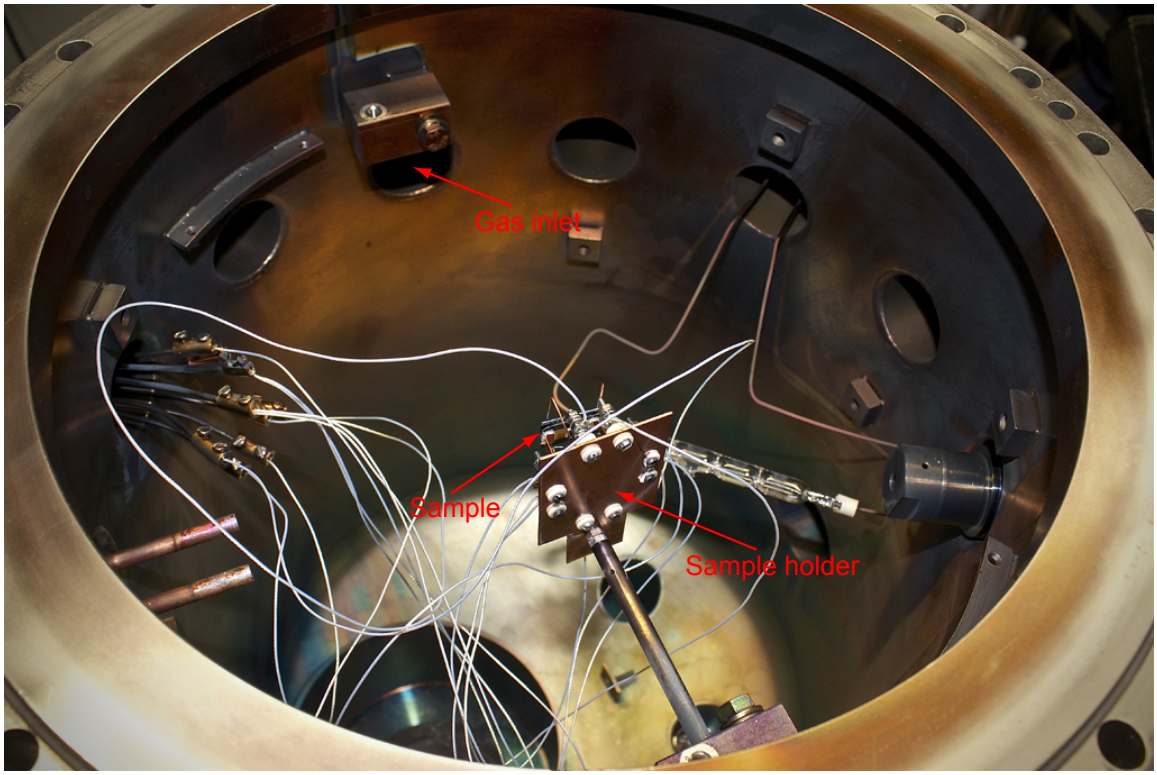

Figure 4.3: Position the sample in the high vacuum chamber. The outlet of the gas inlet system was located in front of the sample surface at a distance of 20 cm.

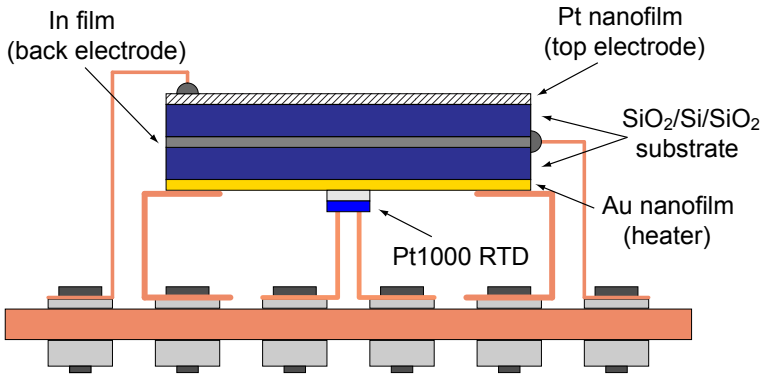

Figure 4.4: Schematic view of the sample holder with a sample. A Pt/SiO_2-Si nanostructure (sample) is placed on the surface of the heater, which consist of Au nanofilm deposited on a $SiO_2/Si/SiO_2$ substrate of the same size as the sample. Electric contacts to the heater are simultaneously used to support the sample.

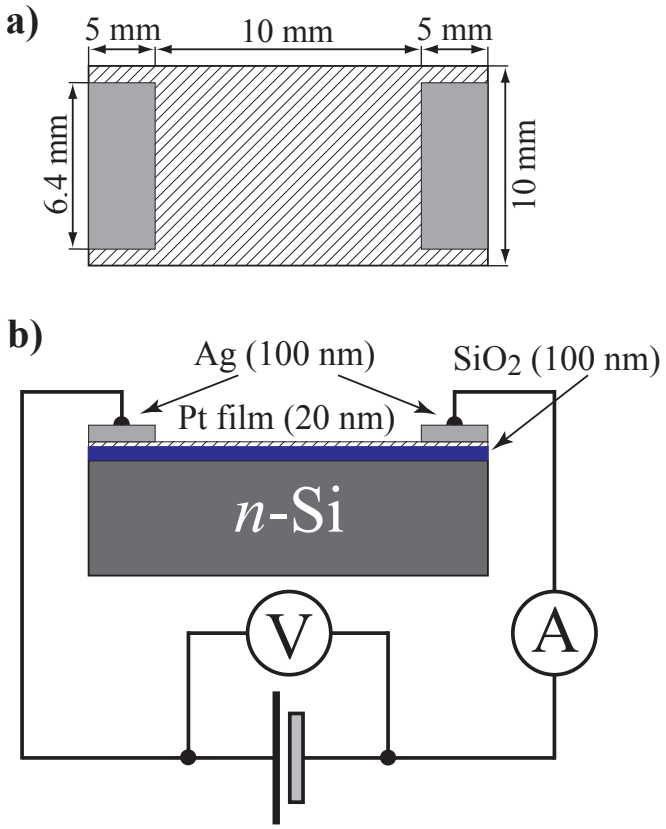

Figure 4.5: a) Top view and b) cross-sectional schematics of the Pt/SiO_2-Si nanostructure and the electrical circuit used for the direct resistive heating and temperature measurement studies.

electrode by the chemical energy released at the surface. Thermal effects hamper the experimental, unambiguous identification of chemicurrents unless a reliable and accurate monitoring of the temperature of the top metal electrode is established. Traditional approaches using an RTD or thermocouple sensor attached to the surface are inadequate for nanometer thickness films due to the large heat capacity of the sensor when compared to that of the film.

Therefore, here we discuss an alternative non-invasive technique to accurately measure and control the temperature of the Pt/Si and Pt/SiO_2-n-Si nanostructures over a wide range, where the material of the top metal electrode itself serves as a resistive temperature sensor. We also compare the accuracies of the traditional RTD and the presented method. Figure 4.5 shows a cross-sectional view and an electric circuit of a Pt/SiO_2-Si nanostructure used for the study of non-invasive techniques of heating and temperature measurement.

The temperature dependences of the Pt film resistance for the Pt/Si and Pt/SiO_2-n-Si nanostructures is depicted in Figure 4.6. For comparison, the temperature dependence of a 20 nm Pt film deposited on a flat glass slide (72.2 % of SiO_2) is presented in the same

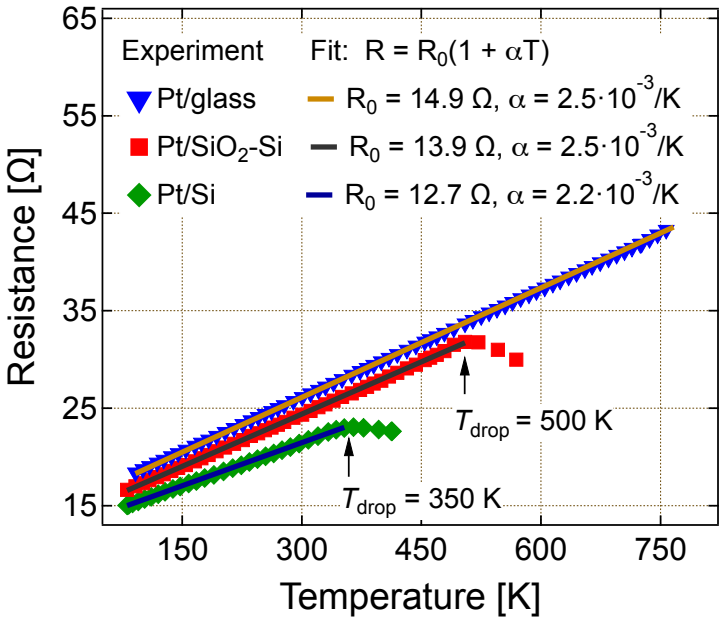

Figure 4.6: Resistance of a 2 cm×1 cm×20 nm Pt film deposited on glass, Si and SiO_2-Si substrates as a function of temperature measured by the Pt 1000 sensor on the top of the Pt surface. Using the linear fit the resistance can be converted to a temperature.

plot. As seen, below 300 K both, the Pt/Si and the Pt/SiO_2-n-Si nanostructure, show a linear temperature dependence of the Pt film resistance, similar to the one of the Pt-glass sample. At higher temperatures a strong deviation from the linear behavior is observed as the resistance drops after reaching some temperature, T_{drop}. This effect can be explained by a growing contribution from a current through the semiconducting substrate, to which an increasing conductance across the Pt-substrate interface may give rise. The value of the Pt film resistance can be reversibly monitored as a function of temperature for each of the samples and does not change due to repeated heating. This means, that the appearance of T_{drop} is not caused by an irreversible change of the Pt/substrate interface. Instead, the value of T_{drop} markedly depends on the interface conditions, So, for example, it is 350 K for Pt/Si and 500 K for Pt/SiO_2-n-Si structures. It is worth noting, that the presence of silicide, which forms at the Pt/Si interface after annealing at 250°C [87], or defects in SiO_2 would increase the leakage currents through the silicon substrate and significantly affect the value of T_{drop}. For the Pt/glass structure a linear temperature dependence of Pt film resistance is observed up to 730 K, the temperature at which the sample is destroyed due to a softening of the glass substrate. Thus, T_{drop} cannot be determined for this structure.

Once a relationship between the resistance of the Pt film and its temperature is established, the film itself can be used as a sensor of its own temperature. For this purpose, the linear fit of the dependence $R(T)$ at $T < T_{\text{drop}}$ can be inverted to determine the temperature $T = T(R)$. To such an approach will further on be referred as to the **direct thermometry** of the nano film. In contrast to traditional methods using a standard RTD

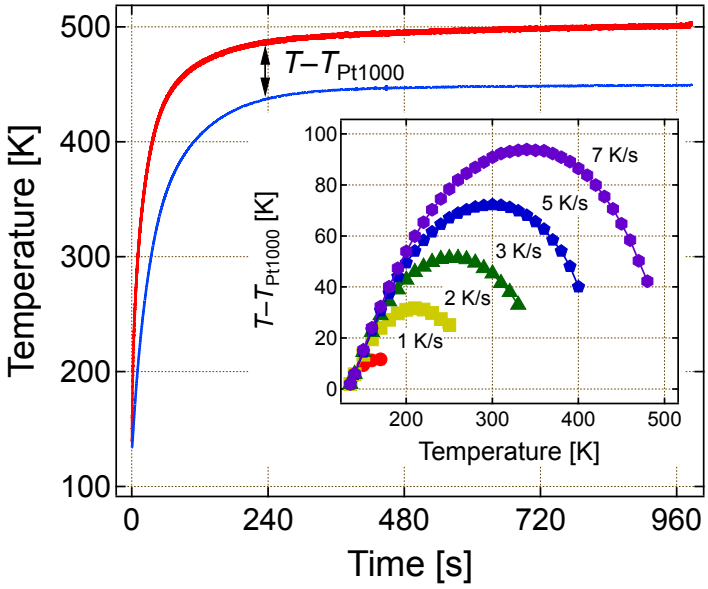

Figure 4.7: The temperature of a 20 nm Pt film on a SiO_2-Si substrate measured simultaneously using the direct thermometry (red curve) and the Pt1000 RTD sensor attached to the film surface (blue curve) during a heating ramp with a rate of 7 K/s. Inset: Difference between the temperatures of the Pt nanofilm measured directly and using a Pt1000 sensor as a function of the film temperature for various heating rates.

or thermocouple sensor attached to the surface, the direct thermometry eliminates spurious influence of the sensor itself on the measurement process. This influence is associated with the following factors: (a) large response time due to the much larger heat capacity of the sensor compared to that of the nanostructure, (b) uneven temperature distribution in the contact area between sensor and a surface of interest, and (c) issues of heat transfer between the surface and the sensor. The results discussed below demonstrate that these factors can be particularly important in the case of large heating/cooling rates, such as those accompanying non-steady state situations in surface chemistry.

The temperature of a 20 nm Pt film of a SiO_2-Si substrate was monitored simultaneously using direct thermometry and a Pt1000 RTD sensor attached to the middle of the film during its heating with various rates in the range of $1 - 7$ K/s with the first measurement controlling the heating rate. Next, the difference $T - T_{\mathrm{Pt1000}}$ between the temperature of Pt film measured directly and with the Pt1000 RTD sensor was derived (Figure 4.7). The inset in Figure 4.7 shows $T - T_{\mathrm{Pt1000}}$ as a function of temperature for different heating rates. As can be seen, $T - T_{\mathrm{Pt1000}}$ strongly depends on the heating rate: it increases with the heating rate and can reach 95 K, corresponding to a 28% deviation, when the Pt film is heated from 135 K to 500 K at the rate of 7 K/s.

Passing a significant DC current through the nanofilm enables resistive Joule heating which is however not conflicting with the ability to measure the temperature as the

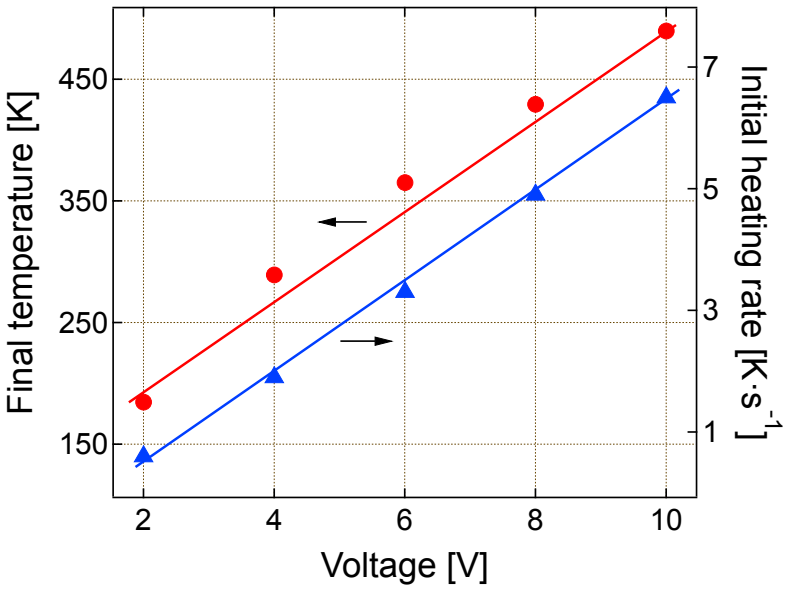

Figure 4.8: Final temperature and initial heating rate for a 20 nm Pt film on a SiO_2-Si substrate as function of the voltage applied for heating.

resistance is easily monitored. This provides a versatile method of temperature control using an $R(T)$ dependence established earlier, such as the one shown in Figure 4.6. This could be of particular interest for application in surface science studies employing methods such as temperature programmed desorption. Very clean experimental conditions can be achieved, since the direct heating deposits electrical power predominantly in the Pt layer of the MS/MOS nanostructure as long as $T < T_{\mathrm{drop}}$ [88]. Among other problems, outgassing from a sample holder and other external parts is avoided.

We have observed that the $R(T)$ dependence established once is stable for many experiments to follow, and may easily be reconfirmed at any time. Moreover, we find that the initial heating rate is linearly dependent on the voltage applied to the Pt film. The dependence of the final, steady-state temperature of the film is also close to be linear. This allows easy control of the final temperature by adjusting the current passing through the Pt nanofilm. Figure 4.8 shows the final temperature and the initial heating rate, when the Pt film on a SiO_2-Si substrate, fixed to the copper sample-holder 45×15×4 mm^3 in size, is resistively heated in a vacuum, using various voltages. Figure 4.9 shows the electric power dissipated in the Pt nanofilm as function of the voltage applied for heating. However, it is worth noting that the necessary voltage values will markedly depend on the size and properties of the Pt film used in different laboratories.

The recorded dependence of the final temperature T_{final} on the voltage, which is shown (Figure 4.8), can be fitted with a line $T_{\mathrm{final}} = T_0 + kU$ where T_0 is the initial temperature and k is the slope. This linear dependence is at first surprising, since one would expect the final temperature to be linearly dependent on the electric power P dissipated in the Pt

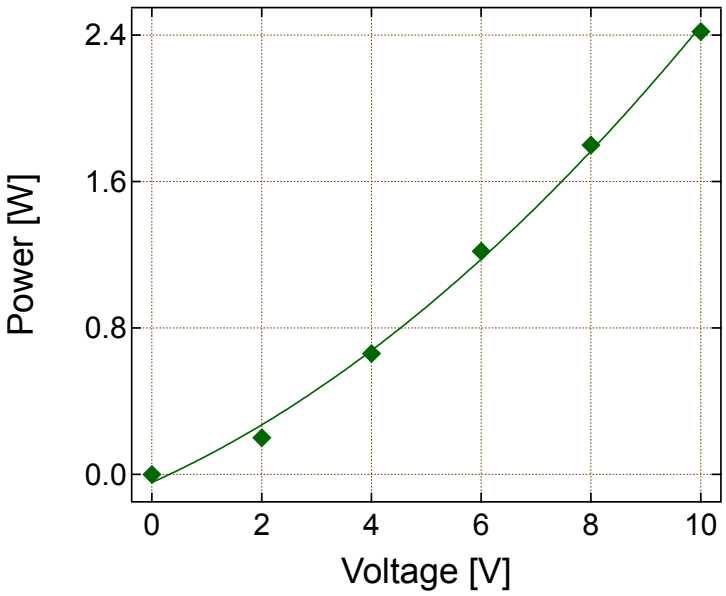

Figure 4.9: The electric power dissipated in the Pt nano film as function of the voltage applied for heating.

nanofilm, but not on the voltage. However, this behavior can be understood if one takes into account that the resistance of the Pt nanofilm is not constant. Rather it significantly changes during the heating process, see Figure 4.6. As a result, T_{final} as a function of the dissipated electric power may deviate from the expected U^2 dependence. Taking into account $R(T)$ we obtain:

$$P = \frac{U^2}{R} = \frac{U^2}{R_0(1 + \alpha\, T_{\text{final}})} \tag{4.1}$$

which suggests a weaker dependence than U^2 (see Figure 4.9.) For the conditions of this experiment we find that P scales nearly linear with U for $U > 2V$, which explains the observed scaling of T_{final} with U.

According to our observations, upon reaching T_{drop}, when the resistance rapidly drops, the dissipated electric power rapidly increases (not shown in Figure 4.8) resulting in permanent device damage provided that the electric current through the device is not limited instrumentally.

It should be also noted that even a small DC current, such as used for the direct thermometry, will also heat the Pt nanofilm. It is possible to estimate the size of this effect of self-heating using the experimental data presented in Figure 4.8. Indeed, the linear fit of the final temperature as a function of the applied voltage gives us $\Delta T/U = 39.3$ K/V, where ΔT is the change in temperature due to internally dissipated electric power when the voltage U is applied. For a bias voltage of 100 mV (which corresponds to about 4 mA current flowing through the Pt nanofilm at 300 K), as used in this study to perform the temperature measurement, the change of the temperature due to the effect of self-heating

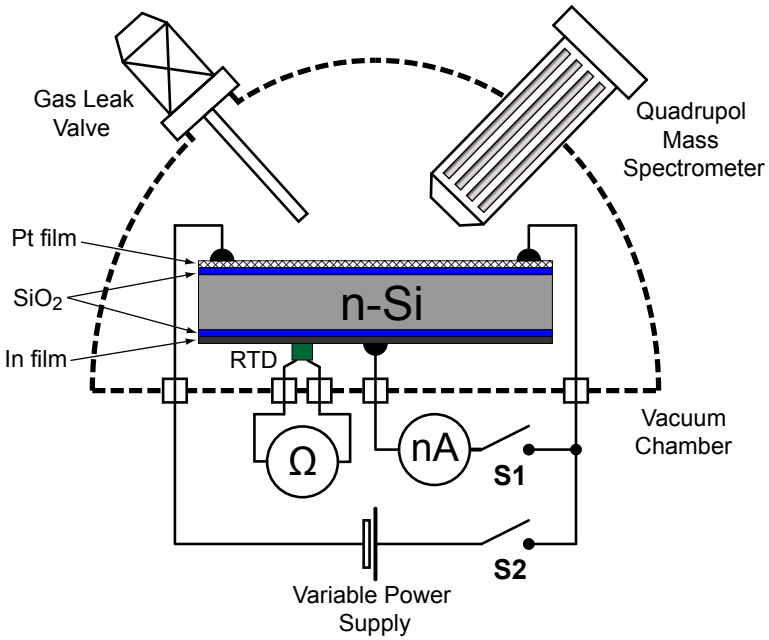

Figure 4.10: Schematic of the experimental setup, which combines direct heating and temperature measurement using Pt/SiO_2-n-Si nanostructures with the TPD technique. The temperature of the device is monitored by a Pt1000 RTD sensor.

$\Delta T = 3.93$ K. Moreover, the current can be reduced to a value less than 1 mA, which will result in $\Delta T < 1$ K. This change of the temperature due to the self-heating effect will be tolerable in most experimental situations.

4.3 Thermal desorption spectroscopy

As shown in Section 1.2 metal-semiconductor, metal-oxide-semiconductor, and metal-oxide-metal composite nanostructures allow the direct detection and quantification of electronic excitations created in the top metal nanofilm in the course of catalytic chemical reactions, as, e.g., the recombination of atomic hydrogen [5, 11, 12] or the oxidation of carbon monoxide [39, 6] and hydrogen [7, 14, 13]. Comparison of the amount of detected hot charge carriers to the number of chemical events on the surface of the composite nanostructures can in principle provide an answer to the long-standing question regarding the role of transient electronic excitations of the substrate in the pathways of energy dissipation [2, 3, 89]: a question, the answer to which is fundamental for the development of a predictive theory of surface chemistry on a molecular level.

Thermal desorption spectroscopy (TDS) is a versatile and prolific tool for studying the kinetics of desorption processes from surfaces, also including the associative reactions which are the final step in catalysis [90, 91, 92]. Moreover, as a method of spectrometry it also allows to gain insights into the composition of the adsorbate layer. And, the spectra

provide some information about the structure of the substrate surface. However, the complex structure and the larger size of the composite nanostructures typically hampers the use of TDS. Moreover, one would really like to be able to record a spectrum while monitoring the flux of hot carriers at the same time.

As a rule, the top electrode of the composite nanostructures consists of a polycrystalline, nanoscopic film of a metal (in most cases it is silver, platinum or palladium) and acts both as a catalyst for a chemical reaction, and a terminal for the electric circuit, which allows to measure the current of hot charge carriers created by the chemical reaction. Both physical and chemical properties of the top metal electrode may vary significantly from one type of composite nanostructure to another due to different methods of preparation, to properties of the support, and the geometry of the electrode etc. Therefore, there is a need to combine the composite nanostrucutres with the standard techniques of surface science, which enables an *in situ* characterization of their properties and the state of their surface as well as monitoring the rate of a surface chemical reaction simultaneously with the detection of hot charge carriers.

In this chapter, we discuss ways which allow to use TDS despite the complexity of the devices. We report that temperature programmed desorption (TPD) experiments become feasible by combining direct, resistive heating of the metal film with the temperature measurement [59] in a way which does not hinder the detection of electronic excitations. We demonstrate this combination of methods by studying the thermal desorption of water molecules from the surface of a Pt/SiO_2-*n*-Si nanostructure.

All measurements described in this chapter were carried out using a custom UHV chamber with a base pressure better than 5×10^{-10} mbar. A cross-sectional view of the UHV chamber with the Pt/SiO_2-*n*-Si nanostructure is depicted in Figure 4.10. Two silver contact pads were located at opposite ends of the Pt nanofilm allowing us to pass a current through it. The two silver contact pads were connected to a variable power supply. In the first step, the temperature dependence of the resistance of the Pt nanofilm was calibrated. A constant voltage of 100 mV was applied through the switch S_2, see Figure 4.10, and the nanofilm resistance was measured over the temperature range from 60 to 300 K. For this purpose, the Pt/SiO_2-*n*-Si nanostructure was cooled at a very small rate of about 0.01 K/s, making use of the connection to the helium coldfinger, starting from room temperature. It was found, that the resistance of the Pt nanofilm can be well described by a linear dependence $R_{\mathrm{Pt}} = R_0 + \alpha T$ on the temperature T, where $R_0 = 6.96\ \Omega$ and $\alpha = 0.039\ \Omega/\mathrm{K}$ are constants.

Establishing the temperature dependence of the resistance of the platinum nanofilm allowed us to use further on the latter as a temperature sensor and a heater. To record thermal desorption spectra, the device was cooled to $T_0 = 80$ K and exposed to H_2O. In the next step, the switch S_2 was closed and the Pt nanofilm was resistively heated by an electric current controlled by the power supply. The heating power was varied by

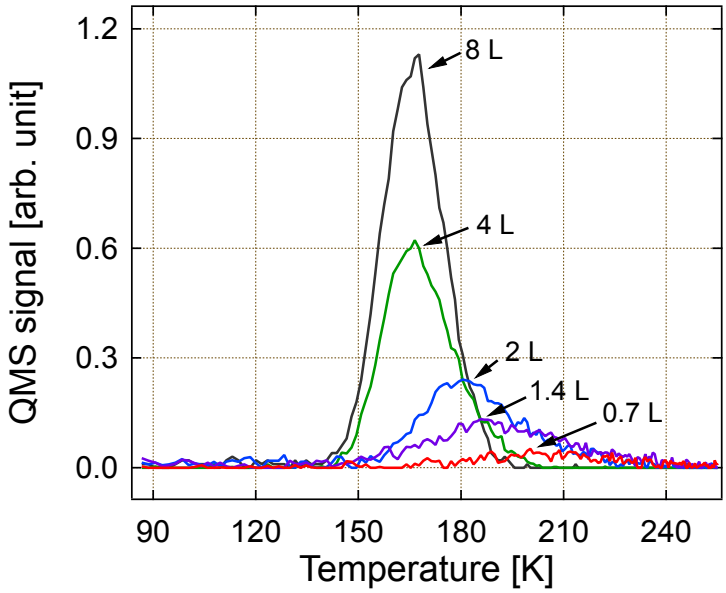

Figure 4.11: TD spectra of H_2O from a Pt/SiO_2-n-Si nanostructure for different exposures in the range of 0.7 to 8.0 L. The heating rate is 11 K/s.

changing the voltage in the range of $0 - 10$ V, which allowed us to dissipate a power of up to 9 W for which the heating rate reached 100 K/s. Simultaneously with the direct heating, the temperature reading was obtained by monitoring the current and using the inverted temperature dependence of the Pt nanofilm resistance

$$T = \frac{U/I - R_0}{\alpha}. \tag{4.2}$$

Following reference [59] this method will be called direct heating and temperature measurement.

A quadrupole mass spectrometer (QMS) (MKS, Spectra Satellite LM 61) was used for residual gas analysis and monitoring the desorption flux. For simplicity we made use of the H_2O content in the background to carry out this study. Doses are given in units of L (1 L = 10^{-6} Torr·s) for which we derived the H_2O partial pressure from reading the pressure meter, which may overestimate the actual value.

Finally, an ammeter connected to the top and back electrodes of the Pt/SiO_2-n-Si nanostructure through the switch S_1 was used to measure the device current induced by a surface chemical reaction or an applied voltage bias, if a voltage source (not shown in Figure 4.10) is connected in series to the ammeter. The current-voltage characteristics recorded from the Pt/SiO_2-n-Si nanostructure before and after TPD experiments were identical. Thus, we conclude, that the electronic properties of the nanostructure are not altered by heating of the top electrode to the extent necessary for H_2O TDS.

Typical thermal desorption spectra of H_2O from the polycrystalline surface of the

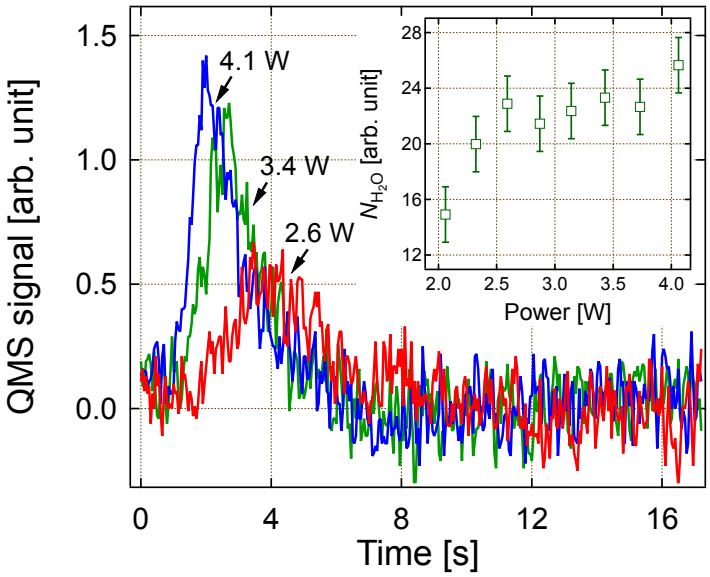

Figure 4.12: TD spectra from the Pt/SiO_2-n-Si nanostructure exposed to 0.7 L of H_2O for several values of heating power. The heating rates were 100, 67, and 50 K/s. Inset: Amount of desorbed H_2O (area under the QMS signal curves) as a function of the heating power. The solid line depicts the calculated amount of desorbed H_2O by the model presented.

Pt/SiO_2-n-Si nanostructure are depicted in Figure 4.11 for different values of exposure in the range of $0.7 - 8.0$ L. These curves are observed, when the Pt nanofilm is resistively heated from 80 to 250 K in which case the heating rate reached 11 K/s. The heating is not constant in our experiments as we apply a constant power. However, it could easily be made so by adding a temperature controller. On the other hand, in view of the device current measurements intended it may be advantageous to work with a constant voltage and to accept the non-constant rate.

For exposures smaller than 1 L, the TD spectrum consists of a single broad peak with a maximum at about 200 K. With increasing exposure this peak narrows and shifts toward lower temperatures. So, for instance, for the largest exposure used in our experiments (8.0 L) the maximum is observed at 170 K. These results are similar to previously published TD spectra for H_2O from different faces of Pt [93, 94, 95] with respect to the position of the maximum and its shift with coverage.

The areas under the curves shown in Figure 4.11 are proportional to the number of H_2O molecules desorbed, as they are plotted versus time. Thus, the amount of desorbed H_2O can be found by integration of the QMS signal over the time

$$N_{\mathrm{H_2O}} = K_1 \int_0^t I(t)dt, \tag{4.3}$$

where K_1 is a constant.

The full application of the TPD technique may require heating with different rates.[90] In our approach this can be achieved by varying the electric power dissipated in the Pt nanofilm, i.e. by applying different voltages or electric currents. However, the measured value for N_{H_2O} is expected not to depend on the heating power dissipated in the Pt nanofilm as long as the pumping speed of the UHV system is sufficiently large. Thus, one would expect, that the area under the thermal desorption curves should be independent of the heating power used as long as the amount of adsorbed H_2O is kept constant. However, we experimentally observe that the area is increasing with increasing electric power (Figure 4.12).

This effect may be understood when taking into account the temperature profile in the Pt nanofilm, when the latter is heated. The problem is that the leads at the ends of the Pt nanofilm are such large in heat capacity that they will effectively hold the film at the idle temperature T_0 at the contact points. In order to quantitatively model this situation, we divide the film into finite volume elements $dV = (h_{Pt} + h_{Si})w dx \approx h_{Si} w\, dx$, where h_{Pt} is the thickness of the Pt film, h_{Si} the one of the SiO_2/Si/SiO_2 substrate, w the width, and dx the length of the differential volume element (see Figure 4.13) For simplicity, we will use the values for bulk Si for the properties of the SiO_2/Si/SiO_2 substrate. At steady state ($dT/dt = 0$) the one-dimensional heat conduction along the x-axis is accounted for by [96]

$$\frac{d}{dx}\left(\frac{dT(x)}{dx}\right) + \frac{1}{\kappa}\left(q_{\text{Joule}} + q_{\text{rad}} - q_{\text{cooling}}\right) = 0, \tag{4.4}$$

where $\kappa = \kappa_{Pt} + \kappa_{Si}$ is the thermal conductivity of the differential volume element, with κ_{Pt} the thermal conductivity of Pt nanofilm and κ_{Si} the thermal conductivity of Si substrate, q_{Joule} the power density ($W \cdot cm^{-3}$) of the Joule heating in the Pt nanofilm, q_{rad} the power density of heating due to radiative exchange between the Pt nanofilm and walls of the vacuum chamber, and q_{cooling} the power density of the cooling caused by conduction to the helium coldfinger. Note, that Equation 4.4 implies that the heat is generated in the Pt nanofilm only, but transported through the whole Pt/SiO_2-n-Si nanostructure.

The Joule heating caused by a constant electric current flowing through the Pt nanofilm can be described as

$$q_{\text{Joule}} = \frac{dQ_{\text{Joule}}}{dV} = \frac{d}{dV}\left(I^2 R\right) = \frac{I^2 \rho_e}{h_{Pt} h_{Si} w^2}, \tag{4.5}$$

where I is the current and $R = \rho_e dx / h_{Pt} w$ the electric resistance of the Pt nanofilm whose resistivity is ρ_e. The radiative heat exchange between the Pt nanofilm and the walls of the vacuum chamber is described by the Stefan-Boltzmann law

$$q_{\text{rad}} = \frac{dQ_{\text{rad}}}{dV} = \frac{1}{h_{Si}} \varepsilon \sigma_B (T_{\text{wall}}^4 - T(x)^4), \tag{4.6}$$

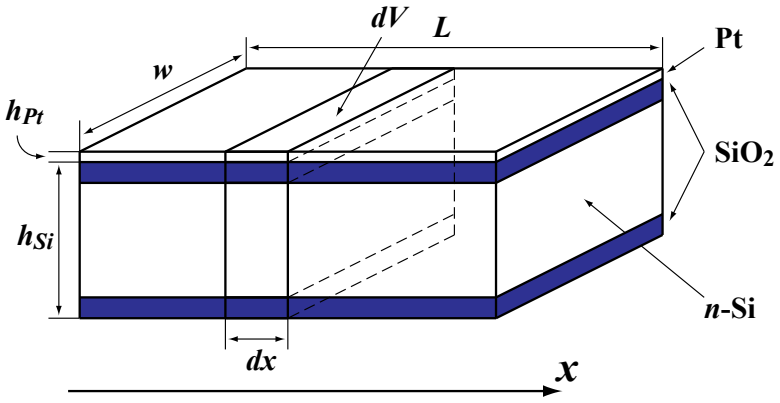

Figure 4.13: Illustration of the differential volume element considered in the one-dimensional heat conduction model.

where ε is the emissivity of the Pt nanofilm, σ_B the Stefan-Boltzmann constant, and T_{wall} the temperature of the chamber walls.

Prior to heating the device, the cooling caused by the connection though the device holder and the probe wires to the coldfinger is balanced by radiative heating of the surface exposed to the walls of the vacuum chamber, i.e.

$$q_{\text{rad}} - q_{\text{cooling}} = 0. \tag{4.7}$$

Therefore, a steady-state at the initial temperature T_0 is established.

In order to find an analytical solution to Equation 4.4 we use the following simplifications: i) that the condition described by Equation 4.7 is valid at all temperatures during the experiment, and ii) that the values for ρ_e and κ are independent of temperature. Assumption i) is justified as the device is in a quasi steady-state also during the heating ramp as a constant temperature profile would establish itself in about 0.1 s.

With these simplifications Equation 4.4 can be rewritten as

$$\frac{d}{dx}\left(\frac{dT(x)}{dx}\right) = -\frac{1}{\kappa}\left(\frac{I^2\rho_e}{h_{\text{Pt}}h_{\text{Si}}w^2}\right), \tag{4.8}$$

which, taking into account the boundary conditions ($T(0) = T(L) = T_0$), yields

$$T(x) = T_0 + \frac{I^2\rho_e}{2\kappa h_{\text{Pt}}h_{\text{Si}}w^2}(L - x)\,x. \tag{4.9}$$

Figure 4.14 shows temperature profiles across the Pt/SiO_2-n-Si nanostructure, calculated using Equation 4.9 for several values of the electric current flowing through the Pt nanofilm. All parameters used for the calculation are listed in Table 4.1.

As can be seen in Figure 4.14, the temperature profiles are parabolic in shape with only the central section heated to a temperature high enough to desorb H_2O. Here, $T_{\text{des}} = 200$ K

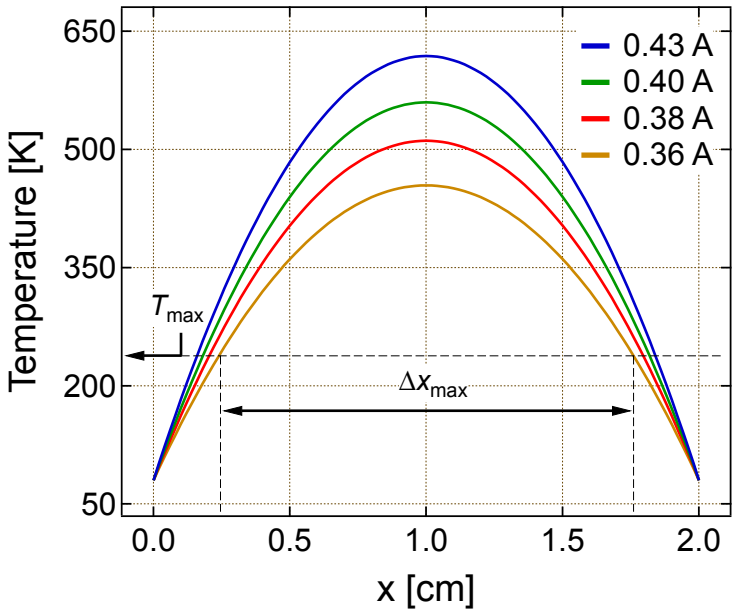

Figure 4.14: Temperature profiles across the surface of the Pt/SiO_2-n-Si nanostructure for different currents flowing through the Pt film calculated using Equation 4.9. T_{des} is the temperature that must be reached in order for a significant amount of H_2O to desorb, Δx_{max} is the length of the region, heated to a temperature above T_{max}.

was chosen as the limiting temperature that must at least be reached in order to observe significant desorption from a surface element arguing that this is about 20 K below the temperature at which we observe the peak in the desorption spectrum. Thus, the area from which H_2O will desorb is given by the product of the width of the Pt/SiO_2-n-Si nanostructure and the length of the section in which the temperature will exceed T_{des}, i.e. $A_{\mathrm{max}} = w\Delta x_{\mathrm{max}}$. At the same time, there are sections at the edges, where the temperature remains lower than the temperature required to desorb H_2O at an appreciable rate. Moreover, the area heated to $T > T_{\mathrm{des}}$ increases with increasing heating power, which in principle could explain the dependence of the amount of desorbed H_2O on the heating power noted, when discussing Figure 4.12.

To lend further credit to this hypothesis, we plot the amount of desorbed H_2O, which is determined from the area under the QMS signal curves (Figure 4.12), as a function of A_{max} derived from the calculation for various heating powers. As shown in Figure 4.15, despite the fact that the values for A_{max} were calculated using a crude model, the amount of desorbed H_2O scales linearly with this quantity. In other words, the N_{H_2O} can be represented by

$$N_{H_2O} = k_2 \, A_{\mathrm{max}}, \tag{4.10}$$

where k_2 is the slope of the line, shown in Figure 4.15. As shown in the inset of Figure 4.12 the calculated values for N_{H_2O} are in a fair agreement with the experimental findings.

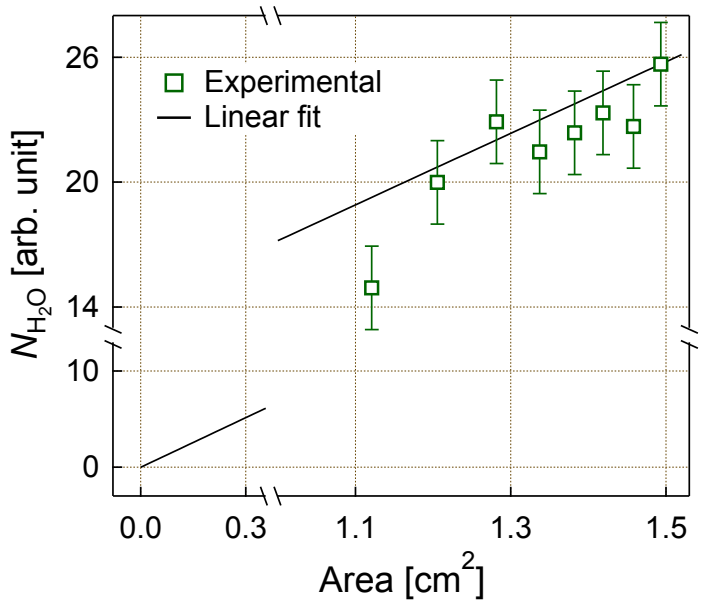

Figure 4.15: Amount of desorbed H_2O (area under the QMS signal curves in Figure 4.12) as a function of $A_{\max} = w\Delta x_{\max}$, the area of the Pt nano film with the temperature $T > T_{\text{des}}$. Here $\Delta x_{\max}$ is the length of the region, heated to a temperature higher than T_{des}, w is the width of the Pt/SiO_2-n-Si nanostructure.

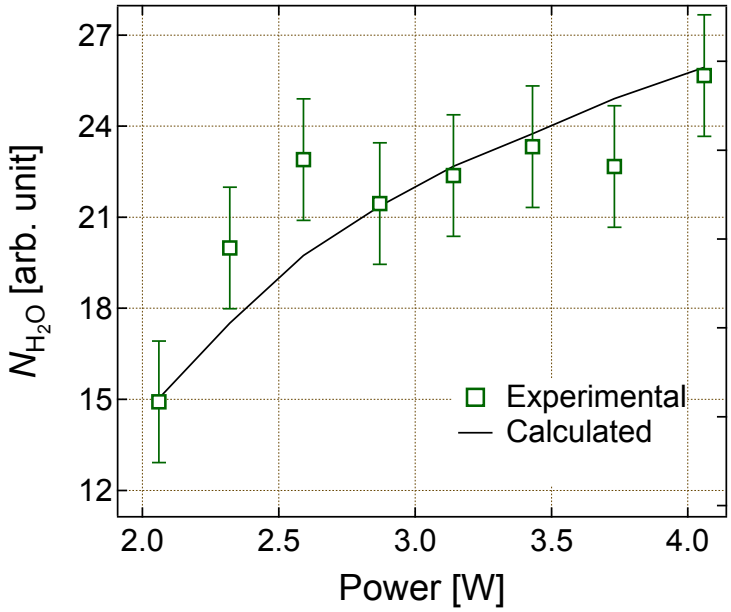

Figure 4.16: Experimental and calculated amount of desorbed water (area under the QMS signal curves) plotted versus heating power.

Table 4.1: The parameters used in the calculation of the temperature profiles along the Pt/SiO_2-n-Si nanostructure

Symbol	Physical parameter	Value
κ_{Pt}	Thermal conductivity of Pt	7.2×10^{-1} W·cm^{-1}·K^{-1}
κ_{Si}	Thermal conductivity of Si	6.1 W·cm^{-1}·K^{-1}
ρ_e	Electric conductivity of Pt	2.5×10^{-6} Ω·cm^{-1}
h_{Pt}	Thickness of Pt nano film	5.0×10^{-7} cm
h_{Si}	Thickness of SiO_2/Si/SiO_2 layer	5.0×10^{-2} cm
T_{wall}	Temperature of chamber walls	300 K
T_0	Initial temperature	80 K

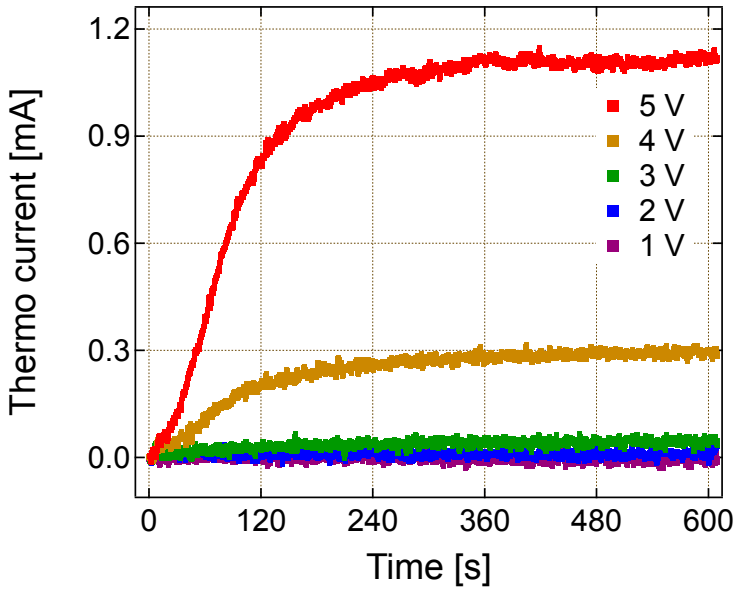

Figure 4.17: Observed device currents when various heating voltages are applied across the Pt film. In this case, the current is thermoelectric in nature arising from the vertical temperature gradient across the Si substrate.

In order to demonstrate that in this set-up heating does not conflict with recording the current between the top Pt electrode and the device back electrode, we have monitored the latter during several heating experiments (Figure 4.17). No spurious currents are observed. The monitored current is identified as thermoelectric current due to the temperature gradient across the Si substrate [59]. This current follows in time the evolution of the device surface temperature, whereas the heating current through the Pt nanofilm has a totally different time dependence. Hence, the set-up presented here enables the simultaneous monitoring of the thermal desorption flux and the detection of chemically induced hot charge carriers.

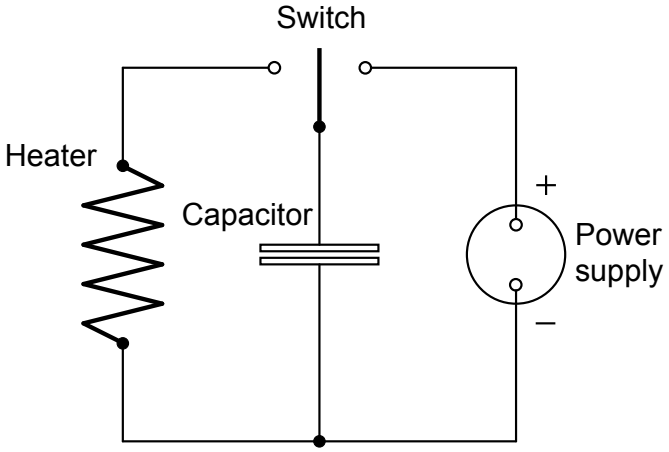

Figure 4.18: The system which allows for the heating with the power obeying an exponential law given by Equation 4.11.

4.4 Pulse heating

In some experiments, which are described in Section 5.2, admission of a gas on the surface of a Pt/SiO_2-n-Si nanostructure caused some changes in temperature of the nanostructure. Analysis of this effect has shown, that such changes in temperature may be attributed to the operation of a heat source with a power, which obeys an exponential law, i.e

$$Q_+ = Q_0 \exp(-t/\tau), \tag{4.11}$$

where Q_0 is the initial heating power at $t = 0$, and τ is the time constant (this parameter represents the time necessary to reach 63.2 % of the final value of the heating power). In our experiments τ was in the range of $0.2 - 0.4$ s. In order to verify this experimentally and to study the thermoelectric effect in the Pt/SiO_2-n-Si nanostructure, caused by these changes in temperature, we used a heating system, which allowed to reproduce a heating mode as described by Equation 4.11. This heating system consisted of a thin film heater and a capacitor, which constitute a RC circuit, and a DC power supply, see Figure 4.18.

In order to understand the principle of operation of this heating system, let us first understand basics of the RC circuit. The simplest RC circuit consists of a capacitor and a resistor [97]. If to charge the capacitor and connect it in series with the resistor, the capacitor will discharge its stored energy through the resistor. The voltage across the capacitor ($U(t)$), which is in this case time dependent, can be found by using Kirchhoff's loop law, where the current through the capacitor ($I_C(t) = -dq(t)/dt = -CdU(t)/dt$, where $q(t)$ is the charge on the capacitor, C is the capacitance, sign "$-$" shows that the capacitor is discharging) must be equal to the current through the resistor ($I_R(t) =$

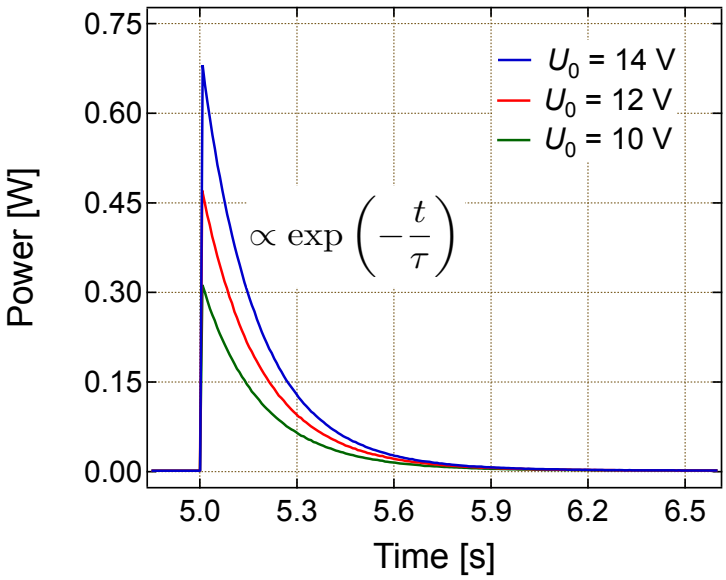

Figure 4.19: Electric power dissipated in 2.4 Ω thin film heater during discharging of a 0.08 F capacitor for several values of voltage on the capacitor when it is charged.

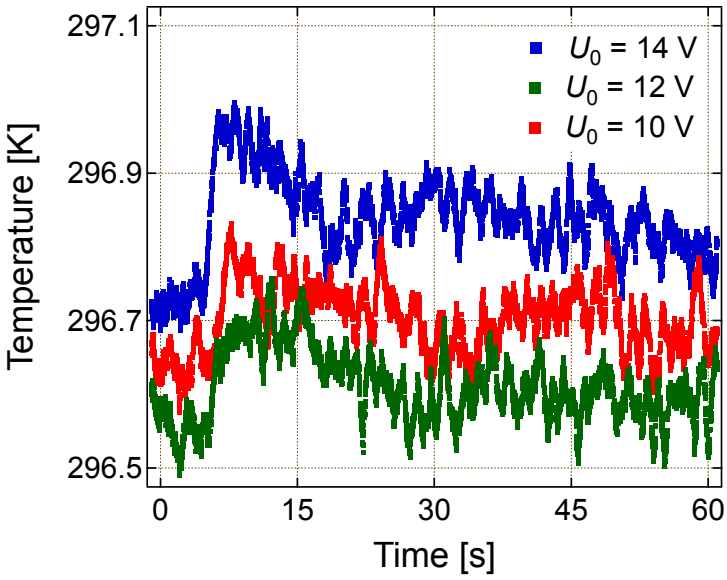

Figure 4.20: Temperature of the Pt/SiO_2-n-Si nanostructure heated using a thin film heater. The electric power dissipated in the heater is shown in Figure 4.19.

$U(t)/R$, where R is the resistance). This results in the following differential equation

$$C\frac{dU(t)}{dt} + \frac{U(t)}{R} = 0. \tag{4.12}$$

Solving this equation for U yields the formula for exponential decay:

$$U(t) = U_0 \exp\left(-\frac{t}{\tau}\right), \tag{4.13}$$

where U_0 is the voltage across the capacitor at time $t = 0$, and $\tau = RC$ is the time constant. The electric power dissipated in the heater can be found using the Joule heating law cite, which suggests $Q_+(t) = U^2(t)/R$.

We used a thin film heater, which consisted of a 100 nm thick film of gold deposited on a $SiO_2/Si/SiO_2$ wafer 20×10×0.5 mm in size. Resistance of the gold film was about 2.4 Ω. Therefore, in order to reproduce the heating mode given by Equation 4.11 with the time constant (τ) in the range of $0.2 - 0.4$ s we used several capacitors, which could be combined to obtain a total capacity in the range of $0.08 - 0.167$ F.

Figure 4.19 shows typical time dependencies of the electric power dissipated in the thin film heater during the discharge of the 0.08 F capacitor. The temperature of the Pt/SiO_2-n-Si nanostructure measured during the discharging of the capacitor on the thin film heater attached to the nanostructure is shown in Figure 4.20.

A comparison of the temperature changes produced by admission of a gas on the surface of a Pt/SiO_2-n-Si nanostructure with the temperature changes produced by the heating system described here is presented in Section 5.2.

Chapter 5

Results and Discussion

In this chapter the main results obtained in the framework of this PhD work are presented. The chapter is organized as follows. At first, the general features of the hydrogen combustion on the surface of thin platinum films deposited on SiO_2/Si substrates are shown. Further, the electric signals and temperature changes measured from a Pt/SiO_2-n-Si nanostructure during oxygen adsorption, which is one of the most energetic steps of the water formation reaction are discussed. Finally, the electric signals and thermal effects associated with the reaction of hydrogen and oxygen molecules on the Pt/SiO_2-n-Si nanostructure in the wide range of temperatures are shown.

5.1 Water formation reaction on platinum: preliminary study

Catalytic combustion of hydrogen on platinum is governed by two processes: chemical heat production and heat loss. Therefore, an important requirement to observe catalytic reaction of water formation on a platinum surface is that the catalyst has a bad thermal contact with the surroundings. Indeed, as pointed out by Kasemo & co-workers [66, 98], as long as the rate of chemical heat production is smaller than the rate of heat loss, the system (gas + catalyst) will be in the stable state, which is controlled by the surface reaction kinetics at the given temperature. However, if to increase the rate of chemical heat production, to make it bigger than the rate of heat loss, it is possible to find a state when the system will be unstable. The excess heat will lead to self-acceleration of the chemical reaction. The system in this state will be already governed by the transport of reactants to the surface of the catalyst. The point, when the system changes from the surface reaction controlled state to the state, controlled by reactants transport, is called **ignition** and can be characterized by the Frank-Kamenetskii condition [66, 98, 99]

$$\frac{dQ_+}{dT} = \frac{dQ_-}{dT}\,, \tag{5.1}$$

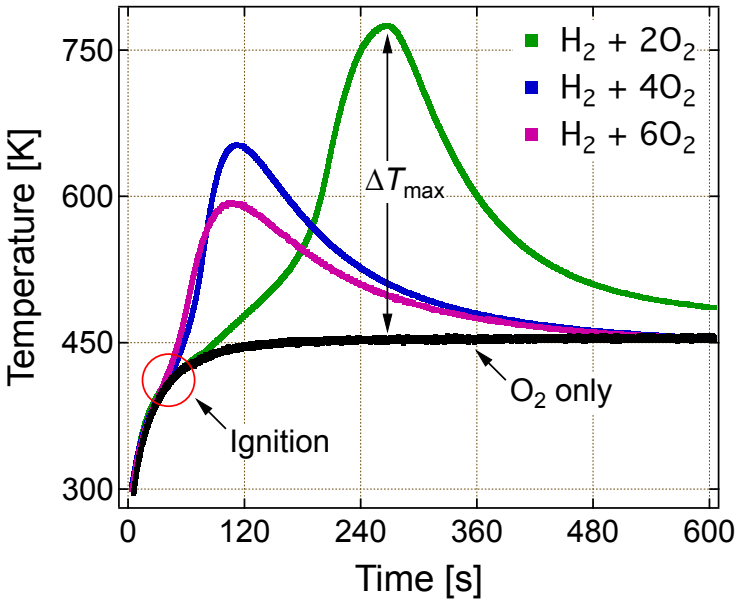

Figure 5.1: Temperature of a platinum nanofilm heated in oxygen and in hydrogen + oxygen mixtures with different concentrations of hydrogen. For all experiments the gas pressure in the chamber is 500 Pa.

where Q_+ and Q_- are the temperature dependent rates of heat production and loss, respectively.

The simplest way to satisfy the condition described by Equation 5.1 is to use a catalyst in a form of a long wire with a small cross-section, which is fixed at the ends. Therefore, the heated wire technique [66] is the most common method for the study of the catalytic combustion of hydrogen. This technique is based on passing a gas mixture (in our case it is the hydrogen + oxygen mixture) at room temperature across a wire or ribbon of a catalytic metal, which is heated by an electric current [100]. In our work, we used a similar method to study the water formation reaction on the surface of a platinum nanofilm, which was deposited on the SiO_2/Si substrate. The platinum nanofilm, placed in the chamber with the hydrogen + oxygen gas mixture, was heated by passing an electric current through it until reaching a critical temperature value (ignition temperature). Then, the catalytic combustion of hydrogen was observed. The resistance of the platinum nanofilm was used to monitor its temperature. The method of heating of the platinum nanofilm by an electric current and measuring its temperature by recording the resistance of the nanofilm is described in detail in Section 4.2.

Figure 5.1 shows the time dependence of the platinum nanofilm temperature, when it is heated in oxygen and in the hydrogen + oxygen mixture with different concentrations of hydrogen. For all experiments the gas pressure in the chamber was 500 Pa. When the platinum nanofilm is heated in oxygen only, the temperature is increased from 300 K to 450 K and then stays constant. However, when oxygen is mixed with hydrogen some

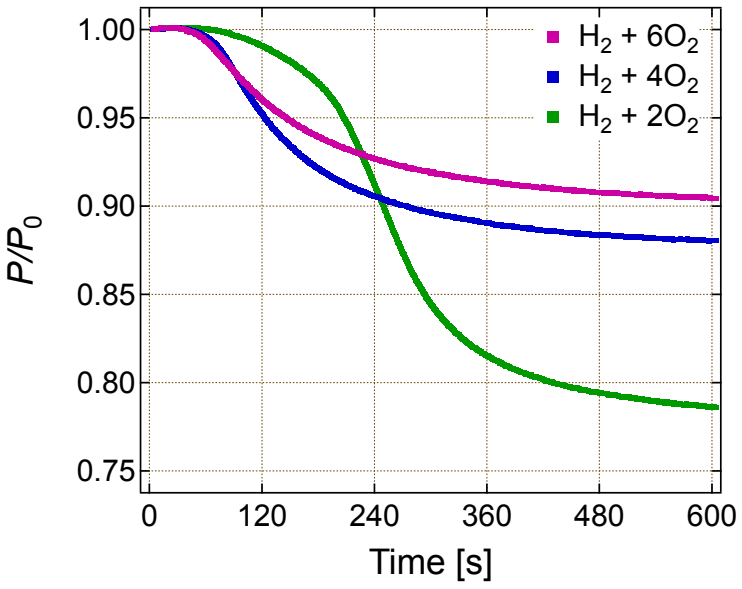

Figure 5.2: Change in pressure in the high vacuum chamber when the water formation reaction takes place on a surface of the platinum nanofilm.

additional heat can be detected after the ignition of hydrogen. When hydrogen starts to burn, the temperature of the platinum nanofilm rapidly increases to a value about $1.5-2.0$ times larger than the temperature during heating in oxygen only, passes through a maximum, and further decreases as a result of reducing the concentration of hydrogen due to its burning. The process of burning of hydrogen was clearly seen by monitoring the gas pressure in the chamber, which begins to decrease rapidly after reaching the temperature at which hydrogen starts to react with oxygen, see Figure 5.2.

Both, the temperature at which the reaction between hydrogen and oxygen starts (T_{ignition}), and the additional heating of the platinum nanofilm as a result of this reaction (ΔT_{max}), strongly depend on the concentration of hydrogen in the gas mixture. This fact is shown in Figure 5.4 and Figure 5.5, where T_{ignition} and ΔT_{max} are plotted versus the relative concentration of hydrogen in the gas mixture, which can be found as $\alpha = P_{\text{H}_2}/(P_{\text{H}_2}+P_{\text{O}_2})$. Here P_{H_2} is the partial pressure of hydrogen, and $P_{\text{H}_2} + P_{\text{O}_2}$ is the total pressure of the hydrogen + oxygen gas mixture. The method of determining ΔT_{max} is shown in Figure 5.1. One can see, that this value was determined by the difference between the temperatures of the Pt nanofilm in the hydrogen + oxygen gas mixture and in oxygen only measured at the same moment of time. Heating of the platinum nanofilm during the reaction between hydrogen and oxygen (ΔT_{max}) increases with the decrease of the hydrogen concentration in the gas mixture. At $\alpha = 0.34$ ΔT_{max} reaches a maximum of about 300 K and then starts to decrease.

The values for T_{ignition} were determined as follows. At first we calculated the first time derivative of the temperatures, shown previously in Figure 5.1, and plotted them versus

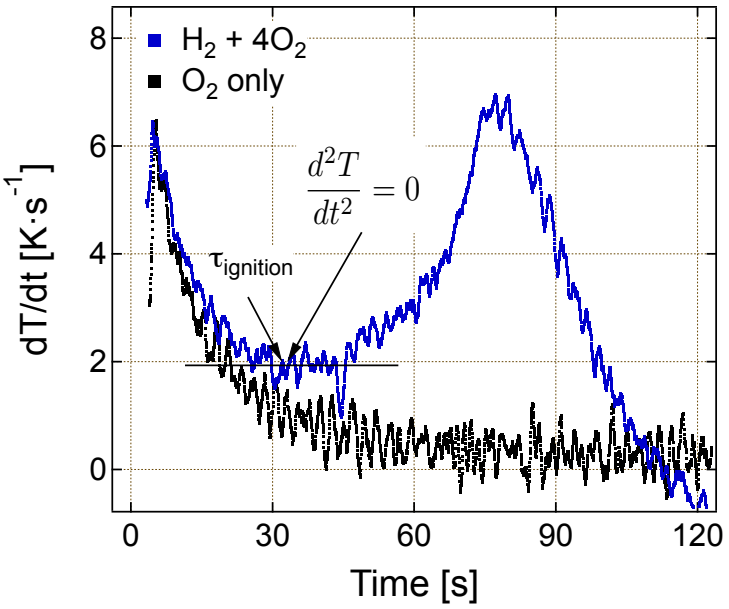

Figure 5.3: The method for determining the moment in time (τ_{ignition}) when the ignition of hydrogen begins. This time is then used for determining the temperature of hydrogen ignition on platinum (T_{ignition}).

time. As can be seen in Figure 5.3, for the case of heating of the Pt nanofilm in oxygen only, dT/dt as a function of time is a decreasing function. At the same time, in the case of heating of the Pt nanofilm in the hydrogen + oxygen gas mixture, a decrease of dT/dt at some point changed to a growth, which we attribute to a chemical heat production due to the hydrogen ignition. Further, the moment in time when the change of dT/dt is observed (the second time derivative in this moment is zero, i.e. $d^2T/dt^2 = 0$), denoted as τ_{ignition}, is obtained. The temperature, which corresponds to τ_{ignition}, is estimated from Figure 5.1 and assigned as T_{ignition}.

As can be seen in Figure 5.4, the temperature of hydrogen ignition decreases with the decrease of the hydrogen concentration in the mixture. The smallest value of T_{ignition}, which was observed in our experiments, was around 380 K for to the relative hydrogen concentration $\alpha = 0.14$. This value is about 60 K higher than the value reported elsewhere for the hydrogen ignition on a heated platinum wire [66, 98].

The observed dependence of T_{ignition} on the hydrogen concentration in the gas mixture can be explained within the previously suggested models. As shown in Reference [66], for $\alpha > 0.1 - 0.2$ the platinum surface is covered by hydrogen atoms prior to ignition. These atoms block the surface and prevent oxygen from the dissociative adsorbing on the platinum surface. Therefore, ignition of the hydrogen + oxygen gas mixture can occur only at the heated platinum surface, as heating promotes H_2 desorption and creates more vacant sites for oxygen. As a result of oxygen adsorption, hydrogen and oxygen atoms start to react. With the increase of the oxygen adsorption rate, the rate of surface reaction

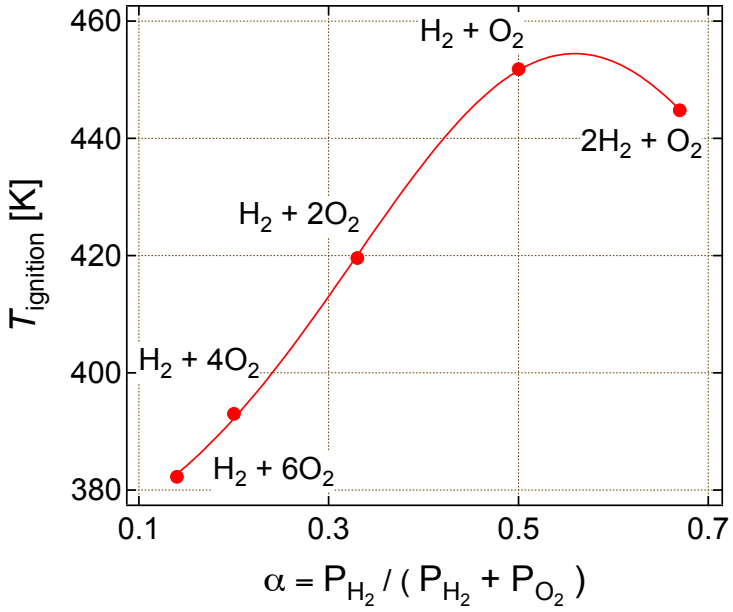

Figure 5.4: The temperature of hydrogen ignition on the platinum nanofilm as a function of relative hydrogen concentration.

also rises (as well as the chemical heat release). At some point the heat produced by the surface reaction is so large enough, that it is not balanced by the heat loss any more and reaction switches to self-acceleration mode (ignition). Thus, obviously, the switch of the reaction to the self-acceleration mode will happen at lower temperatures in the gas mixtures with bigger concentration of oxygen (larger α-values), which is observed by us experimentally. As shown in Reference [66], the transient behavior of the platinum temperature after the ignition point is a result of a combined effect of the transport of reactants in the gas phase and the heat losses.

As discussed in Section 3.3, the properties of the Pt/SiO_2-n-Si nanostructures are sensitive to temperature. Moreover, after reaching some point, which is around 600 − 650 K, these properties can be changed irreversibly. This in turn leads to damage of the potential barriers at the metal-oxide interfaces, which are necessary for detection of chemically induced electronic excitations. Therefore, based on the above mentioned data it can be concluded, that the use of the Pt/SiO_2-n-Si nanostructures to study the water formation reaction in oxygen-rich gas mixtures ($\alpha < 0.3$) is more preferable because of two reasons: (1) in oxygen-rich gas mixtures the surface reaction starts at lower temperatures, and (2) heating of the platinum surface is not big enough to damage the nanostructure, but still notable to allow studying the reaction.

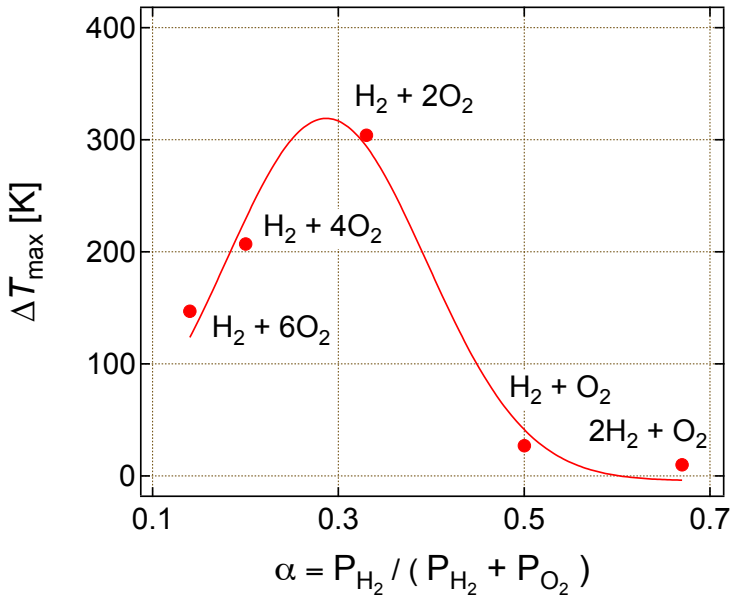

Figure 5.5: The maximal value of heating of the platinum nanofilm during the water formation reaction as a function of relative hydrogen concentration. The line shows a fit of the experimental data using a Gaussian function.

5.2 Charge transfer in Pt/SiO_2-*n*-Si nanostructures induced by adsorption of oxygen molecules

5.2.1 Kinetics of the current induced by adsorption of oxygen

As shown in Section 1.4, dissociative adsorption of oxygen on a platinum surface is one of the first and the most energetic steps of the water formation reaction. Therefore, we decided to pay particular attention to the study of this reaction step. In this section, we report on the use of a Pt/SiO_2-*n*-Si MOS nanostructure to study processes of electric charge generation and transfer induced by adsorption of oxygen molecules on the polycrystalline surface of platinum.

Before all the experiments with oxygen the following procedure was carried out to clean the surface of the Pt/SiO_2-*n*-Si nanostructure: (1) outgassing at 423 K for 10 h in 10^{-4} Pa vacuum, (2) heating to 373 K for 2 h in 10 Pa of oxygen, and (3) outgassing at 423 K for 20 h in 10^{-4} Pa vacuum, followed by the natural cooling to room temperature.

After the surface of the Pt/SiO_2-*n*-Si nanostructure was cleaned its surface was exposed to oxygen at different gas pressures and the electric current induced by the interactions of the oxygen molecules with the surface was measured. Hereafter, we will call this current the **current signal**. Figure 5.6a shows typical current signals detected between the platinum top and indium back electrode of the Pt/SiO_2-*n*-Si nanostructure exposed to oxygen. The admission of oxygen starts at the time moment $t_0 = 5$ s, when the pres-

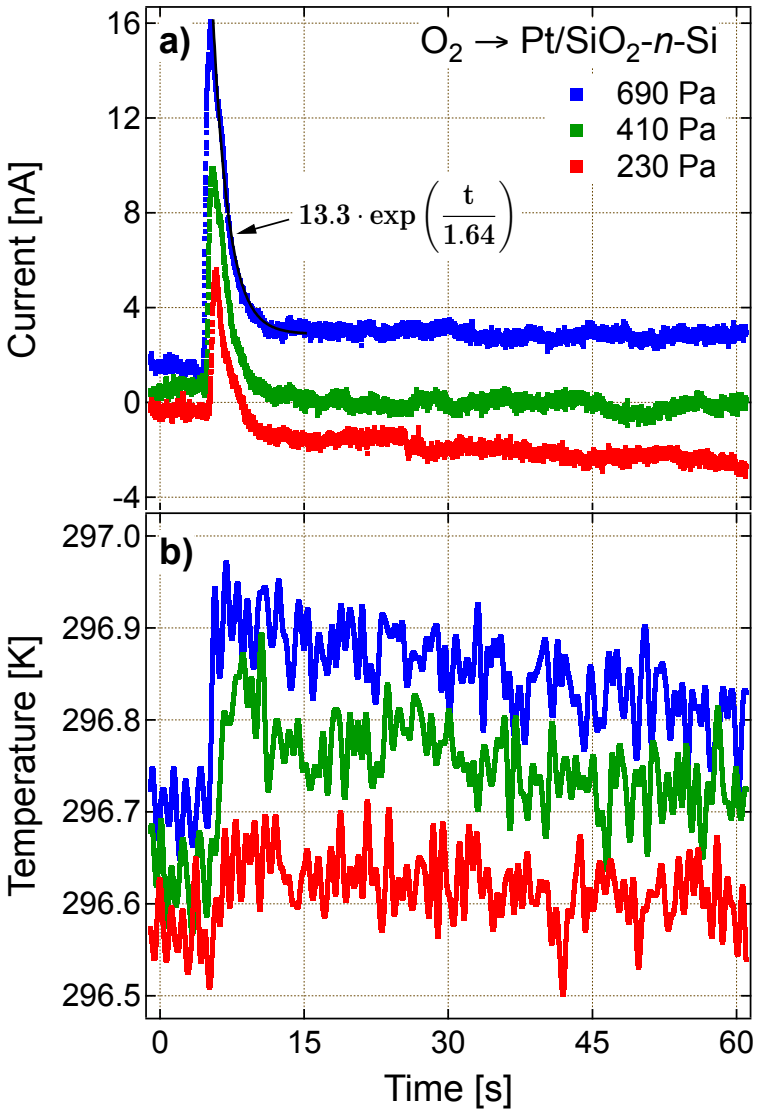

Figure 5.6: a) Current detected from the Pt/SiO_2-*n*-Si nanostructure exposed to molecular oxygen. b) Changes in temperature of the nanostructure measured during the experiment.

sure in the chamber rises from the base vacuum (2×10^{-4} Pa) to 230, 410 or 690 Pa in approximately $\Delta t = 3.0$ seconds. The pressure changes in the HV chamber during admission of oxygen are shown in Figure 5.7. For all pressures, the current signal measured from the Pt/SiO_2-*n*-Si nanostructure has a sharp peak, observed at the beginning of the oxygen admission, which decays with time during the experiment. As can be seen in Figure 5.6a, this decay is described by an exponential function $I = I_0 \exp(-t/\tau_{O_2})$, with the amplitude 6.6 nA, 9.8 nA, 13.3 nA and the time constant $\tau_{O_2} = 1.64$ s for 230, 410 and 690 Pa respectively.

Simultaneously with the appearance of the current signal, small changes in temperature of the Pt/SiO_2-*n*-Si nanostructure can be observed during the admission of oxygen. As shown in Figure 5.6b, at first the temperature rises by about $0.1 - 0.2$ K and then

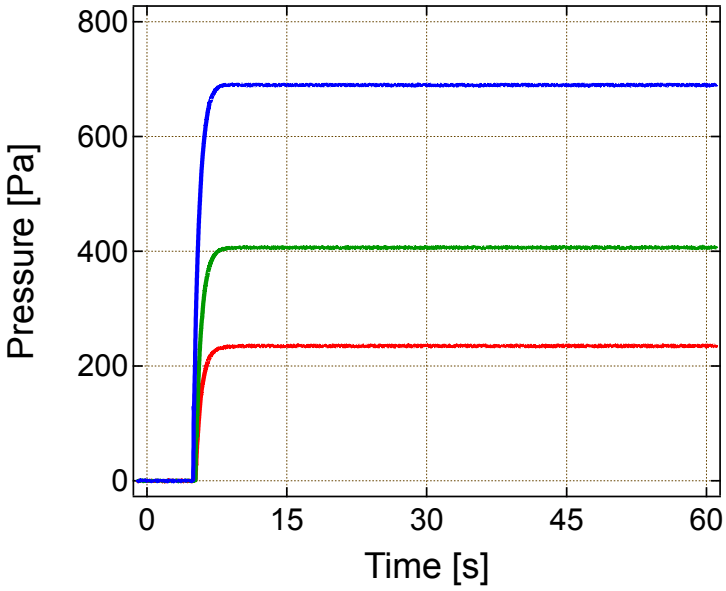

Figure 5.7: Gas pressure in the high vacuum chamber with the Pt/SiO_2-n-Si nanostructure exposed to oxygen for three different experiments.

slowly decreases towards the initial value. These changes in temperature of the Pt/SiO_2-n-Si nanostructure when its surface is exposed to oxygen, will be analyzed in detail in Section 5.2.2.

It is interesting to note, that the amplitude of the current signal, observed when the surface of the Pt/SiO_2-n-Si nanostructure is exposed to oxygen, is sensitive to the history of the surface. The biggest amplitude of the current signal is observed in the experiments during the first admission of oxygen to the nanostructure, which was cleaned by the method described above. If one take the amplitude of the current signal of this first admission of oxygen as 100%, as it is shown Figure 5.8a, the second admission of oxygen on the Pt/SiO_2-n-Si nanostructure, which was already exposed to oxygen and was not cleaned, leads to a much weaker current signal, which is shown in Figure 5.8b. The amplitude of this signal is only about $25 - 27$ % of the amplitude of the signal, observed during the first admission of oxygen. The third admission of oxygen does not lead to a measurable current signal. However, outgassing of the Pt/SiO_2-n-Si nanostructure at $T \geq 400$ K for $3 - 4$ hours in high vacuum results in the recovery of the signal amplitude to the initial value (compare Figure 5.8a and Figure 5.8c).

There are several mechanisms proposed to explain the appearance of the electric current in the composite nanostructures during interactions of their surface with gas particles. These mechanisms can be divided conventionally into two groups. According to mechanisms from the **first group**, interactions of the gas particles with the metal surface lead to excitation of hot electrons with energies above the Fermi level of the metal, and hot holes with energies below the Fermi level due to non-adiabatic dissipation of the chemical

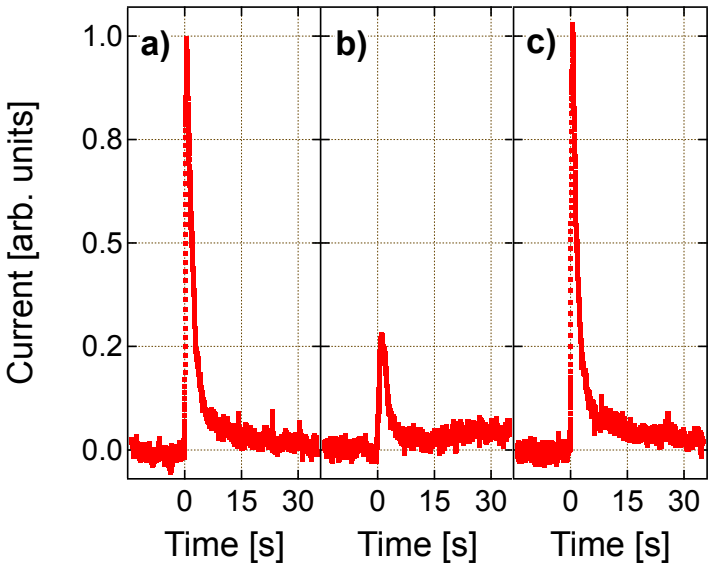

Figure 5.8: Normalized current detected from the Pt/SiO_2-n-Si nanostructure exposed to molecular oxygen: a) first admission on a cleaned surface, b) second admission (third and further admission of oxygen does not lead to a measurable current signal), and c) after outgassing of the nanostructure at 423 K for $3-4$ hours in 10^{-4} Pa vacuum.

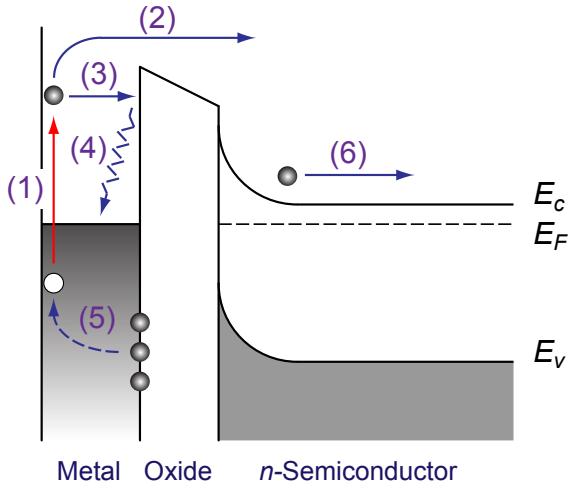

Figure 5.9: Schematic representation of possible mechanisms of an electric current generation in the Pt/SiO_2-n-Si nanostructure during adsorption of oxygen. Here (1) is the excitation of an $e-h$ pair, (2) is the transport of a hot electron over the potential barrier, (3) is the transport of a hot electron with the energy lower then the potential barrier height, (4) is the thermalization of a hot electron, (5) is the neutralization of a hot hole by an electron donor state at the metal-oxide interface, and (6) is the electron transport due to a thermoelectric effect in the n-Si layer.

energy [2, 4, 5, 6, 7, 8, 12, 13, 14]. The excitation of an $e-h$ pair is shown as process (1) in Figure 5.9. In the composite nanostructures, such as MS and MOS diodes, these charge carriers can be detected as an electric current due to their ballistic transport through the top metal electrode and further emission over the potential barrier into the semiconductor layer [2, 5], which is shown as process (2) in Figure 5.9. As shown in Reference [2], in the composite nanostructures based on n-type semiconductors only excited electrons can be effectively emitted over the potential barrier. Thus, the prevailing type of the chemically excited charge carriers detected in this type of nanostructures are electrons.

As pointed out in Reference [10], another mechanism of detection of the chemically excited charge carriers is also possible in MOS nanostructures due to a big number of interface charges and defect levels existing in these structures. This mechanism starts to play a role in the case of low energy chemical processes, when the energy of the chemically excited electrons is not big enough to overcome the potential barrier (this case is shown as process (3) in Figure 5.9). As a result, the excited electron, reflected from the potential barrier, can lose its energy due to the thermalization process, which is denoted as process (4) in Figure 5.9. At the same time, the hot holes remaining in the valence band of the metal can also travel to the metal-oxide interface, where they can neutralize the electron donor states below the Fermi level, existing in MOS nanostructures (see process (5) in Figure 5.9). This process leads to discharging of the interface and can be observed due to compensatory current signal [10].

As shown in Reference [2], the current signal, created due to the processes described by mechanisms of the first group, should reflect the chemical reaction kinetics. In our case this means, that if the current signal shown in Figure 5.6a is due to the generation and transport of hot electrons and holes this current signal should follow the kinetics of oxygen adsorption on the platinum surface. Hence, it can be written as [2]:

$$I(t) = \alpha q A \frac{d\Theta(t)}{dt} \tag{5.2}$$

where α is the yield, which gives a number of electrons detected per chemical reaction event, q is the electron charge, A is the Pt area exposed to gas, and $\Theta(t)$ is the time dependent coverage. According to Equation 5.2, the current signal should be maximal at the initial moment of time, when the platinum surface has the largest number of sites for the adsorption of oxygen. Further, the current signal should decrease to zero after the surface is fully covered with the oxygen molecules.

In order to find the time interval, necessary for oxygen to fully cover the Pt surface, let us consider a kinetic model of gas-surface interactions. This time interval will allow us to estimate the rate at which the current signal should decay, associated with the adsorption of oxygen. As shown in Section 1.3 (see Equation 1.21), interactions of oxygen molecules with the platinum surface occur via dissociative adsorption. Therefore, using

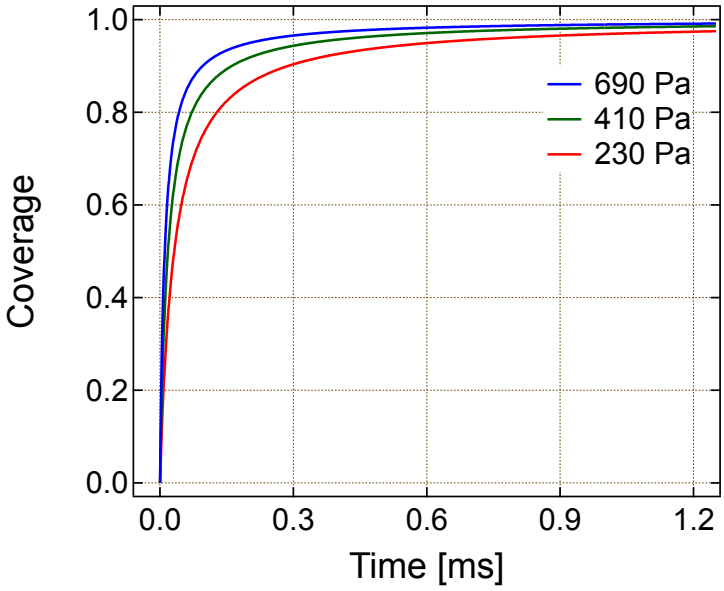

Figure 5.10: Calculated coverages of oxygen on a platinum surface for different gas pressures.

the Langmuir model the rate equation can be written as

$$\frac{d\Theta(t)}{dt} = 2F_{O_2}S_0(1-\Theta(t))^2\,, \tag{5.3}$$

where $F_{O_2} = P_{O_2}A_S/\sqrt{2\pi m_{O_2}k_BT}$ is the flux of oxygen molecules, P_{O_2} is the oxygen pressure, $S_0 = 0.023$ the initial sticking coefficient [60], $A_S = 1/N_{Pt}$ is the area of a Pt site, $N_{Pt} = 1.58 \times 10^{15}$ cm^{-2} the number of adsorption sites on the Pt surface, m_{O_2} is the mass of an oxygen molecule, k_B is the Boltzmann constant, and T is the temperature. Taking into account initial conditions $\Theta(0) = 0$, this equation can be solved, yielding

$$\Theta(t) = \frac{2F_{O_2}S_0t}{1+2F_{O_2}S_0t}\,. \tag{5.4}$$

Equilibrium coverages of oxygen on the platinum surface, calculated using Equation 5.4 with the assumption that the sticking coefficient $S = S_0 =$ constant, are shown in Figure 5.10. As can be seen, the Pt surface is fully covered by oxygen molecules within several milliseconds for the gas pressures considered in this work. Thus, the exponential decay of the current signal with the time constant $\tau_{O_2} = 1.64$ s, shown in Figure 5.6, cannot be explained in terms of the Langmuir adsorption model.

Another puzzle, which we cannot presently resolve, is the disappearance of the current signal from the Pt/SiO_2-n-Si nanostructure after experiments with oxygen and its recovery by outgassing in a high vacuum. The simplest explanation of the current signal reduction after the first admission of oxygen and its disappearance after the second admission of

oxygen, shown in Figure 5.8, would be blocking of the Pt surface by already adsorbed oxygen atoms. However, this explanation cannot explain the recovery of the current signal after the outgassing of the Pt/SiO_2-n-Si nanostructure at $T \geq 400$ K for several hours in a high vacuum. Indeed, desorption of oxygen from platinum happens at $800 - 900$ K (see, for example Reference [71]), which is much higher that the temperature which is used during the outgassing of the nanostructure. This means, that the outgassing does not clean the Pt surface from the adsorbed oxygen, which in turn means that processes of adsorption and desorption of oxygen on the surface of the Pt/SiO_2-n-Si nanostructure are not responsible for the changes in the current signal magnitude shown in Figure 5.8. Indeed, according to Reference [71] the rate of thermal desorption of oxygen from the platinum surface is described by

$$R_{\mathrm{d}} = \nu_{\mathrm{d}} \vartheta^2 \exp\left(-\frac{E_{\mathrm{d}}^0 - a\vartheta}{k_{\mathrm{B}} T}\right), \tag{5.5}$$

where ϑ is the absolute oxygen coverage, $E_{\mathrm{d}}^0 = 2.21$ eV is the activation energy for desorption, $a = 0.43$ eV is a constant, and $\nu_{\mathrm{d}} = 2.4 \times 10^{-2}$ cm^2·s^{-1} is the pre exponential factor. Neglecting the dependence of the activation energy for desorption on the oxygen coverage, one can calculate using Equation 5.5 that at $T = 900$ K the rate of oxygen desorption is factor of 10^{15} larger than at $T = 400$ K. In other words, if to assume that it takes some seconds to desorb a monolayer of oxygen at 900 K, then one would need around 10^7 years to complete the same operation at 400 K.

According to mechanisms from the **second group**, interactions of the gas particles with the metal surface lead to heating of the surface, which in turn can give rise to a current signal. As a rule, two possible processes leading to a current signal in the composite nanostructures are considered [8, 17]. The first process is the thermionic emission of electrons from the top metal electrode into the semiconductor layer over the potential barrier. This process can be depicted similarly to the process (1) in Figure 5.9. However, one should keep in mind, that unlike the emission of hot electrons, which was described above, in the case of thermionic emission electrons, transported over the potential barrier, are in the ground state. In addition to the thermionic emission, heating of the composite nanostructures can give rise to a current signal due to the thermoelectric effect (also known as the Seebeck effect). This effect is based on the ability of majority charge carriers (in n type conductors these are electrons) to move in the direction opposite to a temperature gradient, producing a small electric potential difference across the nanostructure. This is illustrated in Figure 5.9 as the process (6). The electric potential difference can induce a current signal in a similar way as in the case of applying to the nanostructure an external voltage bias.

The preliminary study of the thermionic emission and thermoelectric effects in the composite nanostructures is discussed in Section 1.2.2. The contribution of these effects

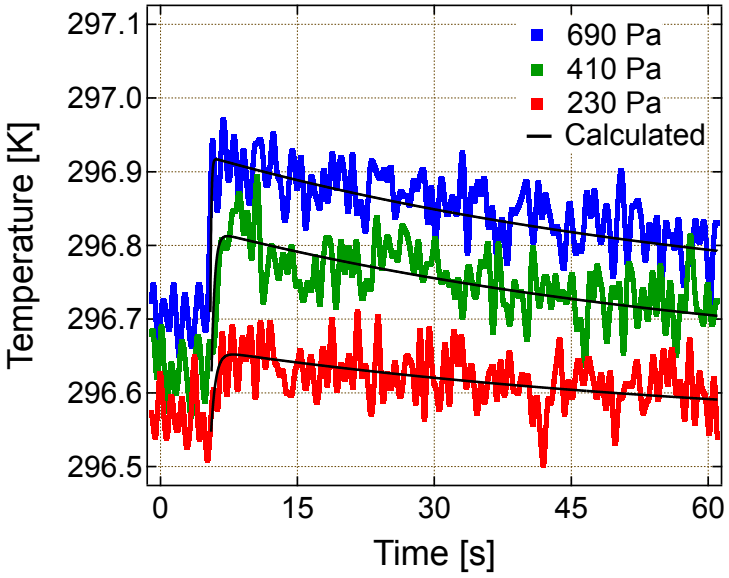

Figure 5.11: Measured and calculated changes in temperature of the Pt/SiO_2-*n*-Si nanostructure exposed to oxygen.

to the magnitude of the current signal measured from the Pt/SiO_2-*n*-Si nanostructure, when it is exposed to oxygen, is estimated in Section 5.2.2.

5.2.2 Thermoelectric effects in Pt/SiO_2-*n*-Si nanostructures during adsorption of oxygen

Some articles proposed that the current measured from the MS and MOS nanostructures in the course of surface chemical reactions can be a result of thermionic emission and thermoelectric effects [16, 17]. Indeed, it is well known that interactions of gas particles with a metal surface lead to a release of significant amounts of heat [16, 17, 101]. As a consequence, small temperature gradients across the nanostructures can be created, which in turn work as a driving force for thermoelectric [16, 17] and thermionic emission [8, 13, 17] currents.

In order to find out whether the thermionic emission and thermoelectric effects, caused by the change in temperature of the Pt/SiO_2-*n*-Si nanostructure exposed to oxygen, can lead to the current signals shown in Figure 5.6a, we have: (1) considered processes of the heat generation on the Pt surface and transport of this heat through the Pt/SiO_2-*n*-Si nanostructure, (2) estimated the heating power responsible for the temperature changes during exposure of the Pt/SiO_2-*n*-Si nanostructure to oxygen, (3) simulated heating caused by admission of oxygen using a technique of pulse heating, described in Section 4.4 and studied the charge transport accompanied this process. Further, we consider each of these steps in more detail.

The change in temperature (ΔT) of the Pt/SiO_2-n-Si nanostructure with time during the gas admission can be written as

$$C_{\mathrm{NS}}\frac{d\Delta T}{dt} = Q_+ - Q_-, \tag{5.6}$$

where C_{NS} is the heat capacity of the nanostructure (NS), Q_+ and Q_- are the powers of heat generation and loss, respectively. Let us assume, that the power of heat generation obeys the same law as the current signal detected from the Pt/SiO_2-n-Si nanostructure, when it is exposed to oxygen. Thus, it can be written as $Q_+ = Q_0 \exp(-t/\tau_h)$, where Q_0 is the initial value of the heating power and τ_h is the time constant. The power of heat loss in our case can be written as

$$Q_- = \varepsilon\sigma A(T^4 - T_0^4) + \kappa_1\Delta T + \kappa_2\Delta T. \tag{5.7}$$

The first term of the right side of Equation 5.7 describes the heat loss by the Pt/SiO_2-n-Si nanostructure due to the radiation. Here ε is emissivity, σ is the Stefan-Boltzmann constant, A is the surface area, and T_0 is the ambient temperature. The second term describes the loss of heat due to the cooling by a gas (convection). Finally, the third term describes the loss of heat by the conduction to the heat sink via the electrical wires connected to the Pt/SiO_2-n-Si nanostructure. Constants κ_1 and κ_2 denote the convection and conduction heat transfer coefficients. For small changes in temperature the heat loss due to the radiation can be approximated by a linear expression $\varepsilon\sigma A(T^4 - T_0^4) = \varepsilon\sigma A T_0^3 \Delta T$. Thus, Equation 5.7 can be rewritten as

$$C_{\mathrm{NS}}\frac{d\Delta T}{dt} = Q_0 \exp\left(-\frac{t}{\tau_h}\right) - \varkappa\Delta T, \tag{5.8}$$

where $\varkappa = \varepsilon\sigma A T_0^3 + \kappa_1 + \kappa_2$ is the combined heat transfer coefficient.

Taking into account initial conditions $\Delta T(0) = 0$ K, Equation 5.8 can be solved analytically, yielding

$$\Delta T = \frac{Q_0}{\beta}\left[1 - \exp\left(-\frac{\beta t}{C_{\mathrm{NS}}}\right)\right]\exp\left(-\frac{\varkappa t}{C_{\mathrm{NS}}}\right), \tag{5.9}$$

where $\beta = (C_{\mathrm{NS}} - \varkappa\tau_h)/\tau_h$.

Figure 5.11 shows results from the fitting the experimentally measured changes in temperature of the Pt/SiO_2-n-Si nanostructure (these experimental curves have already been shown previously in Figure 5.6b) using Equation 5.9. It can be seen that the calculated curves describe well the experimental data both qualitatively and quantitatively, that indicates the correctness of the previously stated assumption about an exponential decay of the heating power with time. From the comparison of the calculated and ex-

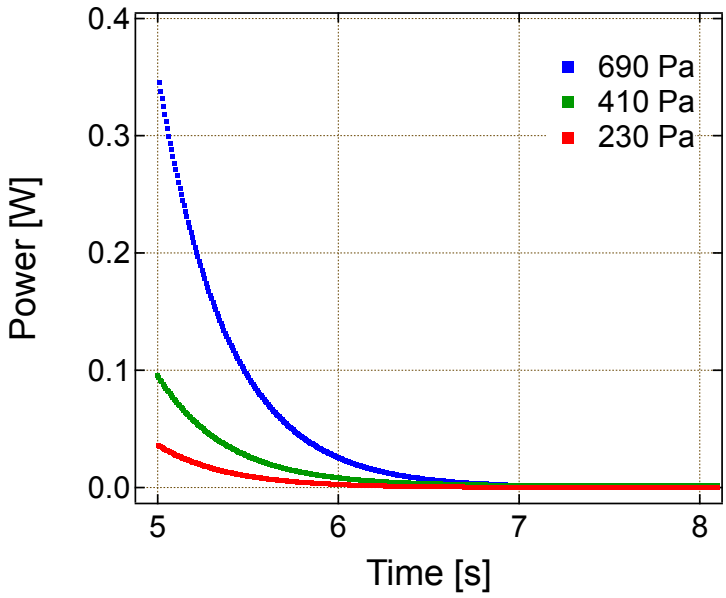

Figure 5.12: Calculated heating powers responsible for the temperature changes during admission of oxygen on the surface of the Pt/SiO_2-n-Si nanostructure shown in Figure 5.11.

perimental curves we derived following parameters: the initial heating power (Q_0), which is equal to 3.6×10^{-2} W, 9.4×10^{-2} W, and 3.45×10^{-1} W for 230 Pa, 410 Pa, and 690 Pa respectively; the combined heat transfer coefficient $\varkappa = 2.73 \times 10^{-3}$ W·K^{-1}, and the time constant $\tau_h = 0.38$ s. The last two parameters are the same for all values of the oxygen pressure. For all calculations we used the heat capacity of the Pt/SiO_2-n-Si nanostructure $C_{\mathrm{NS}} = 1.64 \times 10^{-1}$ J·K^{-1}. This value is obtained by taking into account the size and specific heat capacities of all components of the nanostructure. Heating powers, which are responsible for the temperature changes during the admission of oxygen on the surface of the Pt/SiO_2-n-Si nanostructure are shown in Figure 5.12.

In the next stage of our research, using a method of pulse heating, which is described in Section 4.4, we simulated heating of the Pt/SiO_2-n-Si nanostructure and measured the electric current signals accompanying this process. The parameters of the heating system (such as capacitance of the capacitor and voltage applied to the capacitor during charging) were chosen such that the heating power during discharging the capacitor on the thin film heater, happened in accordance with the curves shown in the Figure 5.12.

Figure 5.13a shows a typical current signal, measured from the Pt/SiO_2-n-Si nanostructure when it is heated using a thin film heater. The current signal measured from the same nanostructure during the oxygen admission is also shown in this figure for comparison. The inset in Figure 5.13a shows an electric circuit diagram for the heating system, which was used in this experiment. The power, dissipated by the thin film heater, was chosen so as to fit the heating power, calculated for the experiment with the admission

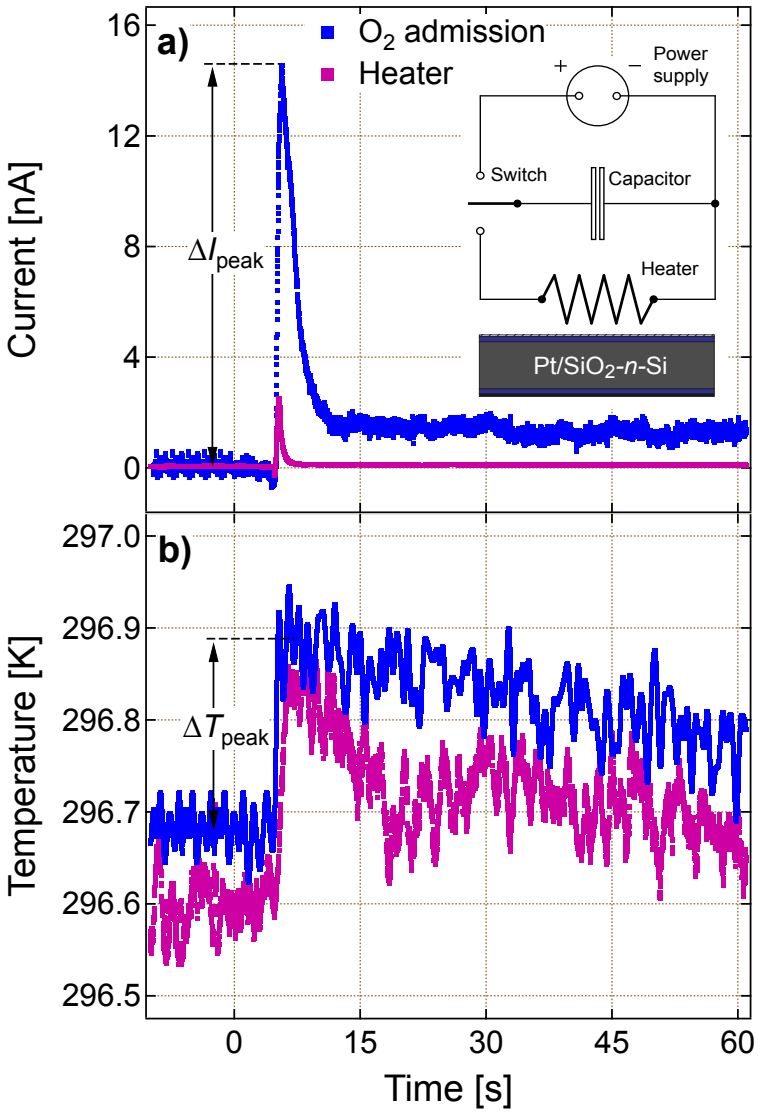

Figure 5.13: a) Current detected from the Pt/SiO_2-*n*-Si nanostructure during the i) oxygen admission (P_{O_2} = 690 Pa) and ii) pulse heating by a thin film heater. b) Corresponding changes in temperature of the nanostructure. Inset: Electric circuit diagram for the heating system.

of 690 Pa oxygen. Corresponding changes in temperature, observed when the Pt/SiO_2-n-Si nanostructure was exposed to oxygen or heated by a thin film heater, are shown in Figure 5.13b.

As can be seen in Figure 5.13, the maximum temperature rise (ΔT_{peak}) and its decay with time are rather similar for experiments with the oxygen admission and heating of the thin film heater. Therefore, one can expect similarity of the thermionic emission and thermoelectric effects in this two experiments. However, the current signals, measured from the Pt/SiO_2-n-Si nanostructure, are notably different. Likely, the current signal, measured when the nanostructure is heated with the use of the thin film heater, can be attributed to the joined action of the thermionic emission and thermoelectric effects. Indeed, according to our analysis, given in Section 1.2.2, both of these effects in the composite MS and MOS nanostructures are the result of a temperature gradient, which can be created when these structures are unevenly heated (as in our case, when the MOS structure is heated only from above by a heater or due to gas-surface interactions). The temperature gradient, in turn, is proportional to the heating power [17], i.e. $\delta T_{\text{NS}} \propto Q_+$, where δT_{NS} is the temperature difference across the nanostructure, which is in a good agreement with our observation, that the the current signal, measured when the Pt/SiO_2-n-Si nanostructure is heated by a thin film heater, decreases with the same time constant ($\tau_h = 0.38$ s) as the heating power. The magnitude of this current signal also agrees well with the estimates given in Section 1.2.2.

Similarity of the changes in temperature, shown in Figure 5.13b, indicates that the heating power in the experiment where the nanostructure is exposed to 690 Pa of oxygen is similar to the one dissipated by a thin film heater. At the same time, the magnitude of the current signal (ΔI_{peak}), measured during oxygen admission, is significantly larger. Moreover, the decay of this current signal is characterized by a larger time constant ($\tau_{O_2} = 1.64$ s versus $\tau_h = 0.38$ s). These facts suggest a non-thermal nature of the current signals detected when the Pt/SiO_2-n-Si nanostructure is exposed to oxygen.

The difference between the current signals, measured from the Pt/SiO_2-n-Si nanostructure exposed to oxygen and heated with the use of the thin film heater, becomes even more notable if one compares characteristics of these signals at different heating powers. To demonstrate this, we will use the following parameters: the maximal magnitude of the current signal (ΔI_{peak}), the maximal change in temperature of the Pt/SiO_2-n-Si nanostructure (ΔT_{peak}), and the value of the electric charge transferred through the MOS junction. The method of determining the first two parameters (ΔI_{peak} and ΔT_{peak}) is indicated in Figure 5.13. The last parameter (the electric charge transferred through the MOS junction), was determined by measuring the area under the curves for the current signal, detected with the use of the Pt/SiO_2-n-Si nanostructure, plotted versus time.

Figure 5.14 shows the maximal change in temperature of the Pt/SiO_2-n-Si nanostructure as a function of the initial heating power (Q_0) for experiments, in which the

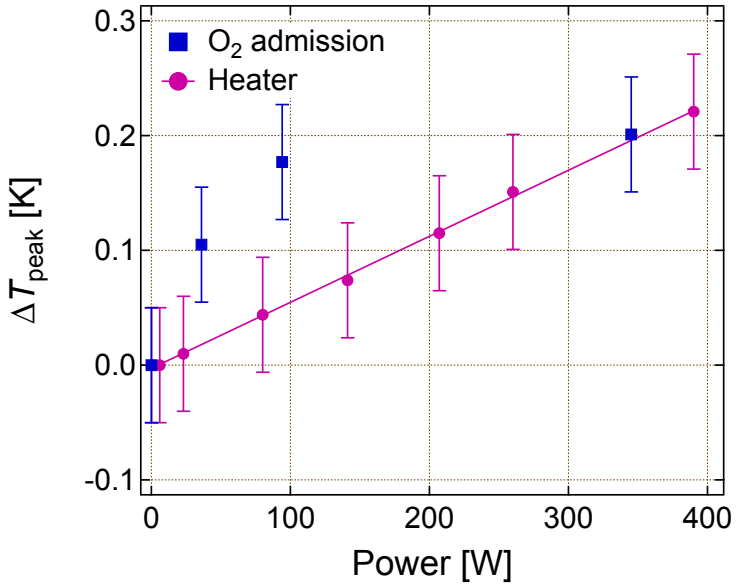

Figure 5.14: The maximal change in temperature of the Pt/SiO_2-*n*-Si nanostructure as a function of the initial heating power.

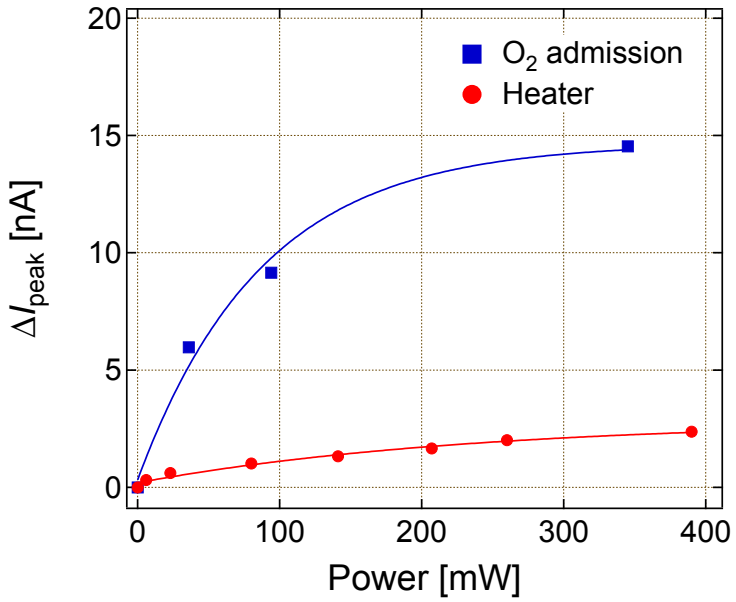

Figure 5.15: The maximal magnitude of the current signal measured from the Pt/SiO_2-*n*-Si nanostructure in experiments with the admission of oxygen and using a thin film heater versus the initial heating power.

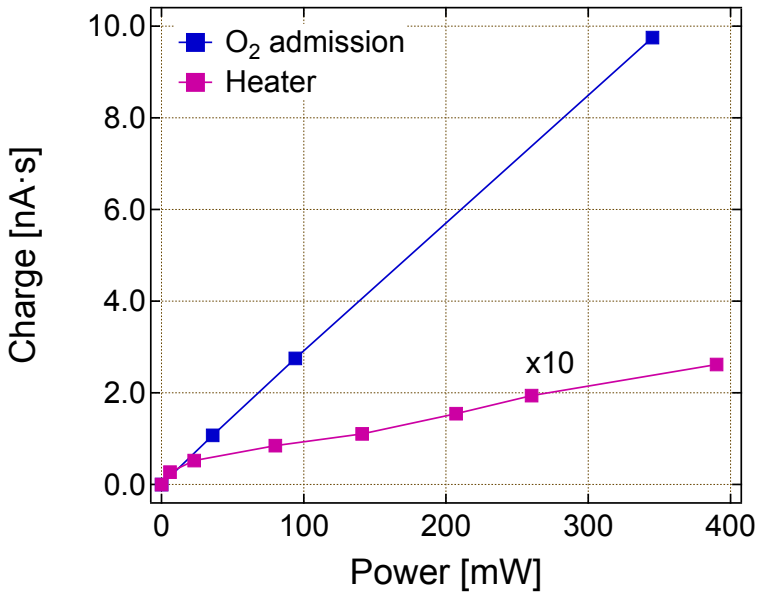

Figure 5.16: The electric charge transferred through the Pt/SiO_2-*n*-Si nanostructure in experiments with the admission of oxygen and using a thin film heater versus the initial heating power.

nanostructure was exposed to oxygen or heated by the thin film heater. In the case of using the thin film heater, ΔT_{peak} is a linear function of the initial heating power, while one can see some deviation from this linear dependence for values of ΔT_{peak}, measured in experiments with oxygen. However, the magnitudes of the changes in temperature are comparable: in both kinds of experiments the maximum value of ΔT_{peak} does not exceed 0.23 K. At the same time, the maximal magnitude of the current signal, measured from the Pt/SiO_2-*n*-Si nanostructure in experiments with the admission of oxygen and using a thin film heater, differs by about an order of magnitude, which is clearly seen in Figure 5.15. Extrapolation of the curve, recorded in the experiment with the thin film heater, indicates that in order to obtain the same magnitude of the current signal as in experiments with oxygen, the heating power, dissipated by the thin film heater, should be about several watts, which is significantly larger, than the one used in our experiments. This in turn contradicts our estimations of the heating power dissipated during exposure of the Pt/SiO_2-*n*-Si nanostructure to oxygen.

The difference between the current signals, measured from the Pt/SiO_2-*n*-Si nanostructure in experiments with oxygen and the thin film heater, are even more notable if one compares the electric charges transferred through the MOS junction. The value of the transferred electric charge allows for the evaluation of the total amount of the electric charge carriers detected by the nanostructure. As shown in Figure 5.16, for equal values of the heating power, the amount of the transferred electric charge, associated with the thermal effects, is only $2 - 10$ % of the one measured in experiments with oxygen. Thus,

we can conclude that the thermionic emission and thermoelectric effects can actually lead to the appearance of measurable current signals in the Pt/SiO_2-*n*-Si nanostructures. However, based on the given above analysis, we can say that these thermal effects can not be considered as the only source the current signals measured from this nanostructure during the admission of oxygen.

5.3 Charge transfer in Pt/SiO_2-*n*-Si nanostructures induced by hydrogen + oxygen reaction

As shown in previous section, exposure of the Pt/SiO_2-*n*-Si nanostructure to oxygen molecules produces some electrical signals, which can be measured between the contacts of the nanostructure as a current. In this section we describe the new features of these signals, which can be observed when oxygen, admitted on the surface of the Pt/SiO_2-*n*-Si nanostructure, is mixed with hydrogen.

This section is organized as follows: at first, we look at the difference of the signals detected when the Pt/SiO_2-*n*-Si nanostructure is exposed to oxygen and hydrogen + oxygen gas mixture at room temperature, further we show the effect of temperature on the value of the signals measured in the experiments with the hydrogen + oxygen gas mixture, and finally we discuss the possible nature of these signals. In particular, we estimate the contribution of the thermoelectric effects to the size of the measured current signals.

5.3.1 Kinetics of the current induced by joint adsorption of hydrogen and oxygen molecules at room temperature

Hydrogen and oxygen are known to react on platinum surface already at low temperatures [62]. Therefore, at first we studied effects associated with the joined adsorption of these two gases on the surface of the Pt/SiO_2-*n*-Si nanostructure at room temperature, when there is no risk to damage the nanostructure.

Figure 5.17 depicts typical current signals measured from the Pt/SiO_2-*n*-Si nanostructure exposed to the hydrogen + oxygen gas mixture. The current signals detected when the same nanostructure is exposed to the components of this gas mixture separately are also shown in this figure. There are two main features of the current signal detected in the hydrogen + oxygen gas mixture. First of all, this current signal does not have additive properties. In other words, the magnitude of the signal measured in hydrogen + oxygen gas mixture is not equal to the sum of the signals in hydrogen and oxygen admitted separately, i.e. $\Delta I_{H_2+2O_2} \neq \Delta I_{H_2} + \Delta I_{2O_2}$. On the contrary, the current signal measured during admission of the hydrogen + oxygen gas mixture has a smaller

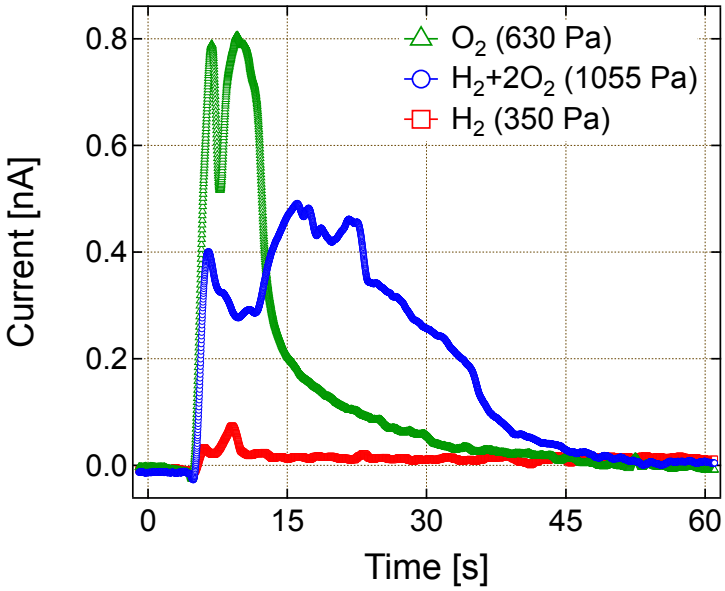

Figure 5.17: Current detected from the Pt/SiO_2-*n*-Si nanostructure exposed to molecular oxygen, hydrogen or hydrogen + oxygen gas mixture.

magnitude than the sum of the signals measured in hydrogen and oxygen (actually it is even smaller than the signal measured when the Pt/SiO_2-*n*-Si nanostructure is exposed to oxygen). Moreover, the current signal detected in the hydrogen + oxygen gas mixture can be characterized by much longer time of increase to the maximal value and decrease to the initial value, which was observed before the gas admission. The temperature of the Pt/SiO_2-*n*-Si nanostructure exposed to the hydrogen + oxygen gas mixture evolves similarity to the current signal behavior, as can be seen in Figure 5.18.

The features of the current signal detected from the nanostructure exposed to the hydrogen + oxygen gas mixture can be attributed to the ability of hydrogen to block the Pt surface and by this to prevent the oxygen adsorption, mentioned in Section 5.1. Indeed, as shown in Section 3.2 the barrier height in the nanostructures is about 0.86 eV at room temperature. This value is larger than the energy released during adsorption of hydrogen on platinum, which is around 0.7−0.78 eV per event [61, 62]. At the same time, it is smaller than the energy released during adsorbtion of oxygen, which is shown to be in the range of 2.25−2.5 eV [61, 62]. Therefore, one can expect that only dissociative adsorption of oxygen on the surface of the Pt/SiO_2-*n*-Si nanostructure can produce electronic excitations, which are energetic enough to allow electrons to overcome the potential barrier and be detected as a current signal. In this situation mixing hydrogen with oxygen during their adsorption on the Pt surface will lead to a decrease in the magnitude of the current signal. Longer times of increase and decrease of the current signal observed during admission of hydrogen + oxygen gas mixture in comparison with the values measured during admission of oxygen only can be explained by a surface reaction between hydrogen and oxygen. In this reaction,

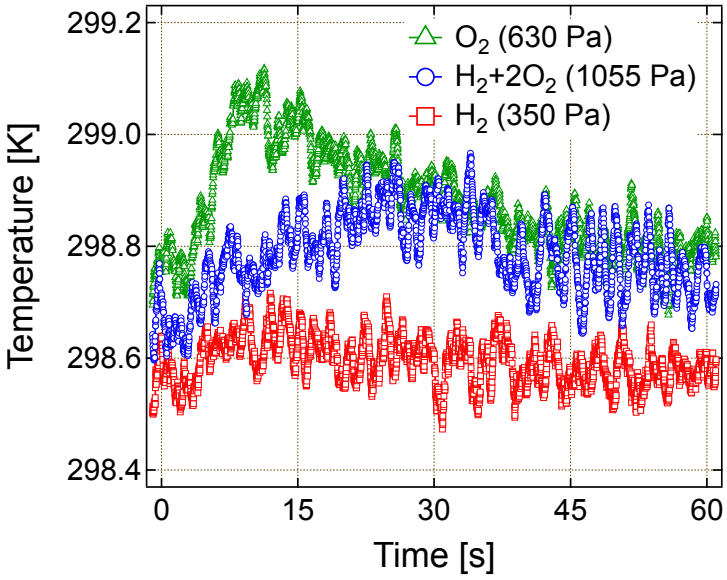

Figure 5.18: Temperature of the Pt/SiO_2-*n*-Si nanostructure exposed to molecular oxygen, hydrogen or hydrogen + oxygen gas mixture.

the Pt surface may be partially cleaned from hydrogen due to the formation of water molecules, giving new places for oxygen adsorption and thus prolongation of the current signal. However, we were not able to detect the appearance of water in the HV chamber during the joined adsorption of hydrogen and oxygen and thereby to prove this hypothesis experimentally.

A distinctive feature of the current signals, shown in Figure 5.17, is a multi-peak structure, which can be clearly seen for all three curves. We have found, that such a separation into several peaks becomes visible when the rate of the gas admission is decreasing. This can be seen in Figure 5.19, for the case of oxygen admission. For the oxygen admission with the higher rate ($dP_{O_2}/dt = 364$ Pa·s^{-1}) the current signal has the ony one clearly seen maxima. At the same time, for smaller rate of the oxygen admission ($dP_{O_2}/dt = 100$ Pa·s^{-1}) the current signal has already two peaks. Similar graphs can be seen also when the Pt/SiO_2-*n*-Si nanostructure is exposed to the hydrogen + oxygen gas mixture.

5.3.2 Kinetics of the current induced by joint adsorption of hydrogen and oxygen molecules at elevated temperatures

As mentioned in Section 5.1, the water formation reaction on platinum is significantly faster at elevated temperatures, which allows us to observe the product of this reaction simultaneously with the current signal detected from the Pt/SiO_2-*n*-Si nanostructure. This in turn makes it possible to compare the evolution of the current signal and temperature of

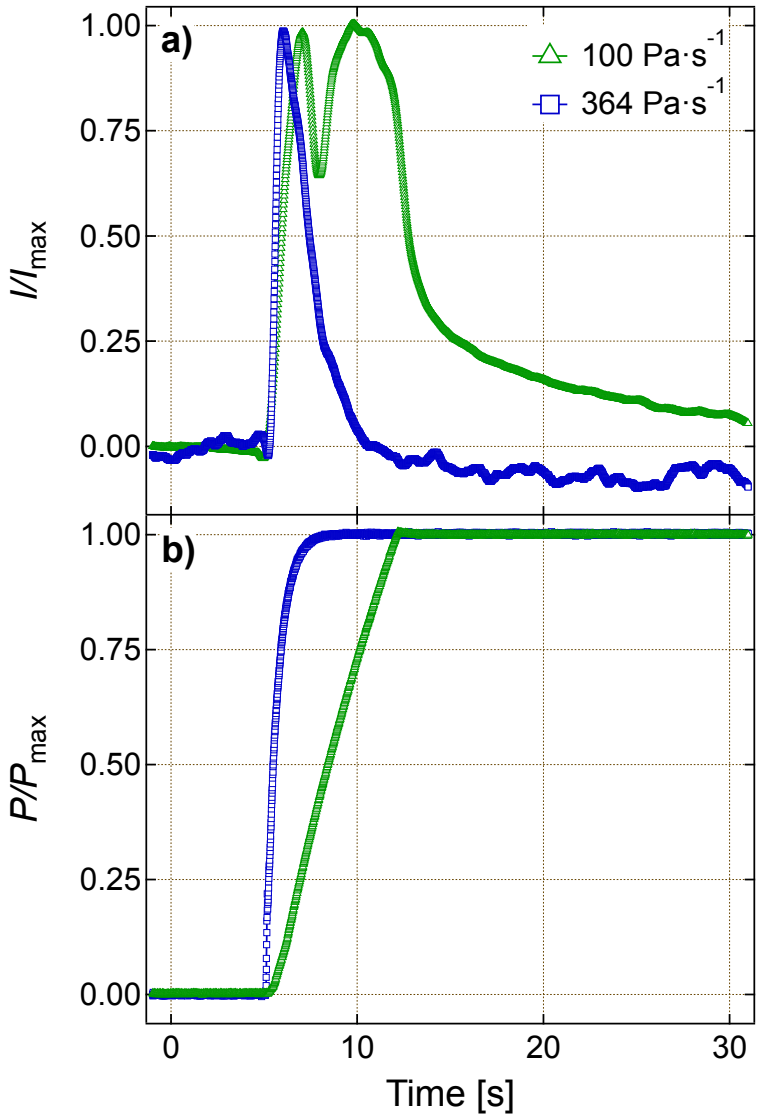

Figure 5.19: a) Normalized current detected from the Pt/SiO_2-*n*-Si nanostructure exposed to molecular oxygen for different rates of the gas admission. b) Normalized gas pressure in the high vacuum chamber.

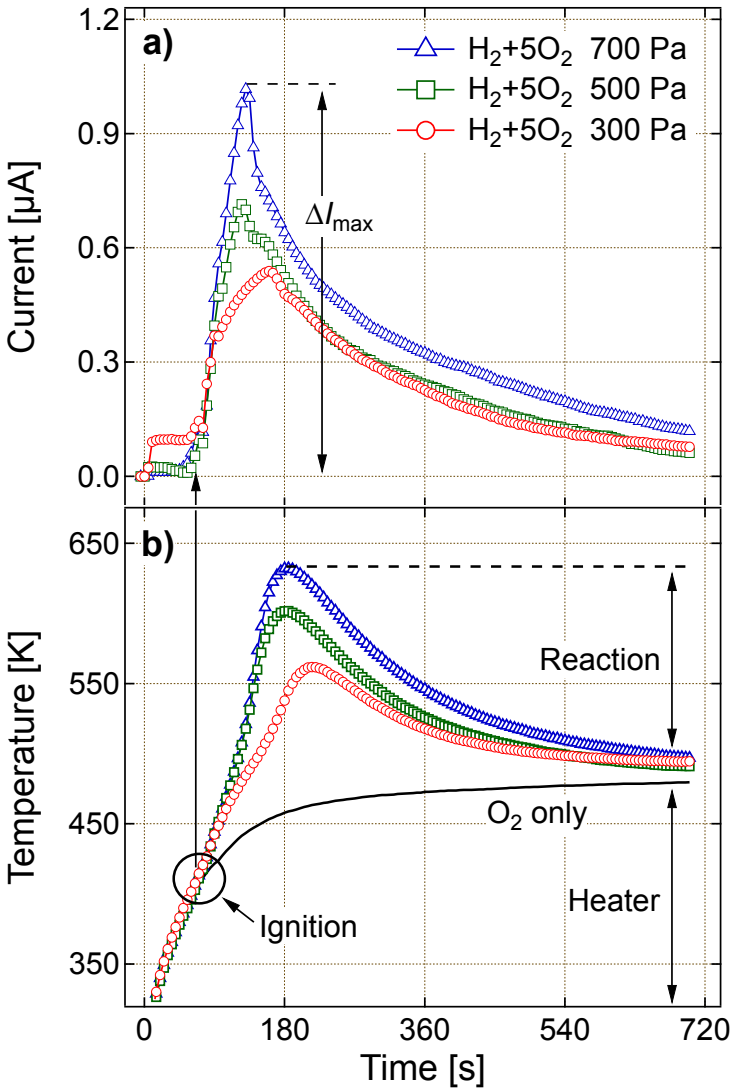

Figure 5.20: a) Current signal and b) temperature measured from the Pt/SiO_2-*n*-Si nanostructure when the water formation reaction takes place on its surface.

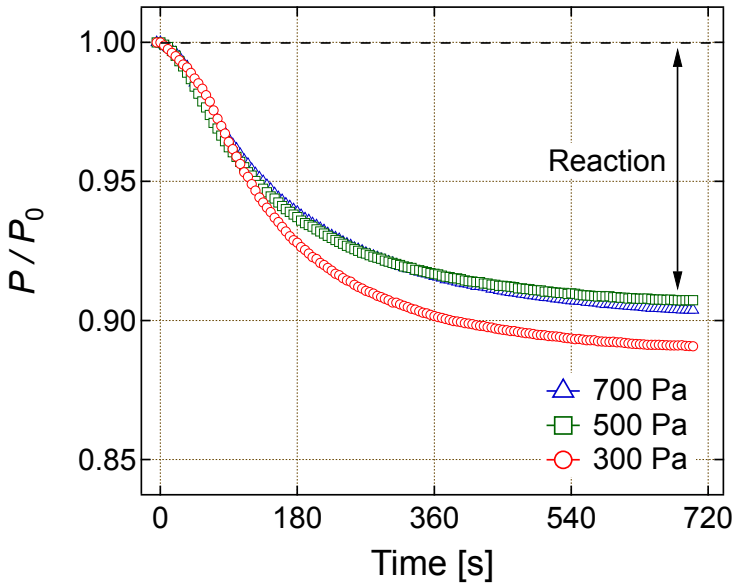

Figure 5.21: Change in pressure in the high vacuum chamber when the water formation reaction takes place on a surface of the Pt/SiO_2-*n*-Si nanostructure.

the Pt/SiO_2-*n*-Si nanostructure with the kinetics of the surface chemical reaction, which in principle can provide a hint about the origin of the current signal.

The experiments described in this section were performed as follows: at first the HV chamber with the Pt/SiO_2-*n*-Si nanostructure at room temperature was filled with the hydrogen + oxygen gas mixture, further the nanostructure was heated to a temperature at which hydrogen and oxygen start to react. Under conditions of a constant volume (during the experiment gas mixture neither admitted into the HV chamber nor pumped out of it) the current signal from the Pt/SiO_2-*n*-Si nanostructure, changes in temperature of the nanostructure and pressure in the HV chamber were measured.

In Figure 5.20a typical current signals measured from the Pt/SiO_2-*n*-Si nanostructure during the surface reaction between hydrogen and oxygen are shown for different initial pressures of the gas mixture in the HV chamber. Corresponding changes in temperature of the nanostructure during the surface reaction are shown in Figure 5.20b. In order to demonstrate the heating effect produced by the chemical reaction, temperatures of the nanostructure when heated in an oxygen atmosphere under the same pressures (the curves, showing temperature of the nanostructure heated in 300, 500, and 700 Pa of oxygen, are almost identical, thus, only one of them is shown the figure) are also shown in this figure. Finally, relative changes in pressure in the HV chamber during the water formation reaction on the surface of the Pt/SiO_2-*n*-Si nanostructure are shown in Figure 5.21. Here, P_0 denotes the initial pressure (measured before the surface reaction was initiated by heating of the Pt/SiO_2-*n*-Si nanostructure) of the hydrogen + oxygen mixture 300, 500, and 700 Pa.

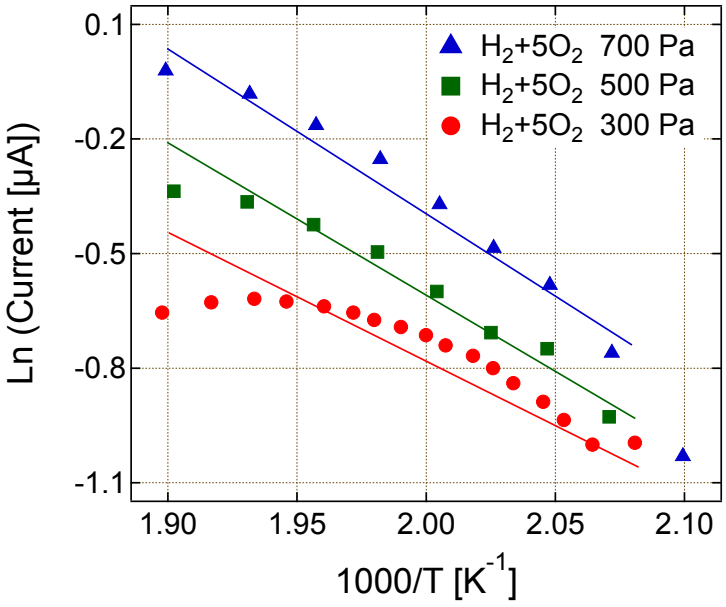

Figure 5.22: Arrhenius plot obtained from the current measured from the Pt/SiO_2-n-Si nanostructure when the water formation reaction takes place on its surface.

As can be seen in Figure 5.20, the current signal increases rapidly when the temperature of the Pt/SiO_2-n-Si nanostructure reaches the value, at which the ignition of hydrogen occurs (T_{ignition}). At the maximal point, this current signal gains a magnitude of up to one micro ampere, which is a factor of 2×10^3 bigger than the current signal measured from the same nanostructure at room temperature (see Figure 5.17). Simultaneously, a significant heating of the nanostructure is observed. Depending on the pressure, this heating can lead to temperatures $100 - 170$ K higher than those measured in the experiments with pure oxygen.

The logarithm of the current signals, recorded from the Pt/SiO_2-n-Si nanostructure during the water formation reaction, in the temperature interval from T_{ignition} to the maximal reached value is plotted in Figure 5.22 against the inverse temperature of the nanostructure. It contains regions where the dependence close to linear is observed. This allows us to estimate the activation energy, for which we obtained $E_{\text{ac}} = 0.33 \pm 0.05$ eV. This is close to values estimated elsewhere for the water formation reaction on the surface of MS Schottky diodes [7, 14]. It should also be noted that this value of the activation energy is close to the activation energy for the water desorption from the surface of platinum, which is around 0.43 eV [61, 62].

5.3.3 Thermoelectric effects in Pt/SiO_2-*n*-Si nanostructures during hydrogen + oxygen reaction

In order to measure the contribution of the thermoelectric effect in the generation of the current signals during the water formation reaction, shown in Figure 5.20, let us first estimate the maximal heating power, which is produced by the reaction.

Similar to the arguments given in Section 5.2.2, the change in temperature (ΔT) of the Pt/SiO_2-*n*-Si nanostructure with time during the water formation reaction on its surface can be written as

$$C\frac{d\Delta T}{dt} = Q_+ - Q_-, \tag{5.10}$$

where C is the heat capacity of the nanostructure, Q_+ and Q_- are the powers of heat generation and loss, respectively. To simplify finding of the analytical solution for this equation, let us assume that: (1) the power of the chemical heat generation is proportional to the time, i.e. $Q_+ = q_\mathrm{r}\, t$, where q_r is a constant; (2) in the time interval from the start of heating of the Pt/SiO_2-*n*-Si nanostructure due to ignition of hydrogen and until the moment when the temperature reaches the maximum value, the power of heat generation Q_+ is significantly bigger than the power of heat loss Q_-, so the latter one can be neglected. Thus the Equation 5.10 can be rewritten as

$$C\frac{d\Delta T}{dt} = q_\mathrm{r}\, t. \tag{5.11}$$

Taking into account the initial conditions $\Delta T(t = 0) = 0$ K, this equation can be solved analytically, yielding

$$\Delta T = \frac{1}{2}\frac{q_\mathrm{r}\, t^2}{C}. \tag{5.12}$$

Figure 5.23 shows experimental and calculated changes in temperature of the Pt/SiO_2-*n*-Si nanostructure due to the heat released on the surface of the nanostructure by the water formation reaction. The experimental curves, shown in this figure, are obtained by subtracting the temperature values measured when the nanostructure is heated in oxygen from the corresponding temperatures measured in the hydrogen + oxygen gas mixture (the original curves showing temperature of the nanostructure measured in oxygen and hydrogen + oxygen gas mixture were shown previously in Figure 5.20b). The calculated curves are obtained using Equation 5.12, where the parameter q_r was equal to 6.7×10^{-4}, 1.75×10^{-3}, and 2.0×10^{-3} W·s^{-1} for 300, 500, and 700 Pa respectively.

A good agreement between experimental and calculated curves for the time interval between the start of the hydrogen ignition and until the moment when the temperature of the Pt/SiO_2-*n*-Si nanostructure reaches the maximum value, shown in Figure 5.23, allows us to estimate the maximal heating power produced by the water formation reaction on the Pt surface. This value, denoted as $Q_+^{\max}$, can be found as a product of the parameter

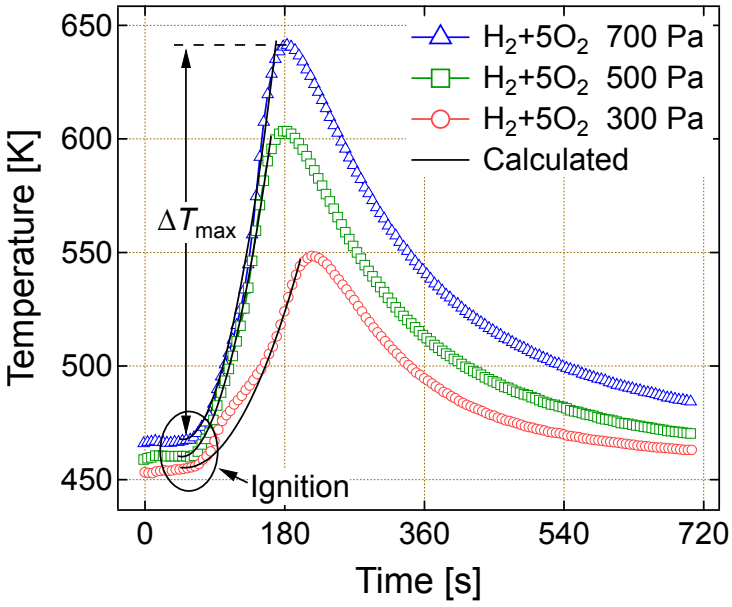

Figure 5.23: Experimental and calculated changes in temperature of the Pt/SiO_2-*n*-Si nanostructure due to the heat released on the surface during the water formation reaction.

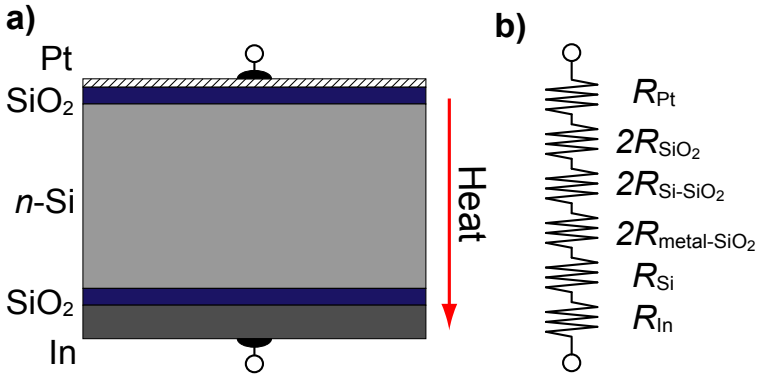

Figure 5.24: a) Cross-sectional view and b) equivalent thermal circuit of the Pt/SiO_2-*n*-Si nanostructure.

Table 5.1: Fitting parameters for the calculation of the thermoelectric current in the Pt/SiO_2-n-Si nanostructure.

Parameter	300 Pa	500 Pa	700 Pa
q_r	6.7×10^{-4} W·s^{-1}	1.75×10^{-3} W·s^{-1}	2.0×10^{-3} W·s^{-1}
Δt_{max}	150 s	115 s	120 s
Q_+^{max}	1.01×10^{-1} W	2.01×10^{-1} W	2.4×10^{-1} W

q_r and the time interval, which is necessary to increase the temperature of the Pt/SiO_2-n-Si nanostructure from the value at the moment of ignition to the maximal value, i.e. $Q_+^{max} = q_r \, \Delta t_{max}$. The values obtained in this way, are listed in Table 5.1.

As reported in Section 1.2.2, the voltage, which is generated in the Pt/SiO_2-n-Si nanostructure due to the thermoelectric effect, can be found as $V_{TE} = S_{NS}\Delta T_{NS} - IR_{ser}$, where S_{NS} is the thermopower (Seebeck coefficient) of the nanostructure (NS), ΔT_{NS} is the temperature difference across the nanostructure, I is the electric current through the nanostructure, and R_{ser} is the series resistance. To find the temperature difference across the Pt/SiO_2-n-Si nanostructure, we consider an equivalent thermal circuit, which is depicted in Figure 5.25. Then, the temperature difference can be written as

$$\Delta T_{NS} = R_{NS} \, Q_+^{max}, \tag{5.13}$$

where R_{NS} is the thermal resistance of the nanostructure. For our case the thermal resistance is given by

$$R_{NS} = R_{Pt} + R_{In} + R_{Si} + 2(R_{SiO_2} + R_{Si/SiO_2} + R_{metal/SiO_2}), \tag{5.14}$$

where R_{Pt}, R_{In}, R_{Si}, R_{SiO_2}, are thermal resistances of the Pt, In, Si, and SiO_2 layers, R_{Si/SiO_2}, R_{Si/SiO_2} are thermal resistances of the Si/SiO_2 and metal/SiO_2 (metal = Pt or In) interfaces.

Taking into account the small thickness and relatively good thermal conductivity of the metal layers and interfaces of the Pt/SiO_2-n-Si nanostructure, R_{NS} can be taken as equal to the thermal resistance of the Si wafer [17], which in turn can be found as

$$R_{Si} = d/k_{Si}A, \tag{5.15}$$

where d is the thickness of the silicon layer, $k_{Si} = 0.03 + 1.56 \times 10^{-3} \, T + 1.65 \times 10^{-6} \, T^2$ is the thermal conductivity of silicon [56], T is the temperature, and A is the cross-sectional area of the Pt/SiO_2-n-Si nanostructure perpendicular to the path of heat flow. As well, we can take the thermopower of the nanostructure equal to the thermopower of the silicon layer [17], which is well known for a wide range of temperatures (see, for example, References [57, 58]).

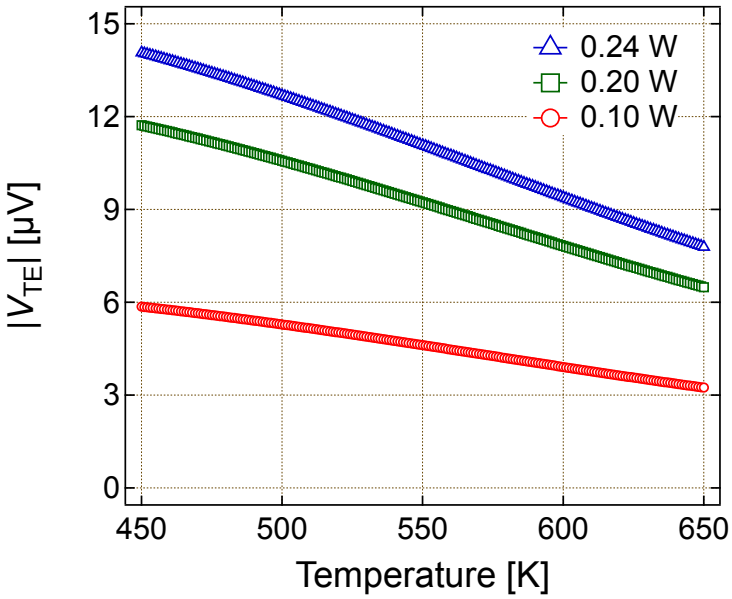

Figure 5.25: Calculated absolute value of the voltage, generated in the Pt/SiO_2-*n*-Si nanostructure due to the thermoelectric effect, as a function of temperature.

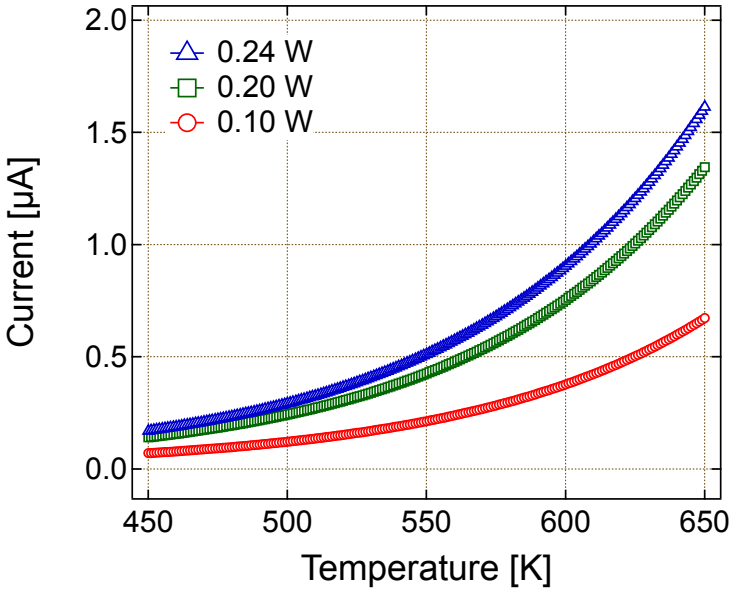

Figure 5.26: Calculated thermoelectric current in the Pt/SiO_2-*n*-Si nanostructure as a function of temperature for several values of heating power.

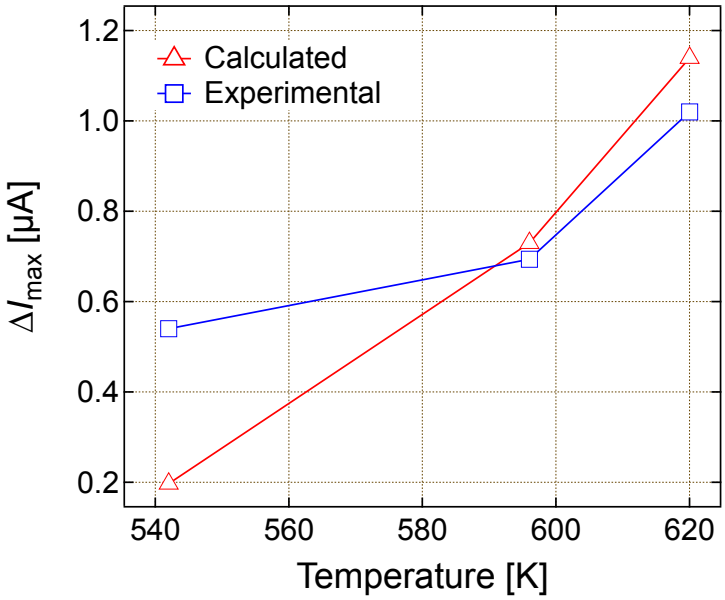

Figure 5.27: A comparison of the maximal value of the current signal, measured from the Pt/SiO_2-n-Si nanostructure during the water formation reaction, and the calculated value of the thermoelectric current at different temperatures.

Taking into account the above mentioned assumptions, the thermoelectric voltage in the Pt/SiO_2-n-Si nanostructure can be written as

$$V_{\mathrm{TE}} = \frac{S_{\mathrm{Si}} Q_{+}^{\max} d}{k_{\mathrm{Si}} A} - I R_{\mathrm{ser}} \,. \tag{5.16}$$

Equation 5.16 does not allow the calculation of V_{TE} since the current through the nanostructure (I) is not known. In turn, this current can be calculated by substitution of the thermoelectric voltage in the equation which describes the current-voltage characteristics of the nanostructure (see Section 3.2). In order to resolve this conflict, we will simplify Equation 5.16 by taking $R_{\mathrm{ser}} = 0$. It is important to note, that this simplification leads to an overestimate of the thermoelectric current. Thus, in the further discussion it makes sense to consider only the order of magnitude of the thermoelectric current, but not the absolute value of it.

Figure 5.25 shows the absolute value of the voltage, generated in the Pt/SiO_2-n-Si nanostructure due to the thermoelectric effect, as a function of temperature, which was calculated using Equation 5.16 for the previously estimated values of the maximal heating power ($Q_{+}^{\max}$). One can see, that the thermoelectric voltage, generated in the nanostructure, is rather small being on the order of tens of microvolts, which agrees well with the general estimates, discussed in Section 1.2.2. The decrease of V_{TE} at higher temperatures is due to a temperature dependence of the Seebeck coefficient for silicon, which tends to have smaller values at high temperatures [57, 58].

The thermoelectric current, generated due to the Seebeck effect in the silicon layer of the Pt/SiO_2-n-Si nanostructure, can be obtained by substituting V_{TE}, calculated using Equation 5.16, in the current-voltage relationship for the composite nanostructure [16, 17]. For the Pt/SiO_2-n-Si nanostructure, this relationship is described in a great detail in Section 3.2. Figure 5.26 shows the calculated thermoelectric current in the Pt/SiO_2-n-Si nanostructure as a function of temperature for the values of heating power, which were estimated by fitting of the experimental curves, showing changes in the temperature of the Pt/SiO_2-n-Si nanostructure in the course of the water formation reaction. As can be seen, even such a small thermoelectric voltage as the one estimated using Equation 5.16, leads to a notable thermoelectric current. The value of this current lies in the microampere range and has a tendency to rise with temperature. A comparison of the current signal, measured from the Pt/SiO_2-n-Si nanostructure during the water formation reaction, and the calculated thermoelectric current is shown in Figure 5.27. In this figure, values of ΔI_{max}, which are defined as a difference between the maximal current through the Pt/SiO_2-n-Si nanostructure during the water formation reaction and a current, when the temperature of the nanostructure is equal to $T_{ignition}$ (this is the moment, when the water formation reaction starts), are plotted versus temperature for both measured and calculated currents. At lower temperatures, the calculated current is factor of two smaller than the experimentally measured current, induced by the water formation reaction. Contrariwise, at higher temperatures, the calculated current is somewhat bigger than the measured current. However, in the whole temperature range both measured and calculated currents have rather similar values. Therefore, we tend to think that the current signals, detected from the nanostructure in the course of the water formation reaction, shown in Figure 5.20 and Figure 5.27, are the result of the thermoelectric effect. In this case, we think, that the small differences in the magnitude of the measured and calculated currents, shown in Figure 5.27, are the result of the simplifications, made during the calculation of the thermoelectric effects. Thus, we see no need to consider other mechanisms of the current generation, such as electric charge carrier creation due to non-adiabatic effects of chemical energy dissipation, to explain the results presented in this chapter. However, this does not indicate a lack of processes of creation such excited charge carriers due to the non-adiabatic dissipation of the energy, released in the water formation reaction on platinum at high temperatures. More likely, this fact should be interpreted as an inability of the Pt/SiO_2-n-Si nanostructures to detect such processes due to a presence of the powerful signal, caused by thermoelectric effects at high temperatures.

Chapter 6

Conclusion and Outlook

In this work the Pt/SiO_2-n-Si metal-oxide-semiconductor nanostructures were used for the study of processes of an electric charge generation and transfer, induced by the steps of the water formation reaction on a polycrystalline surface of platinum. Based on the achieved experimental results and model calculations, following conclusions can be drawn:

- Adsorption of the hydrogen + oxygen gas mixture as well as of the components of this mixture (pure hydrogen and oxygen) on the surface of a Pt/SiO_2-n-Si nanostructure leads to measurable signals, which can be detected as an electric current between the top platinum and back indium contacts of the nanostructure. At room temperature, these current signals have a shape of sharp peaks with the maximal amplitude in the range of several nanoamperes and an exponential decay with time. The maximal amplitude of the current signals is sensitive to the history of the surface: it decreases in the consecutive experiments, but can be recovered by outgassing of the Pt/SiO_2-n-Si nanostructure in high vacuum. At elevated temperatures ($T > 320$ K), the adsorption of the hydrogen + oxygen gas mixture is accompanied by a highly energetic reaction of water formation, which causes significant heating of the Pt/SiO_2-n-Si nanostructure. The current signal, measured during this reaction, reaches several microamperes and reflects the process of the hydrogen burning in the reactor.

- Analysis of the current signals, measured from the Pt/SiO_2-n-Si nanostructure during the adsorption of hydrogen and oxygen, and the surface reaction between these gases, indicates the presence of several processes, which may be responsible for the creation of these current signals. So, for example, a comparison of the current signals, detected during the reaction of water formation at elevated temperatures, with the calculated thermoelectric currents indicates that these current signals can be largely attributed to the Seebeck effect in the silicon layer of the Pt/SiO_2-n-Si nanostructure. Hence, the current signals, detected during the reaction of water formation at elevated temperatures, reflect the transport of heat through the Pt/SiO_2-

n-Si nanostructure, rather than excitation of electrons and holes on the surface of the platinum top electrode due to the non-adiabatic dissipation of chemical energy. The current signals detected during the adsorption of hydrogen on the surface of the Pt/SiO_2-n-Si nanostructure at room temperature may also be attributed to the thermoelectric effect in the silicon layer. At the same time, the current signals, measured from the Pt/SiO_2-n-Si nanostructure during the adsorption of oxygen and the hydrogen + oxygen gas mixture at room temperature, are almost an order of magnitude larger, than the expected thermoelectric current. The last fact is verified by both the model calculations of the thermoelectric current and the experiments, where the thermoelectric current, generated with the use of a small heater attached to the surface of the Pt/SiO_2-n-Si nanostructure, was measured. Therefore, we can talk about the presence of an additional, non-thermoelectric process leading to the current signals during the during the adsorption of oxygen or the hydrogen + oxygen gas mixture at room temperature. The nature of this process is still unclear presently.

The fact that the analysis of the experimental results, done in this work, points to the thermoelectric nature of the current signals, detected with the use of Pt/SiO_2-n-Si nanostructures in the course of the water formation reaction at elevated temperatures, does not automatically mean the absence of the excited charge carriers due to the non-adiabatic dissipation of the energy, released in the reaction. According to our estimations, based on some basic considerations of the heat transport and related to it the electric charge transport, the metal-semiconductor and metal oxide-semiconductor nanostructures suffer from the significant thermoelectric effect at elevated temperatures. These effects are especially notable for the nanostructures which are based on the thick (hundreds of micrometers) substrates of high-mobility semiconductors, as, for example, MOS nanostructures used in this work. Therefore, such nanostructures do not allow for the observation of the electric charge creation due to the non-adiabatic effects of the energy dissipation against the more powerful background thermoelectric current at the temperatures at which catalytic reactions take place. Taking this into account, the use of nanostructures with other architectures, which would allow to reduce thermoelectric effects, seems to us as the next step in the study of the non-adiabatic effects in the dissipation of chemical energy.

Bibliography

[1] Hasselbrink, E. and Lundqvist, B. I., editors. *Dynamics*, volume 3 of *Handbook of Surface Science*. North-Holland, (2008).

[2] Nienhaus, H. *Surface Science Reports* **45**(1-2), 1–78 (2002).

[3] Hasselbrink, E. *Surface Science* **603**(11-12), 1564–1570 (2009).

[4] Hasselbrink, E. *Current Opinion in Solid State and Materials Science* **10**(3-4), 192–204 (2006).

[5] Nienhaus, H., Bergh, H., Gergen, B., Majumdar, A., Weinberg, W., and McFarland, E. *Physical Review Letters* **82**(2), 446–449 (1999).

[6] Park, J., Lee, H., Renzas, J., Zhang, Y., and Somorjai, G. *Nano Letters* **8**(8), 2388–2392 (2008).

[7] Hervier, A., Renzas, J. R., Park, J. Y., and Somorjai, G. *Nano Letters* **9**(11), 3930–3933 (2009).

[8] Karpov, E. G. and Nedrygailov, I. I. *Applied Physics Letters* **94**, 214101 (2009).

[9] Dasari, S. K., Hashemian, M. A., Mohan, J., and Karpov, E. G. *Chemical Physics Letters* **553**, 47–50 (2012).

[10] Liu, X., Cuenya, B., and McFarland, E. *Sensors and Actuators B* **99**(2-3), 556–561 (2004).

[11] Mildner, B., Hasselbrink, E., and Diesing, D. *Chemical Physics Letters* **432**(1-3), 133–138 (2006).

[12] Schindler, B., Diesing, D., and Hasselbrink, E. *The Journal of Physical Chemistry C* **117**, 6337–6345 (2013).

[13] Karpov, E. G. and Nedrygailov, I. I. *Physical Review B* **81**(20), 205443 (2010).

[14] Nedrygailov, I. I. and Karpov, E. G. *Sensors and Actuators B* **148**(2), 388–391 (2010).

[15] Schierbaum, K. and Achhab, M. E. *Phys. Status Solidi A* **208**(12), 2796–2802 (2011).

[16] Creighton, J. and Coltrin, M. *Journal of Physical Chemistry C* **116**, 1139–1144 (2012).

[17] Nedrygailov, I. I., Karpov, E. G., Hasselbrink, E., and Diesing, D. *Journal of Vacuum Science and Technology A* **31**(2), 021101 (2013).

[18] Shustorovich, E. *Metal-Surface Reaction Energetics*. VCH, Wienheim, (1991).

[19] Baule, B. *Annalen der Physik* **349**(9), 145–176 (1914).

[20] Hall, J., Saksager, O., and Chorkendorff, I. *Chemical Physics Letters* **216**(3,4,5,6), 413–417 (1993).

[21] Gumhalter, B. and Matsushima, T. *Surface Science* **561**, 183–192 (2004).

[22] Langmuir, I. *Transactions of the Faraday Society* **17**(621-654) (1922).

[23] Eley, D. D. and Rideal, E. K. *Nature* **146**(3699), 401–402 (1940).

[24] Harris, J. and Kasemo, B. *Surface Science* **105**, L281–L287 (1981).

[25] Nørskov, J. K. and Lundqvist, B. I. *Surface Science* **89**, 251–261 (1979).

[26] Greber, T. *Surface Science Reports* **28**, 1–64 (1997).

[27] Born, M. and Oppenheimer, R. *Annalen der Physik* **84**, 457–484 (1927).

[28] Shalimova, K. V. *Physics of Semiconductors*. Energoatomizdat, 3 edition, (1985).

[29] Böttcher, A., Grobecker, R., Imbeck, R., Morgante, A., and Ertl, G. *Journal of Chemical Physics* **95**(5), 3756–3766 (1991).

[30] Robertson, A. J. B. *International Journal of Electronics* **51**(5), 607–619 (1981).

[31] Brotzen, F. R. *Physica Status Solidi* **22**(1), 9–30 (1967).

[32] Heidberg, J., Hussla, I., and Stammberger, K. H. *Thin Solid Films* **90**, 209–214 (1982).

[33] Kasemo, B. *Physical Review Letters* **32**(20), 1114–1117 (1974).

[34] Amirav, A., Lambert, W. R., Cardillo, M. J., Trevor, P. L., Luke, P. N., and Haller, E. E. *Journal of Applied Physics* **59**(6), 2213–2215 (1986).

[35] Amirav, A., Cardillo, M. J., Trevor, P. L., Lim, C., and Tully, J. C. *Journal of Chemical Physics* **87**(3), 1796–1807 (1987).

[36] Gergen, B., Nienhaus, H., Weinberg, W., and McFarland, E. *Science* **294**, 2521–2523 (2001).

[37] Krix, D., Nuenthel, R., and Nienhaus, H. *Physical Review B* **75**(7), 073410 (2007).

[38] Schindler, B., Diesing, D., and Hasselbrink, E. *The Journal of Chemical Physics* **134**, 034705 (2011).

[39] Ji, X. Z., Zuppero, A., Gidwani, J., and Somorjai, G. *Nano Letters* **5**(4), 753–756 (2005).

[40] Park, J., Renzas, J., Hsu, B., and Somorjai, G. *Journal of Physical Chemistry C* **111**(42), 15331–15336 (2007).

[41] Karpov, E. G., Hashemian, M. A., and Dasari, S. K. *Journal of Physical Chemistry C* **117**, 15632–15638 (2013).

[42] Stella, K., Kovacs, D. A., Diesing, D., Brezna, W., and Smoliner, J. *Journal of the Electrochemical Society* **158**(5), P65–P74 (2011).

[43] Frese, K. and Chen, C. *Journal of the Electrochemical Society* **139**(11), 3234–3243 (1992).

[44] Quinn, J. J. *Physical Review* **126**(4), 1453–1457 (1962).

[45] Rhoderick, E. H. and Williams, R. H. *Metal-Semiconductor Contacts*. Clarendon Press, Oxford, second edition, (1988).

[46] Sze, S. M. *The Physics of Semiconductor Devices*. Wiley, New York, second edition, (1981).

[47] Nienhaus, H., Bergh, H., Gergen, B., Majumdar, A., Weinberg, W., and McFarland, E. *Applied Physics Letters* **74**(26), 4046–4048 (1999).

[48] Diesing, D., Kovacs, D., Stella, K., and Heuser, C. *Nuclear Instruments and Methods in Physics Research B* **269**(11), 1185–1189 (2011).

[49] Gergen, B., Weyers, S., Nienhaus, H., Weinberg, W., and McFarland, E. *Surface Science* **488**, 123–132 (2001).

[50] Cuenya, B. R., Nienhaus, H., and McFarland, E. *Physical Review B* **70**(11), 115322 (2004).

[51] Krix, D., Huba, K., and Nienhaus, H. *Journal of Vacuum Science and Technology A* **27**(4), 918–922 (2009).

[52] Hagemann, U., Krix, D., and Nienhaus, H. *Physical Review Letters* **104**(2), 028301 (2010).

[53] Hagemann, U., Timmer, M., Krix, D., Kratzer, P., and Nienhaus, H. *Physical Review B* **82**(15), 155420 (2010).

[54] Park, J., Renzas, J., Contreras, A., and Somorjai, G. *Topics in Catalysis* **46**(1-2), 217–222 (2007).

[55] Chien, H.-C., Yao, D.-J., and Hsu, C.-T. *Appl. Phys. Lett.* **93**, 231910 (2008).

[56] Madelung, O., editor. *Semiconductors: Data Handbook*. Springer, Berlin, third edition, (2004).

[57] Fulkerson, W., Moore, J. P., Williams, R. K., Graves, R. S., and McElroy, D. L. *Phys. Rev.* **167**(3), 765–782 (1968).

[58] Geballe, T. H. and Hull, G. W. *Phys. Rev.* **98**(4), 940–947 (1955).

[59] Nedrygailov, I. I., Hasselbrink, E., Diesing, D., Dasari, S. K., Hashemian, M. A., and Karpov, E. G. *J. Vac. Sci. Technol. A* **30**(3), 030601 (2012).

[60] Ljungström, S., Kasemo, B., Rosen, A., Wahnström, T., and Fridell, E. *Surface Science* **216**, 63–92 (1989).

[61] Williams, W., Marks, C., and Schmidt, L. *The Journal of Physical Chemistry* **96**(14), 5922–5931 (1992).

[62] Hellsing, B., Kasemo, B., and Zhdanov, V. *Journal of Catalysis* **132**(1), 210–228 (1991).

[63] Ikeda, H., Libby, P. A., and Williams, F. A. *Combustion and Flame* **93**, 138–148 (1993).

[64] Fassini, M., Zhdanov, V. P., Rinnemo, M., Keck, K. E., and Kasemo, B. *Journal of Catalysis* **141**, 438–452 (1993).

[65] Bui, P. A., Vlachos, D. G., and Westmoreland, P. R. *Industrial & Engineering Chemistry Research* **36**, 2558–2567 (1997).

[66] Rinnemo, M., Deutschmann, O., Behrendt, F., and Kasemo, B. *Combustion and Flame* **111**(4), 312–326 (1997).

[67] Keck, K. E. and Kasemo, B. *Surface Science* **126**, 469–478 (1983).

[68] Mitchell, G. E., Akhter, S., and White, J. M. *Surface Science* **166**, 283–300 (1986).

[69] Wagner, F. T. and Moylan, T. E. *Surface Science* **206**(1-2), 187–202 (1988).

[70] Gland, J. L., Sexton, B. A., and Fisher, G. B. *Surface Science* **95**, 587–602 (1980).

[71] Campbell, C. T., Ertl, G., Kuipers, H., and Segner, J. *Surface Science* **107**, 220–236 (1981).

[72] Bonzel, H. P. and Ku, R. *Surface Science* **40**, 85–101 (1973).

[73] Gland, J. L. *Surface Science* **93**, 487–514 (1980).

[74] Steininger, H., Lehwald, S., and Ibach, H. *Surface Science* **123**, 1–17 (1982).

[75] Derry, G. N. and Ross, P. N. *Journal of Chemical Physics* **82**, 2772–2778 (1985).

[76] Weaver, J. F., Chen, J., and Gerrard, A. L. *Surface Science* **592**, 83–103 (2005).

[77] Moll, J. L. *IRE Wescon Convention Record* , 32 (1959).

[78] Pfann, W. G. and Garrett, C. G. *Proceedings of Radio Engineers* **47**, 2011 (1959).

[79] Fowler, R. H. and Nordheim, L. *Proceedings of the Royal Society A* **119**, 173–181 (1928).

[80] Tersoff, J. *Physical Review Letters* **52**(6), 465–468 (1984).

[81] Tersoff, J. *Physical Review B* **32**(10), 6968–6971 (1985).

[82] Werner, J. H. and Güttler, H. *Journal of Applied Physics* **73**, 1315–1319 (1993).

[83] McBrayer, J. D., Swanson, R. M., and Sigmon, T. W. *Journal of the Electrochemical Society* **133**(6), 1242–1246 (1986).

[84] Tsui, B.-Y. and Chen, M.-C. *Solid-State Electronics* **36**(4), 583–593 (1993).

[85] Jones, C. E. and Johnson, G. E. *Journal of Applied Physics* **52**(8), 5159–5163 (1981).

[86] Prabhakar, A., McGill, T. C., and Nicolet, M.-A. *Applied Physics Letters* **43**(12), 1118–1120 (1983).

[87] Majni, G., Costato, M., and Panini, F. *Journal of Physics and Chemistry of Solids* **46**(5), 631–641 (1985).

[88] Thomsen, L. B. *MIS hot electron devices for enhancement of surface reactivity by hot electrons*. PhD thesis, Technical University of Denmark, (2009).

[89] Wodtke, A., Tully, J., and Auerbach, D. *International Reviews in Physical Chemistry* **23**(4), 513–539 (2004).

[90] Redhead, P. A. *Vacuum* **12**(4), 203–211 (1962).

[91] Menzel, D. *Desorption phemomena*, volume 4, 101–142. Springer Berlin Heidelberg (1975).

[92] de Jong, A. M. and Niemantsverdriet, J. W. *Surface Science* **233**(3), 355–365 (1990).

[93] Fisher, G. B. and Gland, J. L. *Surface Science* **94**(2-3), 446–455 (1980).

[94] Ibach, H. and Lehwald, S. *Surface Science* **91**(1), 187–197 (1980).

[95] Grecea, M. L., Backus, E. H. G., Riedmüller, B., Eichler, A., Kleyn, A. W., and Bonn, M. *Journal of Physical Chemistry B* **108**, 12575–12582 (2004).

[96] Rathore, M. M. and Kapuno, R. A. *Engineering heat transport*. Jones & Bartlett Learning, 2 edition, (2010).

[97] Sears, F. W., Zemansky, M. W., and Young, H. D. *University Physics*. Addison-Wesley Publishing Company, 7 edition, (1987).

[98] Rinnemo, M., Fassini, M., and Kasemo, B. *Chemical Physics Letters* **211**(1), 60–64 (1993).

[99] Frank-Kamenetskii, D. A. *Diffusion and heat transfer in chemical kinetics*. Plenum Press, New York, 2 edition, (1969).

[100] Rader, C. G. and Weller, S. W. *AIChE Journal* **20**(3), 515–522 (1974).

[101] Borroni-Bird, C. E., Al-Sarraf, N., Andersson, S., and King, D. A. *Chemical Physics Letters* **183**(6), 516–520 (1991).

Curriculum vitae

The biography is not included in the online version for reasons of data protection.

List of Publications

1. M. A. Hashemian, E. Palacios, I. I. Nedrygailov, D. Diesing, E. G. Karpov, Thermal properties of the stationary reaction current in a mesoporous Pt/TiO_2 system, *ACS Applied Materials & Interfaces* **5** (23), 12375 (2013).

2. I. I. Nedrygailov, E. G. Karpov, E. Hasselbrink, D. Diesing, On the significance of thermoelectric and thermionic emission currents induced by chemical reactions catalyzed on nanofilm metal-semiconductor heterostructures, *Journal of Vacuum Science & Technology A* **31**, 021101 (2013).

3. I. I. Nedrygailov, E. Hasselbrink, D. Diesing, S. K. Dasari, M. A. Hashemian, E. G. Karpov, Non-invasive measurement and control of the temperature of Pt nanofilms on Si supports, *Journal of Vacuum Science & Technology A* **30**, 030601 (2012).

4. I. I. Nedrygailov and E. G. Karpov, Pd/*n*-SiC nanofilm sensor for molecular hydrogen detection in oxygen atmosphere, *Sensors and Actuators B* **148**, 388 (2010).

5. E. G. Karpov and I. I. Nedrygailov, Nonadiabatic chemical to electrical energy conversion in planar Schottky nanostructures, *Proceedings of the ASME 2010 International Mechanical Engineering Congress & Exposition*, Vancouver, British Columbia, Canada, Paper No. ES2010-40634 (2010).

6. E. G. Karpov and I. I. Nedrygailov, Nonadiabatic chemical-to-electrical energy conversion in heterojunction nanostructures, *Physical Review B* **81**, 205443 (2010).

7. E. G. Karpov and I. I. Nedrygailov, Solid-state electric generator based on chemically induces internal electron emission in metal-semiconductor heterojunction nanostructures, *Applied Physics Letters* **94**, 214101 (2009).

Presentations and Talks

1. I. I. Nedrygailov, E. Hasselbrink, D. Diesing, Energy dissipation processes during surface chemical reactions at high gas pressures, International Workshop SFB 616, Bad Honnef, Germany, $3-8$ June (2013).

2. I. I. Nedrygailov, K. Asteman, E. Hasselbrink, D. Diesing, Temperature and bias voltage induced electron tunneling through ultrathin TaO_x barriers, DPG Spring Meeting, Regensburg, Germany, $10-15$ March (2013).

3. I. I. Nedrygailov, J. Meyburg, E. Hasselbrink, D. Diesing, Chemical-to-electric energy conversion in reactions of oxygen and hydrogen molecules on Pt surface, 76^{th} Annual Meeting of the DPG, Berlin, Germany, $25-30$ March (2012).

4. I. I. Nedrygailov, J. Meyburg, E. Karpov, E. Hasselbrink, D. Diesing, Non-invasive measurement and control of the temperature of Pt nanofilms on Si supports, 76^{th} Annual Meeting of the DPG, Berlin, Germany, $25 - 30$ March (2012).

5. I. I. Nedrygailov, D. Diesing, Energy flows in surface chemical reactions: heating and excited electrons, CoE CME International NanoEnergy Seminar, University of Illinois at Chicago, Chicago, Illinois, USA, 8^{th} November (2012).

6. I. I. Nedrygailov, E. Hasselbrink, D. Diesing, Probing surface chemical reactions with metal nanofilm-semiconductor Schottky diodes, AVS International Symposium and Exhibition, Tampa, Florida, USA, 28 October−2 November (2012).

7. I. I. Nedrygailov, E. Hasselbrink, D. Diesing, E. G. Karpov, Modeling of chemical reaction-induced thermal currents in metal nanofilm-semiconductor Schottky diodes, AVS International Symposium and Exhibition, Tampa, Florida, USA, 28 October−2 November (2012).

8. I. I. Nedrygailov, K. Stella, C. Soostmeyer, E. Hasselbrink, D. Diesing, Monitoring and adjusting the temperature of ultra-thin metal catalysts in situ, 75^{th} Annual Meeting of the DPG, Dresden, Germany, $13 - 18$ March (2011).

9. I. I. Nedrygailov, K. Stella, E. Hasselbrink, D. Diesing, Direct heating and monitoring of the real temperature of Pt thin film catalysts by electric current: towards local chemistry, Internationel Workshop SFB 616, Kloster Schoental, Germany, $5-8$ September (2010).

Acknowledgement

First of all I would like to thank Prof. Dr. Eckart Hasselbrink for giving me the opportunity to carry out this PhD project. Also, I would like to thank for the assistance provided by him during the whole period of time, which I spent in his group.

I would like to express my special appreciation and thanks to Dr. Detlef Diesing, who was supporting me both in the laboratory and outside of it all the time. I am very grateful for the friendly atmosphere, which he managed to create and will always fondly remember these few years that we worked together.

I would also like to thank all my colleagues and the technical staff at the Surface Dynamics Group. In particular, I would like to thank engineers Elke Normann, Hans Vanheiden, and Jürgen Leistikow for the technical support of my work and their willingness to help me in any situation.

Last but not least, I would like to thank the financial support, which was provided by the Department of Chemistry, University of Duisburg-Essen, Sonderforschungsbereich (SFB) 616 "Energiedissipation auf Oberfläche", and Deutscher Akademischer Austauschdienst (DAAD).

Erklärung

Hiermit versichere ich, dass ich die vorliegende Arbeit mit dem Titel

"**Studies of energy dissipation pathways in the water formation reaction using metal-oxide-semiconductor nanostructures**"

selbst verfasst und keine außer den angegebenen Hilfsmitteln und Quellen benutzt habe, ich bisher in keinem Promotionsverfahren gescheitert bin und dass die Arbeit in dieser oder ähnlicher Form noch bei keiner anderen Universität eingereicht wurde.

Essen, im März 2014